A CONTINUOUSLY RECORDING INTERFEROMETER IN THE CALIBRATION OF STRAINMETERS

By

Stanley Smookler

A Thesis submitted to the Faculty and the Board of Trustees of the Colorado School of Mines in partial fulfillment of the requirements for the degree of Master of Science in Geophysical Engineering.

Signed: Stanley Smookler
Stanley Smookler

Golden, Colorado

Date: 26, Feb, 1968

Approved: Maurice W. Major
Dr. Maurice W. Major
Thesis Advisor

Prof. John C. Hollister
Head of Department

Golden, Colorado

Date: 26 FEB, 1968

ABSTRACT

Romig's millimicron displacement transducer (1967) is calibrated by a variable spacing Fabry-Perot interferometer. This calibration permits absolute earth-strain measurements to an uncertainty of 1 percent.

Optical flats plane to $\lambda/50$ are mounted on a spring parallelogram. Thermal expansion of a steel tube deforms the parallelogram, smoothly displacing one of the optical flats. The resulting intensity of the 5016 Å He line, observed through a pinhole at the central zone of the interference pattern, produces a sharp peak on a pen recorder each time the plate moves a distance $\lambda/2$. Thus the displacement of the plate can be read directly from the chart. A theoretical analysis of the peak width based on the work of Chabbal (1958) agrees with the observed uncertainty.

TABLE OF CONTENTS

LIST OF FIGURES

LIST OF TABLES

Table Page

ERRATA

Page No.	Corrections
34	In eqs. 16, 17 and 18, Δm is replaced by $\frac{\Delta m}{2}$. Therefore eq. 19 should read (19) $\Delta m = \sigma_o h(\Delta\phi)^2$ and eq. 21 should read (21) $\rho_p = f(\lambda_o \Delta m/h)^{\frac{1}{2}}$
35	On the first line, the quantity 3 mm (3×10^7 Å) should be replaced by 1½ mm ($3/2 \times 10^7$ Å).
37	On the right side of eq. 22b, replace S(u-m) by D(u-m)
44	On the sixth line of sec. c-2, sec. c-3 should be replaced by sec. b-3
49	On the fourth, fifth and sixth lines, Δm is replaced by $\frac{\Delta m}{2}$. Therefore eq. 28a should read (28a) $\Delta m \simeq \frac{2h(\Delta\phi)^2}{\lambda_o}$ and eq. 28b should read (28b) $\rho_p \simeq f(\Delta m \lambda_o/2h)^{\frac{1}{2}}$ On the ninth line, h = 3 mm is replaced by h = 1½ mm. On the thirteenth line, the quantity 1½ mm is replaced by 3/4 mm.
53	In eq. 30, Δm_1 should be calculated using an air gap of thickness 3/4 mm instead of 1½ mm. Hence the half width Δm_1 should be calculated to be less than 0.035 order.
56	On the twelfth line, the second sentence should read, "The Doppler, Airy and Pinhole effects... broadening." On the 21st line, replace the quantity ½ mm by ¼ mm. The equation on the last line should then read $\rho_p = 3.5 \text{ in.} \left(\frac{5016}{2\times\frac{1}{4}\times10^7} \times 0.01\right)^{\frac{1}{2}}$

T 1164

Page No.	Corrections
59	On the second line, replace ½ mm by ¼ mm. On the fifth line, replace the quantity 0.024 order by 0.01 order. Lines 6 to 9 should be replaced by the following phrase, "which is less than the half widths of each of the Surface Defect Functions so that the surface defects now constitute a larger source of broadening than that of the Doppler effect and the Pinhole effect." On the eleventh line, the quantity 1½ mm is replaced by 3/4 mm. On the nineteenth line, the quantity ½ mm is replaced by ¼ mm.

ERRATA

Page No.	Corrections
37	On the right side of eq. 22b, replace S(u-m) by D(u-m).
44	On the sixth line of sec. c-2 replace the words sec. c-3 by the words sec. b-3.
45 46 47	In figures 11, 12, and 13 the scale of the x-axis is incorrect. The order numbers 0.01 and 0.02 must be replaced by the numbers 0.05 and 0.10 respectively.
50	The corrections to be applied to Fig 15 are exactly the same as those applied to Figs 11, 12, and 13 (see corrections for pages 45, 46, and 47).
53	On line 14 replace the equation $b \simeq 0.05$ Å by the equation $b \simeq 0.04$ Å. Delete lines 15 to 18 (including eq 30) and replace by the following: "The Doppler width Δm in fractions of an order number is derived from eq. 11 (30) $m = -2\frac{(\Delta\lambda)h}{\lambda_o^2}$ For $b \simeq 0.04$ Å the Doppler width is calculated to be about 0.05 order." Please note that because the incorrect Doppler half width (b = 0.07 order) is used to define the Source function S(m) in the text of the thesis, further corrections involving S(m) are necessitated (see corrections for pages 54 to 58).
54	On line 10 replace b = 0.07 order by b = 0.05 order.
54 56	Delete the second paragraph in section c-4 and replace it by the following paragraph: "The computed Instrumental function W(m) is shown in Fig 55 compared with the functions A(m)*F(m) and A(m). It is observed that the contours of A(m)*F(m) and W(m) are identical at the peak. Thus the Airy and Pinhole effects constitute the main sources of peak broadening. By using a smaller pinhole and a smaller air gap h, the broadening may be diminished to such an extent that the Airy width will dominate the peak broadening; then use of higher reflection coefficients will reduce the Airy peak width so that the Surface Defect functions become the limiting factors in peak broadening."
55	The function A(m)*S(m) in Fig 16 is incorrect. Fig 16 must be replaced by Fig 54 showing the correct function A(m)*S(m).

Page No.	Corrections
57	Because S(m) as calculated in the text is incorrect, Fig 17 should be deleted (including all references to Fig. 17).
58	Fig 18 must be replaced by Fig 55 which shows W(m) as calculated using the corrected function S(m).
155	On line 2 insert the following sentences after the sentence ending with "0.004 order.": "Since water vapor constitutes less than two percent of the atmosphere by volume, then under laboratory conditions in the Denver area, the index of refraction will be decreased by an amount less than 10^{-6} from that of dry air. If the humidity change does not cause the water-vapor content to exceed the two-percent figure, the corresponding refractive index change will be less than 10^{-6} causing the peak to shift by 0.006 order." In sec b-2, the last sentence which reads, "Thus the order change . . . . . will not be considerably affected.", should be deleted.
156	On line 21 replace the figure 0.002 by the figure 0.001 so that the sentence reads, "Examination of each of the resultant peaks . . . . . of the peak is about 0.001 order." At the end of sec b-3 add the following paragraph: "Since the peak width is less than 0.03 order, the broadening due to transmission of extraneous lines is negligible. On the other hand the peak shift of 0.001 order is not negligible because it must be added to the peak shift caused by refractive-index changes. Thus for a scan of 15 orders, the total error contributed by the peak width (0.002 order) and the peak shift (0.011 order) is 0.013 order so that the relative uncertainty calculated by the least-square method still holds."
166	On line 7 replace the phrase, "merge above the magnitude at one half the peak", by the phrase, "merge at about 0.4 of the peak magnitude."
167	Replace Fig 51 by Fig 56.
171	Delete the entire paragraph beginning with the phrase, "Another important result . . . . . ." and replace it by the following paragraph:

Page No.	Corrections
171	"Another important result to come out of the error analysis (Ch. V, sec b-2 and sec b-3) is that the peak shift contributed the largest error for the specific interferometer used. Refractive-index variations caused by pressure, temperature, and humidity changes accounted for the largest portion of the peak shift. If the interferometer is operated at a constant temperature (20°C for instance) so that water vapor constitutes less than two percent of the air by volume, then the most serious source of error, humidity changes, can be kept within acceptable bounds. For more accurate calibrations the present interferometer can be made less sensitve to the index-of-refraction changes by decreasing the plate spacing."

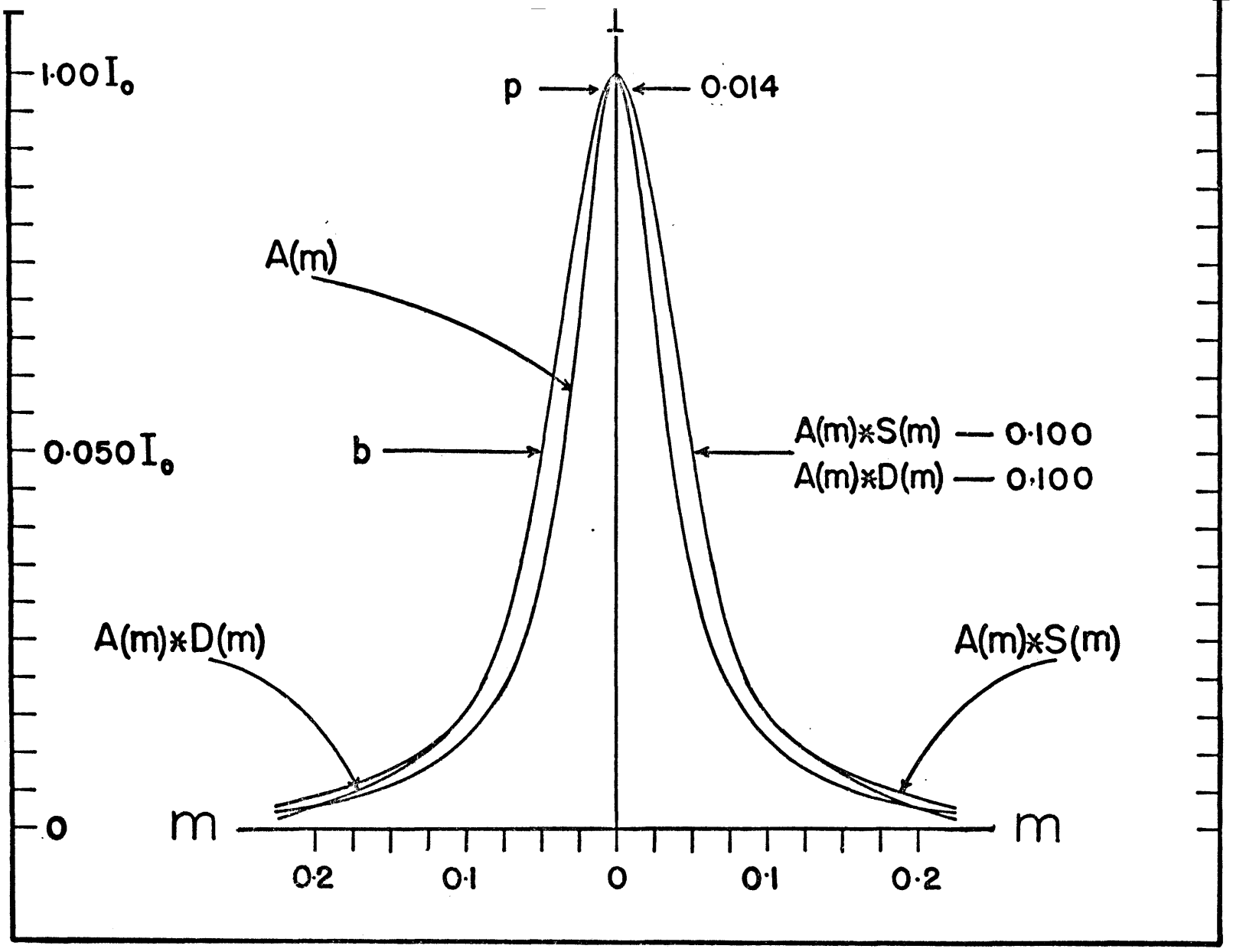

Figure 54. The Functions A(m)*S(m) and A(m)*D(m) where $D(m) = D_p(m)*D_s(m)*D_g(m)$

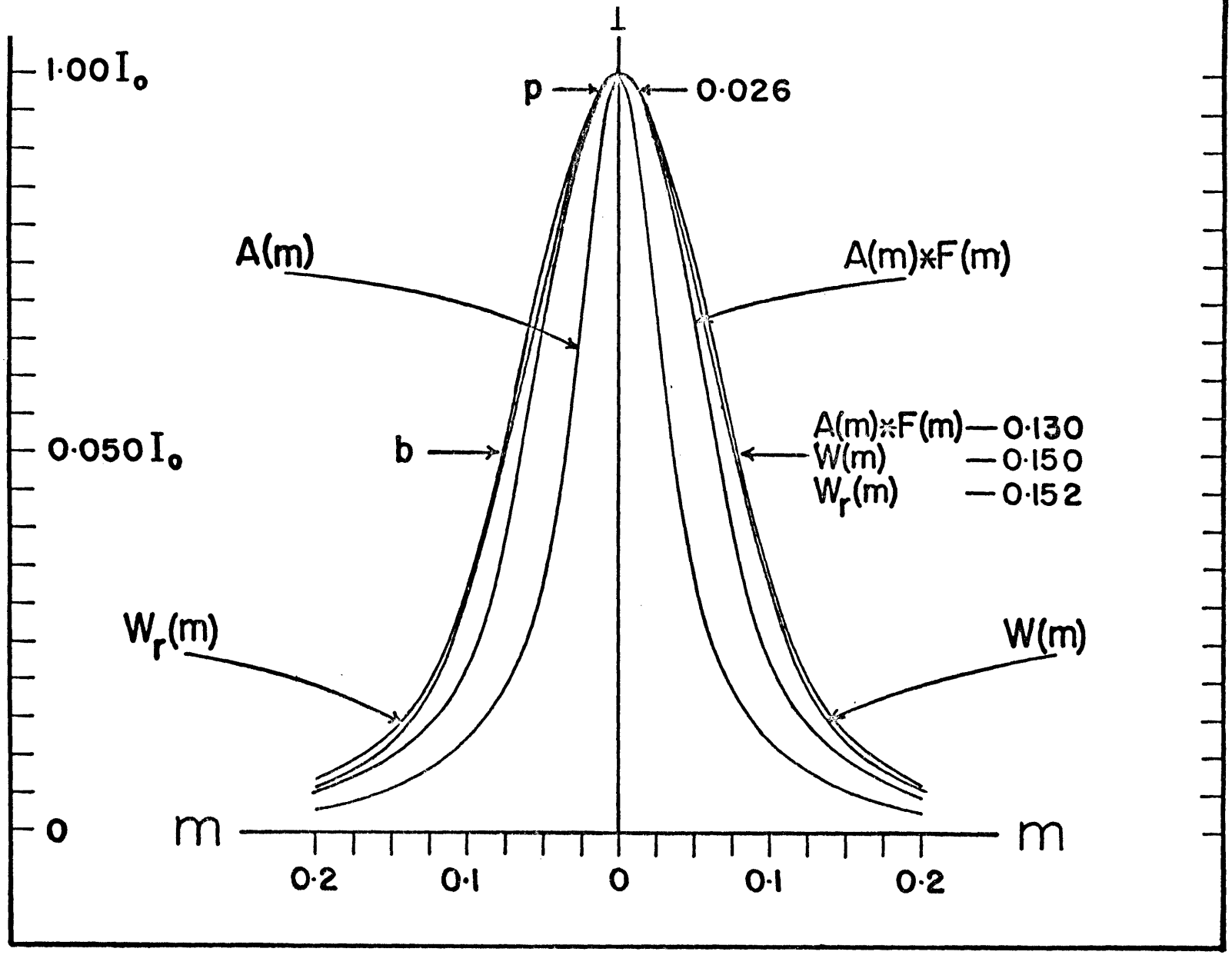

Figure 55. Instrumental Functions, W(m) computed when there is no rotation of the optical flat and $W_r(m)$ computed when there is a 0.09 arc-sec rotation of the optical flat, are compared to the function A(m)*F(m)

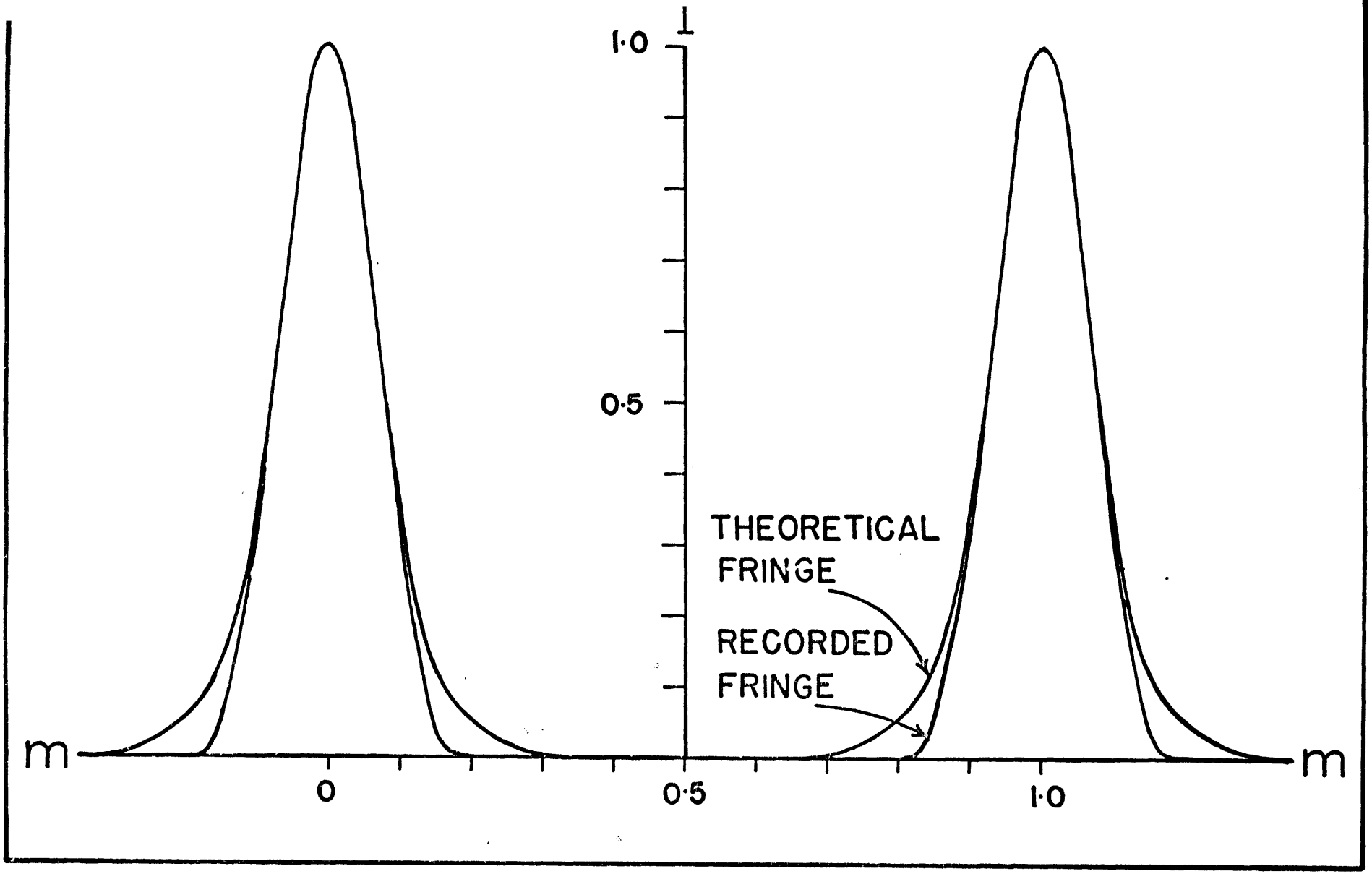

Figure 56. Comparison between an average recorded fringe and the theoretical fringe computed when the moving optical flat has rotated through an angle of 0.09 arc sec.

ADDITIONAL COMMENTS

Most of the conclusions stated in sec. c-4 of ch. II were based on the use of an air gap of thickness 1½ mm. However, due to an error of a factor of ½ in the calculation of the pinhole diameter and in the half width of the Pinhole Function (see Errata, p. 49 and p. 53), the half width of the Source Function is one half of that calculated in the text (see eq. 30 on p. 53). Hence, the interferometer is not as sensitive to the temperature at the source as was previously demonstrated. In ch. V, sec. C, the recorded and the theoretical fringes are compared. The theoretical fringe W(m) was computed from data based on the Source Function having a half width of 0.07 order. However, as shown in the section on Errata, the Source Function has a half width of less than 0.035 order so that the theoretical fringe plotted in fig. 51 is narrower than that of the recorded fringe. One may then conclude that there may be other appreciable sources of broadening in the interferometer, yet to be accounted for.

March 4, 1968

ACKNOWLEDGMENTS

The author wishes to thank Dr. Maurice W. Major and Dr. John V. Kline for their many critical discussions. The author is also grateful to Mr. Jack Kintner for his assistance and advice in assembling the instrument, and Mr. Russell Gray for the computer program required to calculate the fringe contours.

This work was supported by the Environmental Science Service Administration under contract C-176-65(G).

I. INTRODUCTION

Until recently quantitative studies of earth strains have been handicapped by the lack of a sufficiently accurate method for calibrating the transducer of the strainmeter. This thesis will describe a continuously recording interferometer that has calibrated the transducer to one part in one hundred.

A. The Strainmeter and Its Calibration

The continuous observation of rock strain over long periods of time has taken on importance in the study of earth tides, long period waves from seismic disturbances, and earthquake prediction. A strainmeter that measures earth strain was first successfully built in 1935 by Benioff (1959). In recent years interest in this instrument has been renewed with its installation in a deep mine in Ogdensburg, N. J. (Major and others, 1964). Since 1964 several of these strainmeters have been installed and

operated in California and the Denver area by the Colorado School of Mines (CSM).

The strainmeters used by CSM consist of a horizontal length standard, built of quartz tubing, which extends over a distance of 100 ft. One end of the quartz tube is buried in a cement cap that is attached to bedrock. On the free end of the quartz tube is mounted a single capacitor plate placed between a pair of parallel capacitor plates of a transducer bolted to a cement pier. Any expansion or contraction of the rock in the 100-ft distance which the strainmeter spans will move the central capacitor plate relative to the outer capacitor plates. This movement unbalances a capacitance bridge and generates a signal voltage that is read out on a continuously running pen recorder.

Measurement of earth strain by the extensometer requires the measurement of two quantities: (1) Measurement of the strainmeter span with a steel tape to about a 1-percent accuracy, (2) Measurement of the displacement of the central capacitor plate relative to the outer capacitor plates of the transducer. Because the accuracy of the strain measurement is limited by the 1-percent measurement of the quartz tube length between two points on the ground, it is desirable to know the relative movement of the central plate to 1 percent also. The calibration is achieved by displacing

the transducer capacitor plates a predetermined distance and observing the corresponding output.

Two methods have been used to calibrate the strainmeter transducer in installations run by CSM. The earlier of the two calibrations was performed by displacing the quartz tube with a micrometer screw and observing the movement with a microscope containing a micrometer eyepiece. This method has several drawbacks. For example the smallest movements that could be observed were about ¼μ; and to obtain a reasonably small relative uncertainty, movements from 6 to 10μ had to be produced. Two things were wrong with the foregoing method. First such movements went beyond the linear range of the instrument, and second they were 6 to 10 times the expected measurement range of the strainmeter. The presence of an operator next to the transducer caused displacements in the transducer due to thermal disturbances and strain and tilting of the cement pier. Nevertheless 15-percent calibrations were achieved, and it was determined that strains of about ½μ in 100 ft were associated with the earth tide.

The second method now used at CSM provides a better calibration of the strainmeter. In this method the conventional transducer is replaced by a device that uses a differential screw (Lansing Research Corp., 1965, p. 17-19)

and a parallelogram (discussed in more detail in ch. III). This unit (Romig, 1967) provides a small "known" movement for the strainmeter and is read out on the transducer recording system as a voltage change. The screw is nominally rated by the manufacturer to produce a linear displacement of 250μ in. per revolution. The movement transmitted to the transducer capacitor plates is 1/10 of the movement produced by the screw at the driven end of the parallelogram. Remote operation of the screw, through a motor and a worm gear, causes the capacitor plates to move with a velocity of about 6¼μ in. per min. Figure 1 is a drawing of this transducer.

This transducer has proven to be precise, but its accuracy is not known. For example, as the transducer plates are displaced, the load exerted by the hinged parallelogram on the screw increases so that the displacement of the plates may not be a linear function of the screw displacement. One may also question the ability of the parallelogram to transmit 1/10 the motion of the screw to the capacitor plates. Consequently it is desirable to determine the movement of the plates in terms of a fundamental length standard.

B. The Wavelength of Light as a Length Standard

One method of calibrating displacement measuring instruments is to provide a known controlled movement with a

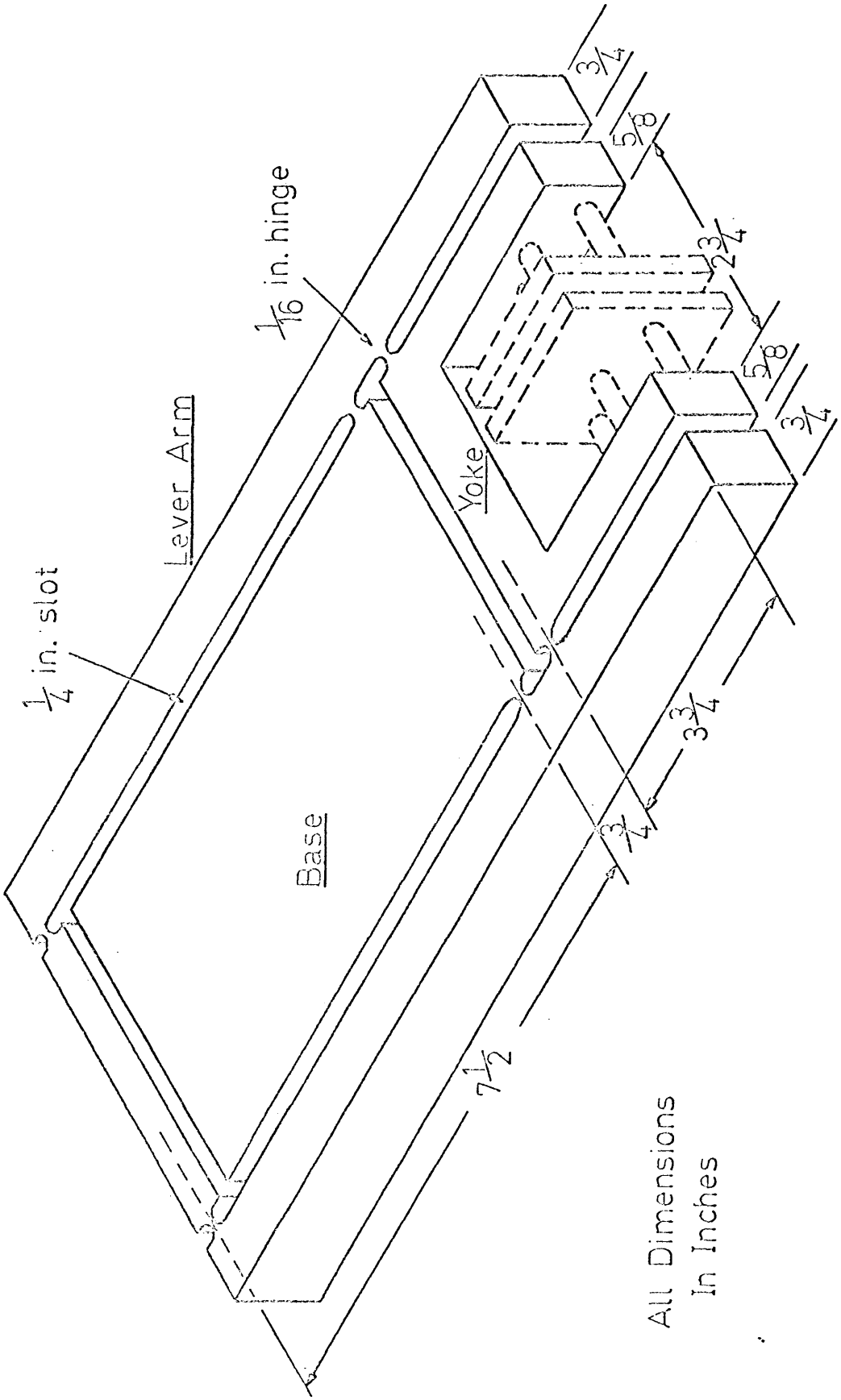

Figure 1. Drawing of the Strainmeter Transducer.

device that has already been calibrated. A second method utilizes a length standard to measure an unknown input displacement directly.

The strainmeter transducer is an example of the first approach where a "known" controlled movement is used to calibrate the strainmeter. Because it is easily built and relatively inexpensive, the strainmeter transducer is being used at all sites operated by CSM. This paper describes the second method, the use of a length standard, the wavelength of light, to measure the unknown displacement directly.

In 1960 the International Conference on Weights and Measures adopted the resolution that the meter is to be defined as equal to 1,650,763.73 wavelengths of the orange red line of Kr_{86} (Francon, 1966, p. 270). The previous definition of the meter, the distance between two inscribed lines on a platinum iridium bar kept in the archives in Sevres France, became obsolete because of the advantages inherent in the measurement of the wavelength of light. Accuracy in wavelength measurements has reached one part in 10^8 (Wildhack and others, 1965, p. 130, 131) (the unknown line is measured by comparing it with the standard orange red line of Kr_{86}). Length can be measured with the wavelength standard with an accuracy of four parts in 10^7 (Wildhack and others, 1965, p. 6, 7), and the precision in this measurement is 50 times

better than the precision in measuring the meter between two inscribed lines (Francon, 1966, p. 270). Furthermore the wavelength of light is indestructable; and finally, the access to light-wave standards is easier than access to the primary platinum iridium standard, only one of which exists.

Not all spectral lines can be used as length standards. In recent years three specific wavelengths have been considered as possibilities in defining the meter. These are the red line of Cd, the green line of Hg_{198}, as well as the orange red line of Kr_{86}. To be selected as a length standard, the line must be a single, isolated line which is narrow and sufficiently intense.

Many lines are excluded because they exhibit complex structure due to the presence of several isotopes of the same element. Furthermore wavelengths emitted from sources consisting of a single isotope having an odd mass are excluded because of their hyperfine structure.

Once the condition that the source be a single isotope of even mass is satisfied, additional experimental conditions must be met to reduce line broadening due to the Doppler and pressure effects. These conditions require a light source containing gases of large atomic mass at low temperatures and low vapor pressures. An example of such a light source is the Kr_{86} lamp described by Englehard

(1957, p. 19). The lamp is operated at the triple point of nitrogen (120°K and a few hundredths of a torr of pressure). Under these conditions the wavelength scale has an uncertainty of less than one part in 10^8 at any point on the scale. To display the wavelength scale, the Fabry-Perot interferometer is used because of its high resolving power (Meissner, 1941, p. 405).

C. Choice of the Fabry-Perot Interferometer

The logical choice of an instrument to calibrate the strainmeter transducer is the Fabry-Perot interferometer because it will produce sharp narrow fringes required for accurate length measurements.

The interferometer consists of two glass plates that are partially silvered and set parallel to each other. Figure 2 is a schematic diagram of the interferometer. In its operation monochromatic light from a source S illuminates the optical system so that the light rays will be propagated through the system normal to the optical flats F_1 and F_2. A pinhole is placed at the focal point of the first lens L_1 so that all rays passing through the pinhole are bent by the lens, perpendicular to the flats. When the light enters the gap between the flats, the rays will be multiply reflected between the silvered faces and partially

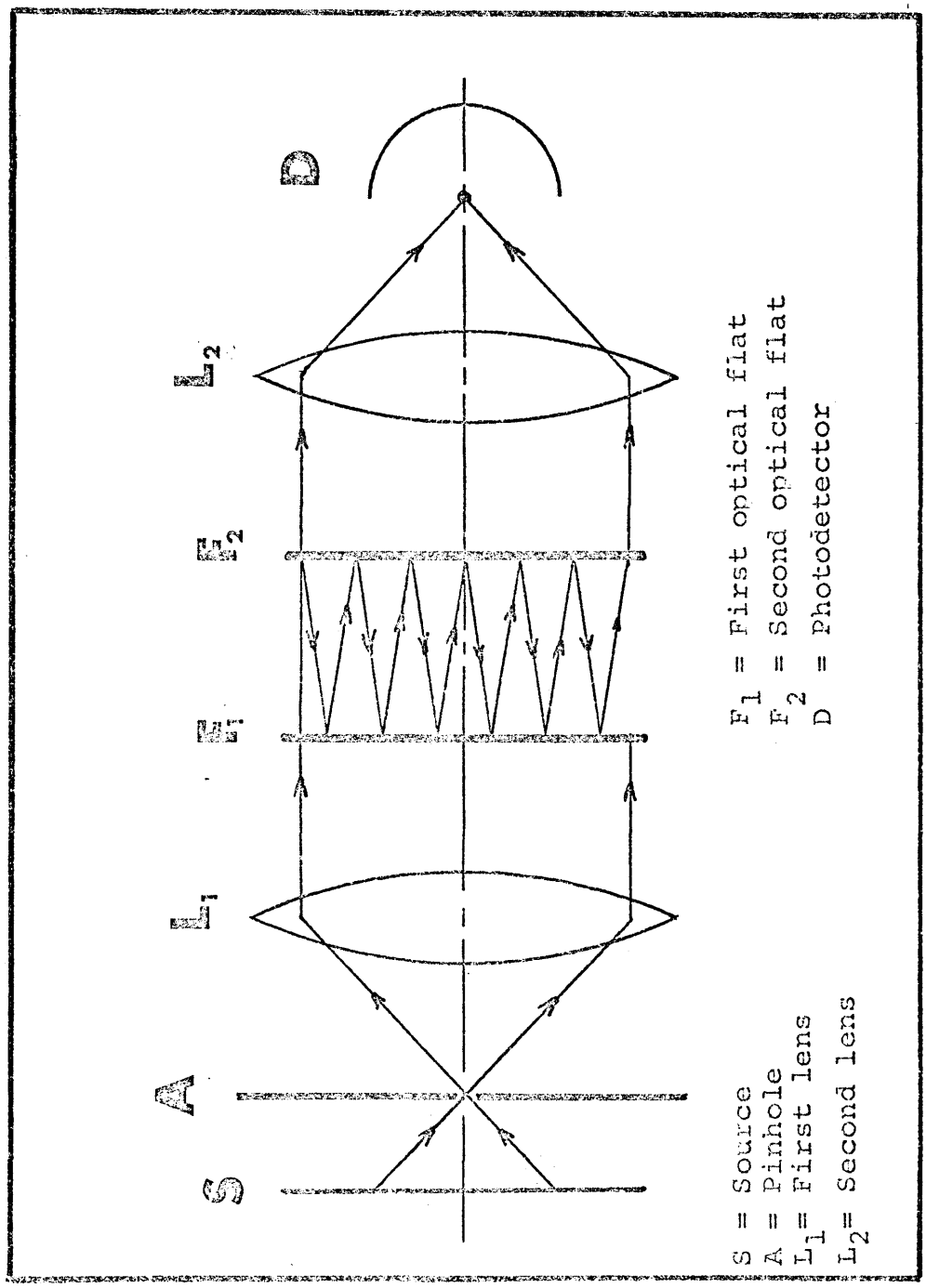

Figure 2. Diagram Illustrating the Operating Principles of the Fabry-Perot Interferometer.

transmitted to the second lens L_2, which focuses the light onto the photocell D. (Although the rays are normal to the plates, they are shown in fig. 2 to be inclined at an angle to the normal of the flats in order to demonstrate the multiple reflection of these rays between the flats.) The interference between many beams produces sharper fringes than two-beam interference, as will be shown in ch. II, sec. b-2. When the spacing is exactly equal to an integral number of half wavelengths, the rays emerging from the flats will interfere constructively so that the intensity measured by the photocell will be a maximum. If one of the flats is displaced several half wavelengths, a sequence of peaks will be recorded. A scan through each peak represents a half wavelength ($\lambda/2$) of movement.

With the extreme accuracies inherent in length measurements through interferometry, it is not surprising to find that this tool has attracted the attention of several investigators. Blayne and Gillman (1965) adapted a Fabry-Perot interferometer to measure the position of the quartz tube of the strainmeter with respect to the ground. They then applied these measurements to the calibration of a conventional strainmeter transducer. A laser source was used in conjunction with a multiple beam interferometer to sample earth strains at distances of ten meters (Vali and

others, 1965). Finally a third author (Kane, 1966) proposed the use of fiber optics and interferometry for the measurement of earth strain. One of the chief advantages here is the low cost of building such a strainmeter.

In the above interferometric applications, the interferometers were employed directly in the measurement of earth strain. Because the screw operated strainmeter transducer is the secondary calibration device for the CSM strainmeters, the interferometer described here is operated at a separate installation as the primary calibration device.

Until recent years Fabry-Perot interferometers (called etalons) have been almost exclusively constructed with fixed spacers separating the Fabry-Perot plates. Few mechanical scanning interferometers had been built because of the difficulty of producing accurate parallel motion of the plates (Born and Wolf, 1965, p. 330). Nevertheless the movable Fabry-Perot interferometer presents certain advantages in its application as a length transducer. It allows one to avoid the conventional photographic technique which employs the method of exact fractions (Candler, 1951, p. 217-220) for calculating the plate separation. This method is both cumbersome and tedious to use. On the other hand the variable spacing interferometer permits one to read the displacement of the plate directly from the chart because a

scan through a recorded peak represents $\lambda/2$ movement of the plate.

In recent years several articles have appeared describing mechanical scanning interferometers. For example Slater and others (1965) describe a rugged magnetostrictive scanning Fabry-Perot interferometer to be used in space research, and Bruce (1966) describes a feedback system used to maintain the plates parallel as they are displaced. One of the earliest designs that solved this parallelism problem was that of Kline (1952). Indeed Kline's interferometer has already been adapted by Bottom (1964) in the measurement of strain. Kline's basic design has now been applied in the construction of the Fabry-Perot interferometer which is used to calibrate the strainmeter transducer. In the remaining portion of this thesis, the theory and construction of the interferometer and its application as a primary calibration device for strainmeters will be described.

II. THEORY OF THE FABRY-PEROT INTERFEROMETER

In this chapter the theoretical laws describing the operation of the "ideal" Fabry-Perot interferometer are developed. From these laws are deduced three advantages that this instrument offers as a displacement transducer. They are:

(1) The Fabry-Perot interferometer records sharp narrow peaks when illuminated with monochromatic light,

(2) The relationship between the position of the recorded peaks and a displacement of one of the interferometer plates is linear,

(3) A photocell can be used to monitor the intensity change.

In the final portion of this chapter the conditions under which the "real" Fabry-Perot interferometer operates are examined, and an analysis of the resulting uncertainties is made. The accuracy of the interferometer absolute length scale is calculated, and suggestions are offered on how to reduce the calculated uncertainties if a greater accuracy

than is now available in the present instrument is required.

A. Intensity Distribution of the Transmitted Interference Pattern

The Airy Formula describing the transmitted intensity distribution through two parallel plates is derived in most texts on optics (Rossi, 1957, sec. 3-10). Nevertheless the standard development of the Airy Formula is reproduced below in order to present to the reader a handy means for future reference.

a-1. Development of the Airy Formula

In the rigorous theory describing the interference phenomena observed with parallel plates, the incident radiation is represented by the real part of the complex quantity

$$\bar{E} = E_o \bar{e}_o \varepsilon^{\,i(\omega t - \psi)} \tag{1a}$$

where $\bar{E}$ is the incident electric field vector ($\bar{E}$ is identified as the light vector) (Rossi, 1957, p. 378).

E_o is the amplitude of the incident ray,

ω is the angular frequency in radians/sec,

t is the time in sec,

$\bar{e}_o$ is the unit vector defining the direction of the electric field which is always normal to the direction along which the light disturbance is propagated.

ψ is the phase angle where $\psi = \frac{2\pi n_1}{\lambda_o} + \delta$ and λ_o is wavelength in vacuo of the incident radiation. n is the refractive index of the medium through which the light travels. The

quantity l is the geometric path over which the ray travels, and the quantity nl is known as the optical path s. δ is an arbitrary phase angle.

The vector property of $\bar{E}$ is not essential to the development of the Airy Formula. As is the practice in most optic texts, the unit vector $\bar{e}_o$ will be dropped with the understanding that the resulting expression is still a vector perpendicular to the direction of the light beam. One thus has

$$E = E_o \varepsilon^{i(\omega t - \psi)} \tag{1b}$$

To begin, a single ray described by eq. 1b is allowed to fall on two parallel plates that are assumed to be identical in their optical properties (see Fig. 3). The material separating the plates has a refractive index n which is assumed to be constant in the initial development. Furthermore the material composing the plates is assumed to have a greater refractive index than that of the medium between the plates. Assume the plates are of infinite extent with the spacing h. In the final simplifying assumptions, absorption of the incident energy is considered negligible, and the first ray incident on the second plate in Fig. 3 is allowed to have an arbitrary phase angle δ of zero.

The resulting amplitudes of the rays emerging from the parallel plates are first considered. If τ is the fraction

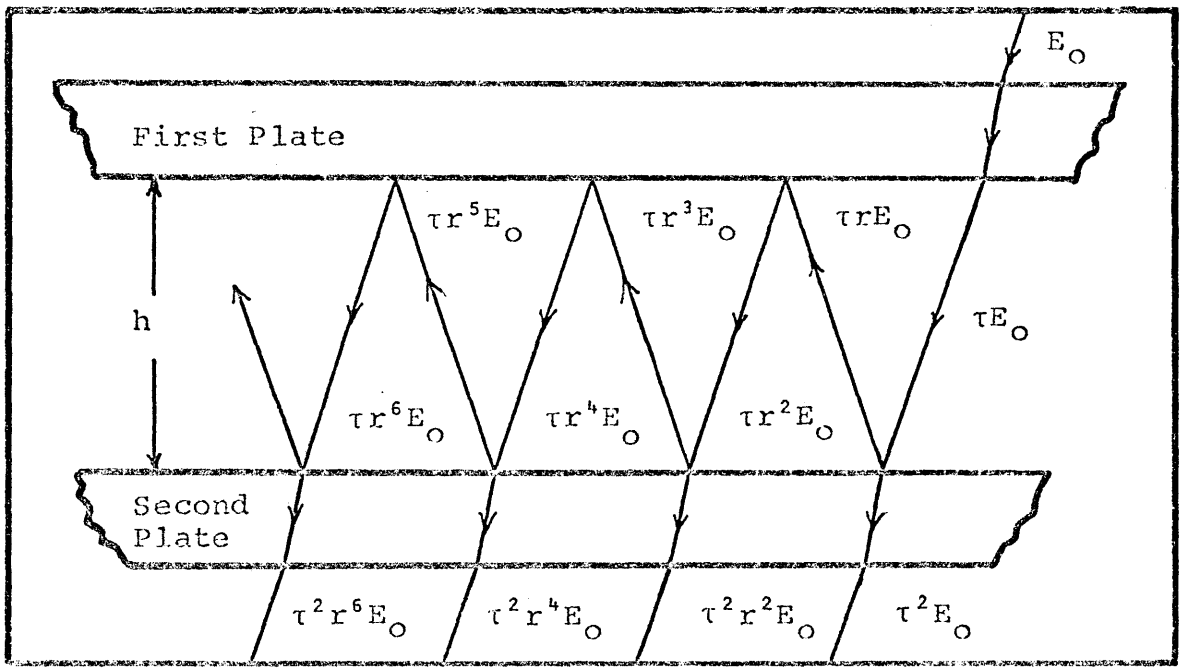

Figure 3. Multiple Reflection and Transmission of Light Rays Through Two Parallel Plates.

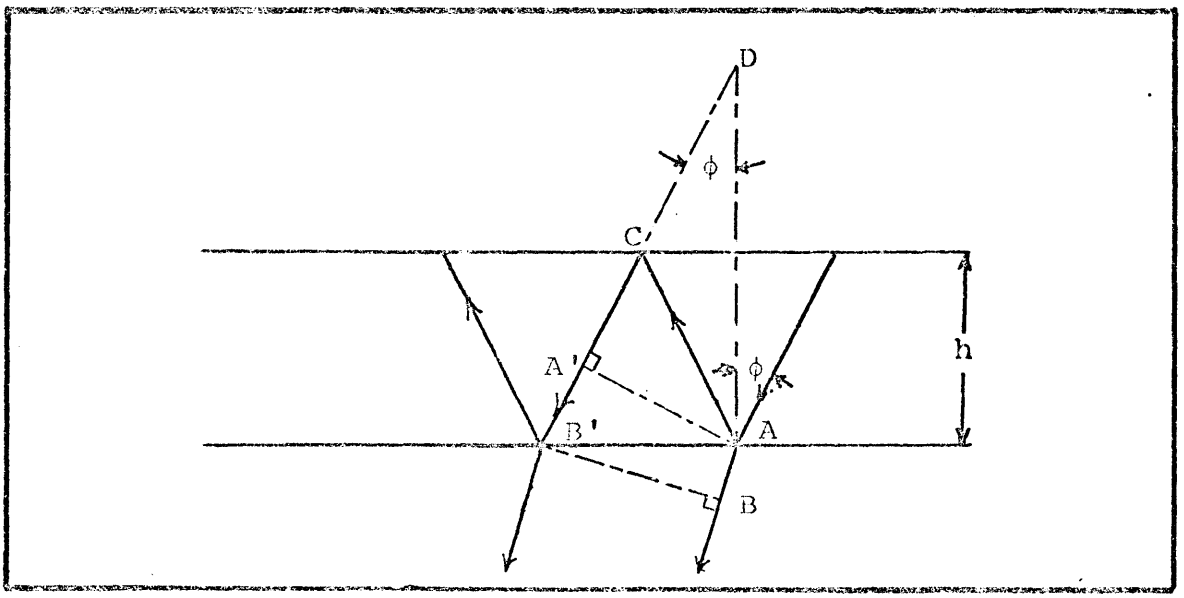

Figure 4. The Path of the Interfering Rays in the Fabry-Perot Interferometer.

of the incident amplitude transmitted through either plate, and r is the fraction of the amplitude in the gap reflected at either plate, the resulting amplitude of the rays emerging from the plates takes the form

$$\tau^2 E_o,\ \tau^2 r^2 E_o,\ \tau^2 r^4 E_o,\ \ldots\ \tau^2 r^{2(K-1)} E_o$$

One notes from fig. 3 that a ray incident at the second plate in the gap will be divided into two parts, one transmitted directly through the second plate and one twice reflected between the plates. The latter ray is subsequently transmitted partially by the second plate into the surrounding medium, where it interacts with the first transmitted ray. A phase change results as a consequence of the additional optical path that the reflected ray must traverse before it is superimposed on the first ray. Also, due to the reflection, a phase change of π will be imposed on the electric field vector at each plate, but the resultant phase change 2π for the double reflection adds nothing to the total phase angle.

Thus each emerging ray will have its phase increased from that of the previous ray by the amount $\psi = \frac{2\pi}{\lambda_o} s$. Consequently the light beam leaving the parallel plates can be represented as being composed of an infinite number of light vectors

$$(2)\quad E_o\tau^2\varepsilon^{i\omega t},\ E_o\tau^2 r^2\varepsilon^{i(\omega t-\psi)}\ \ldots\ E_o\tau^2 r^{2(K-1)}\varepsilon^{i\{\omega t-(K-1)\psi\}}$$

When the Principle of Superposition is applied, the total amplitude transmitted is

$$E = \tau^2 E_o \varepsilon^{i\omega t} \sum_{K=1}^{\infty} (r^2 \varepsilon^{-i\psi})^{K-1} \tag{3}$$

Eq. 3 is a geometric series, and since $r<1$, the result is

$$E = \frac{\tau^2 E_o}{1-r^2\varepsilon^{-i\psi}} \varepsilon^{i\omega t} \tag{4}$$

The resulting intensity distribution is computed by multiplying eq. 4 by its conjugate E^*.

$$E \cdot E^* = \frac{\tau^4 E_o^2}{1-2r^2\cos\psi+(r^2)^2}$$

$$I = \left\{\frac{\tau^2}{1-r^2}\right\}^2 \frac{I_o}{1+\frac{4r^2}{(1-r^2)^2}\sin^2\frac{\psi}{2}}$$

Because the intensity is directly proportional to the amplitude squared, I_o and I, which are the intensities observed to enter and leave the parallel plates, are each respectively proportional to the quantities E_o^2 and $E \cdot E^* = E^2$. Similarly τ^2 is the fraction of the incident intensity transmitted through each plate and is called the transmission coefficient T. Analogously r^2 is called the reflection coefficient R. Hence the expression for the intensity distribution becomes

$$I = \frac{T^2}{(1-R)^2} \frac{I_o}{1+\frac{4R}{(1-R)^2}\sin^2\frac{\psi}{2}} \tag{5}$$

where

$$\psi = \frac{2\pi}{\lambda_o} s$$

In the absence of absorption, one has from the Conservation of Energy Principle

$$R + T = 1$$

whence eq. 5 transforms into the Airy Formula

$$(6a) \quad I = \frac{I_o}{1 + \frac{4R}{(1-R)^2} \sin^2 \frac{\psi}{2}}$$

In the final step of the derivation, the phase angle ψ is computed, and the intensity distribution I is shown to depend on the plate spacing h.

In fig. 4 one constructs the wavefronts AA' and BB', which represent the phase condition of the light disturbance at the time instants t and t', when rays AB and CA'B just leave the gap and enter the second plate at points A and B' respectively. In the time $\Delta t = t - t'$ required for the disturbance to travel from positions AA' to BB', the reflected ray must traverse the geometric distance,

$$l = AC + CA'$$

To compute the distance l a perpendicular is constructed from the plate surface AB' at A so that it meets the line B'A' at D. If ϕ is the reflecting angle, then the angle $ADB' = \phi$. From the geometry of fig. 3 AC = CD whence l

becomes

$$l = CD + A'C$$

$$l = 2h \cos\phi$$

The optical path difference is then

(6b) $$s = 2nh \cos\phi$$

so that the phase angle becomes

(6c) $$\psi = \frac{4\pi}{\lambda_o} nh \cos\phi$$

With eq. 6c the derivation of the Airy Formula is now completed, and it is noted that I is indeed dependent on h. The observation is also made that, when $\psi = 2\pi m$ (m = integer), the intensity transmitted will be a maximum and equal to the incident intensity I_o.

If high reflection coatings are used at the plate surfaces, the interferometer will record sharp narrow peaks, as will be demonstrated in section b-2. High reflectivities are produced inexpensively by coating the plates with metal films. With these coatings two of the suppositions used to derive the Airy Formula no longer hold. Section a-2 considers how the Airy Formula is to be modified when metal films are used.

a-2. Corrections Applied to the Airy Formula

Metal coatings used as reflecting surfaces introduce two conditions not previously considered. First the phase

change due to reflection is not exactly π, and second, an appreciable portion of the incident intensity will be absorbed by the film.

A phase change $\pi + \alpha/2$ is produced at each reflection, and the phase change is found to depend on the angle of reflection and the wavelength. The correction to be applied enters into the phase angle (eq. 6c) which then becomes

$$(7) \qquad \psi' = \frac{4\pi}{\lambda} nh \cos\phi + \alpha = \psi + \alpha$$

Because the interferometer is to be used with monochromatic radiation incident normally on the parallel plates, the phase angle α will only serve to shift the position of the fringes by a constant amount changing the effective spacing h between the plates. As a displacement transducer, the interferometer measures differences between consecutive positions of the plates, and therefore no error will be produced because of the phase shift.

The correction applied to eq. 5 when absorption is considered is obtained from the Conservation of Energy Principal where

$$R + T + A = 1$$

and A is the fraction of the intensity absorbed by the film so that eq. 5 becomes

$$(8) \qquad I = \left(1 - \frac{A}{1-R}\right)^2 \frac{I_o}{1 + \frac{4R}{(1-R)^2} \sin^2 \frac{\psi'}{2}}$$

Equation 8, a modified form of eq. 6a, shows that the effect of absorption is to reduce the transmitted intensity by the factor $\left(1 - \frac{A}{1-R}\right)^2$. This makes the position of the peak more difficult to locate but does not change the position of the peak.

The corrections described by eqs. 7 and 8 will not affect the form of the intensity contour and consequently eq. 6a will continue to be used to describe the interferometer as a displacement transducer.

a-3. Fringe Geometry

It is noted in eq. 6a that the phase angle ψ, eq. 6c, determines the intensity distribution of the transmitted interference pattern. If the interplate spacing h is held constant and the interferometer is illuminated with monochromatic light of single wavelength λ_o, the angle of inclination ϕ will determine the zones of equal intensity (fringes). Equation 6a does not specify any particular geometric configuration under which these zones of equal intensity will form. Instead the geometry of the fringes depend on the auxiliary lens system which is symmetric about the principal axis of the optical system. Thus the interference pattern will be projected as a set of concentric

rings whose centers, occurring at $\phi = 0$, lie at the intersection of the principal axis with the image plane. The geometry of the transmitted interference pattern is illustrated in Fig. 5. The radii ρ of these rings can be determined by the equation $\rho = f\text{Tan}\phi$ derived from the geometry of Fig. 5 where f is the focal length of the lens.

B. The Fabry-Perot Interferometer as a Displacement Transducer

By changing the phase angle ψ in the Airy Formula, the intensity I may be varied. Since ψ contains the parameter h, which specifies the position of the plates, it is obvious, then, that to design a displacement transducer, one must vary h (and thus ψ) while maintaining all other parameters in ψ, i.e. λ_o, ϕ, and n, constant. In this section a theoretical study is made of the form that the intensity distribution will take when only h is varied. From this study the benefits in using the interferometer to measure displacements are discussed, and the accuracy of these measurements is computed.

b-1. Linearity of the Interferometer Length-Measuring Scale

The Fabry-Perot interferometer provides a length-measuring scale that is linearly related to the spacing of

S = Extended Source
F_1 = First Optical Flat
F_2 = Second Optical Flat
L = Convex Lens
I = Image Plane
H = Circular Fringe Pattern

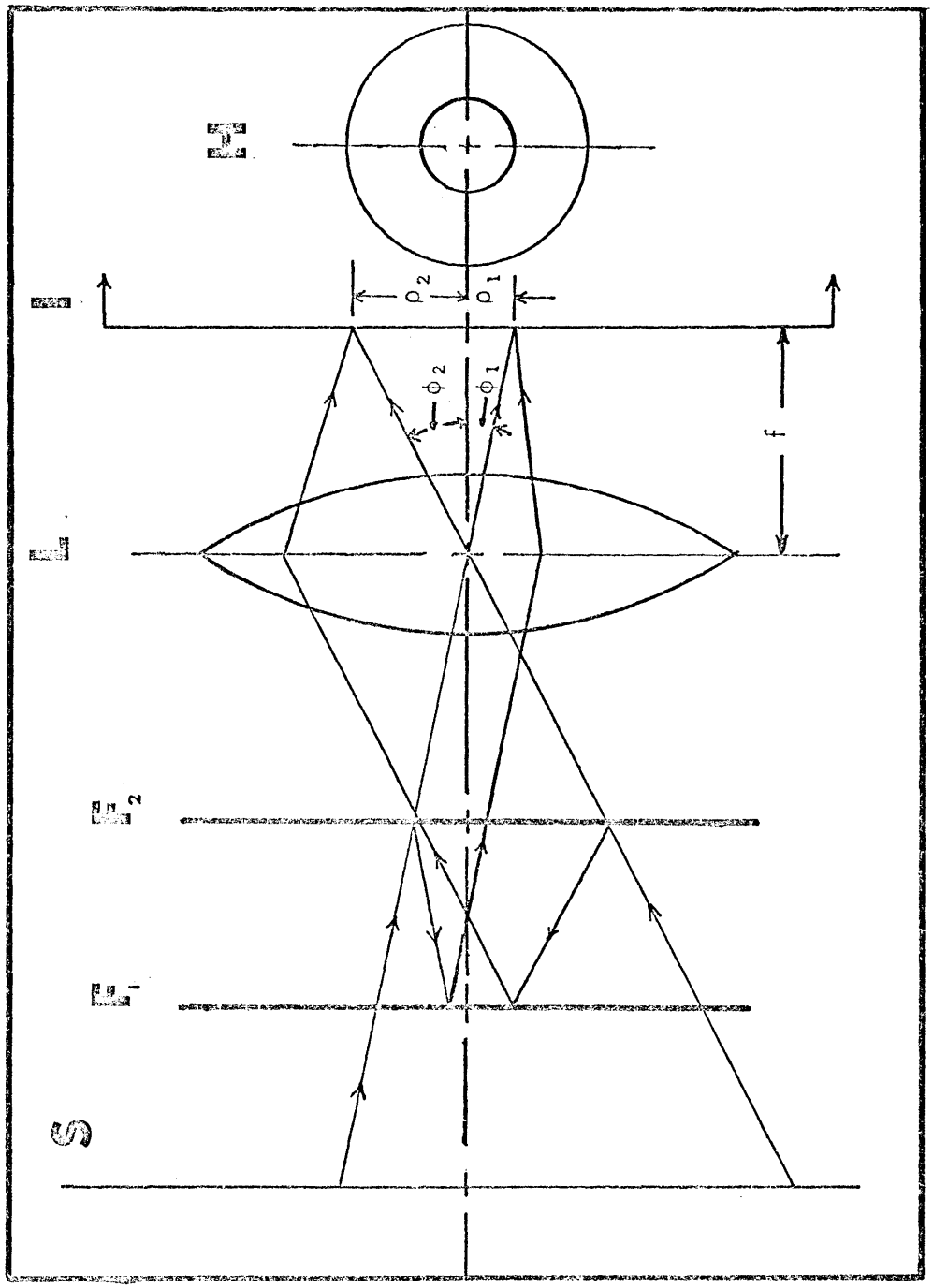

Figure 5. Formation of the Circular Interference Fringes in the Fabry-Perot Interferometer.

the interferometer plates as can be seen if one examines eq. 6c, which is restated for convenience.

$$(6c) \qquad \psi = \frac{4\pi}{\lambda_o} nh\cos\phi$$

By the use of monochromatic light and by restriction of the field of view to a small spot on the interference pattern, the quantities λ_o and ϕ can be kept constant. It is also assumed that the refractive index, n, of the medium between the plates does not change. Hence it follows that the phase angle ψ will then be a linear function of the interplate separation h. From section a-1 it was noted that fringes of maximum intensity will be produced when complete reinforcement of the superimposed rays occurs. This condition takes place when (in eq. 6a)

$$(9) \qquad \psi = 2\pi m \qquad (m = \text{integer})$$

Substitution of eq. 9 into eq. 6c yields the result

$$(10) \qquad m\lambda_o = 2nh\cos\phi$$

where the quantity m, called the order number, is directly proportional to h. Equation 10 is the basic operating equation of the Fabry-Perot interferometer. It describes the condition when two consecutive rays, emerging from parallel plates, will interfere constructively if the optical path difference between the rays equals an integral multiple

of wavelengths.

The physical interpretation of eq. 10 may be further simplified by making the medium between the plates air (n = 1.000) and monitoring the intensity change at the central zone of the interference pattern where $\phi = 0$. Hence eq. 10 becomes

$$h = \frac{m\lambda_o}{2} \tag{11}$$

Now if the thickness of the gap is an integral multiple of half wavelengths, the peak intensity will be transmitted at the central zone. Thus the order number m can be used to define the wavelength scale provided by the interferometer, e.g. when the separation distance of the plates is increased or decreased by a half wavelength, the order number will change to m+1 or m-1 respectively. The uncertainty in this scale is due to the finite width of the recorded peak. To minimize the undertainty the peaks are made as narrow as feasible.

b-2. Production of Sharp Narrow Peaks - Half Width and Peak Width

In sec. b-1 it was remarked that a broadening of the recorded peak would reduce the accuracy of the wavelength scale. It is in this situation that the Fabry-Perot interferometer displays its overwhelming advantage because it is

able to provide a wavelength scale exhibiting fringes having sharp peaks. To realize this advantage eq. 6 will be examined with respect to the fringe width as a function of the intensity distribution.

The parameter used commonly to specify narrowness of the fringes is the half width, b. It is defined as the width of the fringe calculated between points on its contour where the intensity is one half the peak intensity (see fig. 6 where the Airy intensity distribution, eq. 6a, is plotted against the order number m).

It is more useful to express the half width in units of order number rather than radians. First a general expression for the fringe width at any intensity I will be derived. If Δm represents the fringe width in fractions of an order number between two points on the fringe contour at intensity I , the phase angle at which the intensity I occurs is

$$\psi = 2\pi \left(m \pm \frac{\Delta m}{2}\right)$$

Putting the quantity $4R/(1-R)^2$ equal to F (the reflection finesse) eq. 6a is rewritten

$$I = \frac{I_o}{1 + F \sin^2 \frac{\psi}{2}}$$

Solving for ψ and then Δm one has

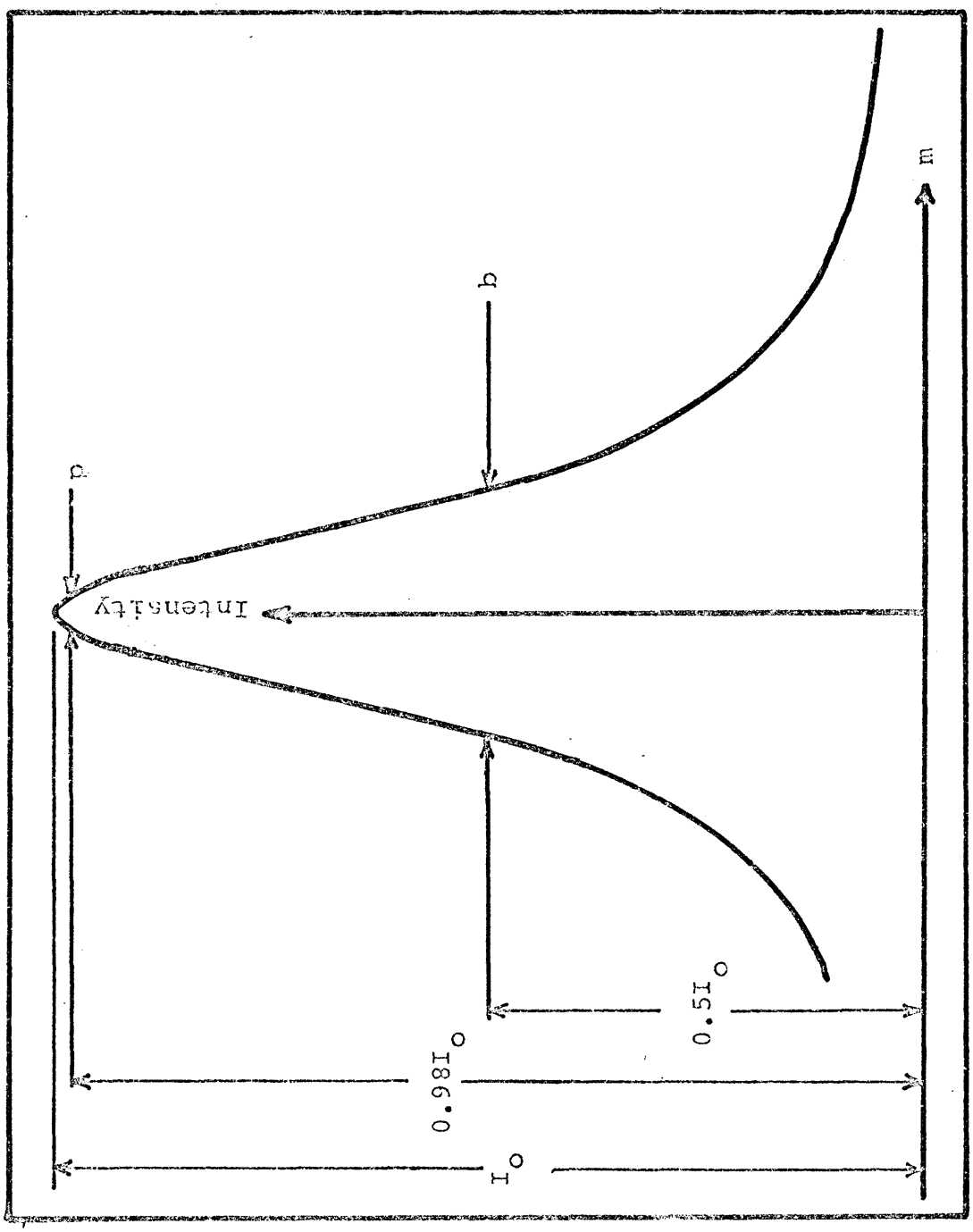

Figure 6. The Airy Intensity Contour of the Fabry-Perot Fringes.

$$\psi = 2 \sin^{-1} \left\{\frac{I_o - I}{F\ I}\right\}^{\frac{1}{2}}$$

$$\Delta m = \frac{2}{\pi} \sin^{-1} \left\{\frac{I_o - I}{F\ I}\right\}^{\frac{1}{2}} \qquad (13a)$$

when $I = \frac{1}{2} I_o$ the half width, b, is

$$b = \frac{2}{\pi} \sin^{-1} \frac{1}{F^{\frac{1}{2}}} = \frac{2}{\pi} \sin^{-1} \frac{1-R}{2\ R^{\frac{1}{2}}} \qquad (13b)$$

If one now allows R to approach unity, b becomes smaller, indicating a narrowing of the fringe. Another useful result occurs when high reflection coefficients are used. The "background" (the recording level between peaks) diminishes rapidly as the reflection coefficient approaches one.

When using metal films to obtain high reflectivities, one must also consider the loss of transmitted intensity due to absorption. In addition monochromatic light is usually obtained by filtering the input radiation. This filtering further reduces the available intensity. It is found that R = 0.8 will be about the highest reflection coefficient available in metal films which give large enough transmission coefficients (T = 0.1) (oral communication with J. V. Kline, 1967, CSM) to yield an observable interference pattern by photoelectric means.

To calculate the half width at R = 0.8, one has from eq. 13b, F = 80, whence

$$b = \frac{2}{\pi} \sin^{-1} \frac{1}{4x5^{\frac{1}{2}}}$$

and finally

$$b = 0.071 \text{ order}$$

In this paper a new quantity is introduced called the peak width. It is designed to describe the increase in uncertainty in locating the point of maximum intensity when the fringe is broadened near its peak. The peak width p is defined as the width calculated between points on the fringe contour where the intensity equals $0.98I_o$ (see fig. 6).

Therefore from eq. 13a

$$p = \frac{2}{\pi} \sin^{-1} \frac{0.141}{F^{\frac{1}{2}}} \tag{14}$$

for R = 0.8, F = 80, the peak width is

$$p = 0.011 \text{ order}$$

With a peak width of about 1/100 order, it is seen that about a 1-percent uncertainty will exist between consecutive divisions of the wavelength scale. This is the limit of the accuracy to be expected for the ideal Fabry-Perot interferometer when a coefficient of 0.8 is used.

b-3. Detection of the Intensity at the Central Zone

Since the central zone at $\phi = 0$ appears as a spot rather than a ring and since such an integral order contains about the same energy regardless of the angle ϕ, (Jaquinot,

1954) the central zone will be the most convenient place on the interference pattern from which the intensity change due to a movement of one of the plates may be monitored by a photocell. Also at the central zone, the factor cos ϕ in eq. 10 is unity. If in addition the medium between the plates is air, a displacement of one of the plates will be read out directly as a sequence of recorded peaks, where each represents a half wavelength of movement. Finally the central zone is conveniently isolated by centering a pinhole on the optical axis so that only radiation normal to the Fabry-Perot plates will be passed to the photocell.

b-4. Design of the Pinhole

When an optimum pinhole diameter is chosen, certain conflicting conditions must be resolved. It is desirable that the diameter should be small to limit the range of ϕ, and yet if it is too small, the intensity transmitted through the hole will be reduced. The correct sized pinhole will transmit maximum intensity provided by an integral order at the central zone. However any larger pinhole will become disadvantageous because the transmitted line will be broadened without an increase in the peak intensity.

Of the first two conditions the lower limit on the diameter can be determined experimentally when the intensity transmitted through the pinhole is just detected by the

photocell. On the other hand in determining the upper limit on the diameter, one must consider the finite angular width $2\Delta\phi$ subtended by the pinhole where the order change monitored by the photocell will be a function of $\Delta\phi$ as well as the displacement Δh of one of the interferometer plates. Consequently the upper limit on the size of the pinhole will be ascertained when radiation is just barely transmitted at its outer rim as the order number at $\phi = 0$ goes beyond an integer. Figure 7 illustrates transmission of radiation through the pinhole when plates are allowed to scan through 1/2 order alternately transmitting maximum and then minimum intensity.

In the third condition the Doppler effect causes the light source to emit radiation having a finite bandwidth $\Delta\sigma$ ($\sigma_o = 1/\lambda_o$). Therefore in addition to the angular width subtended by the central aperture, one must also account for any broadening of the fringe due to the presence of other component lines having wave number σ different from that of the presumed radiation σ_o by an amount $\Delta\sigma$.

In the development below the conditions of a finite range of ϕ subtended by the pinhole and radiation of a finite bandwidth $\Delta\sigma$ transmitted through the pinhole are used to calculate the optimum pinhole diameter.

At the center where $\phi = 0$ one has from eq. 10

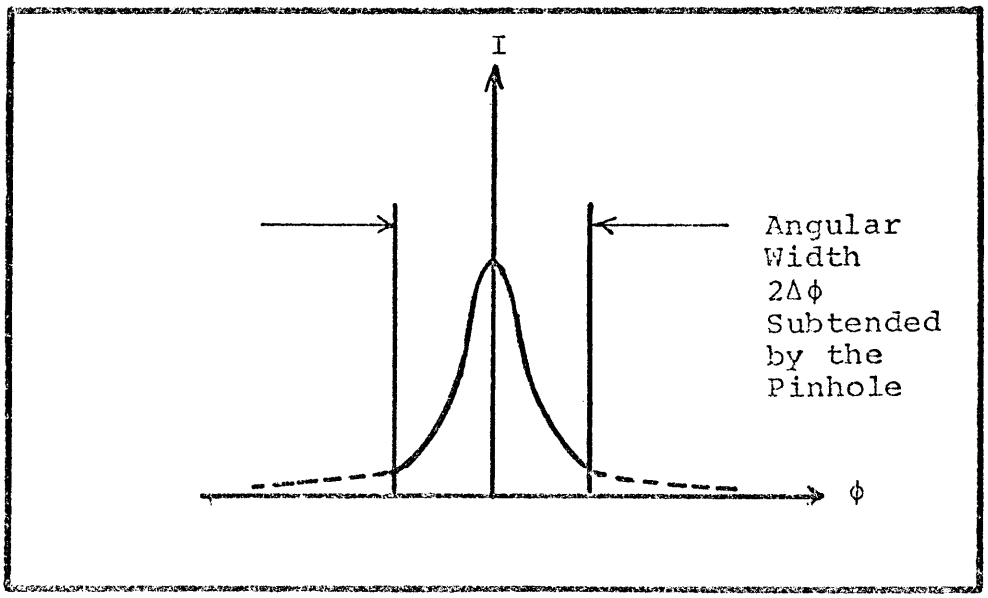

Figure 7a. Intensity Transmission through the Pinhole at an Integral Order Number.

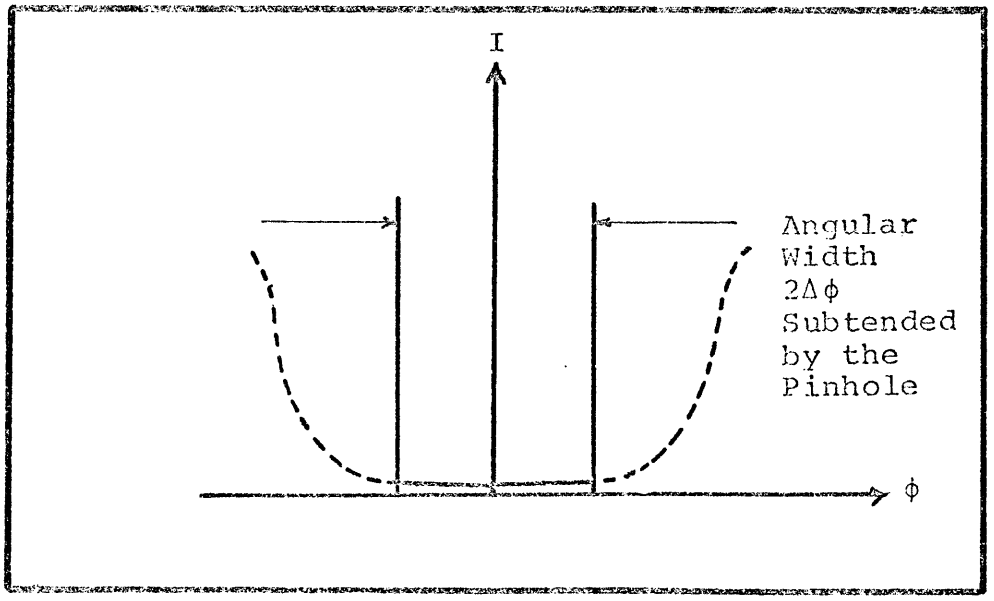

Figure 7b. Intensity Transmission Through the Pinhole at an Integral Order Number Plus One Half.

(15) $m = 2h\sigma_o$

At the outer rim of the pinhole the resulting order due to variations $\Delta\phi$ and $\Delta\sigma$ is

(16) $m-\Delta m \simeq 2h(\sigma_o+\Delta\sigma)(1-\frac{\Delta\phi^2}{2})$

where $\Delta\phi$ is small. Subtracting eq. 15 from eq. 16

(17) $\Delta m \simeq h\{\sigma_o\Delta\phi^2-2\Delta\sigma\}$

From eq. 15

(18) $\Delta m = 2h\Delta\sigma$

Equation 17 then becomes upon substitution of eq. 18

(19) $\Delta m \simeq \frac{1}{2}\sigma_o h\Delta\phi^2$

From Fig. 5 the diameter of the pinhole may be determined in terms of the focal length, f, and the pinhole radius ρ_p

(20) $\rho_p \simeq f\Delta\phi$

Then solving for $\Delta\phi$ and hence ρ_p one has

(21) $\rho_p \simeq f\ (2\lambda_o\Delta m/h)^{\frac{1}{2}}$

To specify the order change to be transmitted by the pinhole, Δm is arbitrarily chosen such that, when the central portion of the aperture transmits peak intensity, the outer rim will transmit 1/10 peak intensity. Thus one has by eq. 13a

$$\Delta m = \frac{2}{\pi}\sin^{-1}(\frac{9}{F})^{\frac{1}{2}}$$

$$\Delta m \simeq 0.2 \text{ order}$$

If one assumes a plate separation of 3mm (3×10^7 Å), wavelength λ_o of 5016Å, and a focal length f = 3.5 in., the radius of the pinhole is

$$\rho_p \simeq 3.5 \text{ in.} \left(\frac{2 \times 5016 \times 0.2}{3 \times 10^7}\right)^{\frac{1}{2}}$$

$$\rho_p \simeq .020 \text{ in.}$$

In the following section, the broadening effects on the transmitted peaks introduced by the pinhole of 0.040-in. diam. will be examined. It will be shown that these broadening effects, although increasing the uncertainty in determining the least count of the wavelength scale, will nevertheless be small enough to provide a sufficiently accurate scale to calibrate the strainmeter to 1 percent.

C. Sources of Uncertainties in the Fabry-Perot Interferometer

In the ideal theory it is shown by eq. 13 that the fringe transmitted through the instrument will be broadened as the reflectivity decreases. However when evaluating the performance of the actual instrument, one must also consider additional line broadening effects not predicted by the ideal theory:

(1) The Fabry-Perot plates are not perfectly plane and flat,

(2) The plates are not perfectly parallel,

(3) The plates assumed to be of infinite extent in theory are of finite area in practice,

(4) Introduction of a pinhole, although eliminating the effects of (3), contributes its own broadening effect,

(5) Lines emitted by the source are not monochromatic.

One may treat these effects in the manner of Chabbal, (1958) who introduces "Disturbance Functions" $D(\sigma)$ and $F(\sigma)$ to describe the loss of resolution and transmitted luminosity of the Fabry-Perot interferometer. $D(\sigma)$, the Surface Defect Function, describes the effects on the transmitted pattern when the plates are not perfectly smooth, plane, and parallel. The Pinhole Function $F(\sigma)$ describes the broadening in the transmitted line when the pinhole intercepts radiation transmitted over a finite range of ϕ. In addition, due to the use of finite sized plates, a deflection loss will occur as one moves out from the central order across the plates (Sluis, 1956). One observes that vignetting of the plate images worsens for larger angles of incidence and is zero at $\phi = 0$. The broadening effects of this function will therefore be negligible and will not be considered further.

In a similar fashion one introduces the Disturbance Function, $S(\sigma)$, to describe the fringe broadening contributed by the source. Since the order change is larger than the

wavelength variation is used to describe a displacement of one of the plates, the Disturbance Functions will be expressed in terms of the parameter m rather than σ. One thus has

S(m) - Source Function

D(m) - Surface Defect Function

F(m) - Pinhole Function

In order to analyze the effects of these broadening disturbances upon the Airy Function A(m) defined by eq. 6, one uses linear filter theory. In this mathematical system one approximates the interaction between the Disturbance Functions and A(m) by supposing that the resulting output is a superposition of component outputs produced by corresponding input disturbances. This resultant output, called the Instrumental Function W(m), is calculated by using the process of convolution where

$$W(m) = A(m) * D(m) * F(m) * S(m) \tag{22a}$$

and

$$A(m) * D(m) = \int_{-\infty}^{\infty} A(u) S(u-m)\, du \tag{22b}$$

similarly

$$A(m) * D(m) * F(m) = \int_{-\infty}^{\infty} \int_{-\infty}^{\infty} A(u) D(M-u) F(m-M)\, du\, dM \tag{22c}$$

Equation 22a is integrated to determine W(m). However such a calculation may become laborious. An alternative

method is to utilize digital data processing techniques that have been developed in the petroleum industry to solve such problems. A standard computer program written by Mr. Russell Gray was used to determine the resulting broadening effects on the Airy Function. The results are described in the following sections.

c-1. The Surface Defect Functions and Their Convolution With the Airy Function

In this section line broadening due to any deviation of the plates from perfect flatness and parallelism is investigated; otherwise it is assumed that the interferometer functions perfectly. To describe these effects Chabbal (1958) allows one plate to be perfectly plane while the second plate carries the surface defects (see fig. 8). Letting any point on the imperfect plate lie at a distance h from the perfect plate, Chabbal then introduces the function

$$D(h)\,dh = dS \tag{23}$$

where D(h) describes the influence of the surface defects upon transmission of radiation of σ_o through the plates. When dS, which represents the surface area on the imperfect plate lying between thicknesses of h + dh/2 and h - dh/2, transmits σ_o so that $2h(\cos\phi)\sigma_o$ = integer, D(h) will have a

maximum value. When no radiation is transmitted, D(h) will have a minimum value.

Assuming h_o is the thickness corresponding to maximum D(h), Chabbal then defines the increment $x = h-h_o$ so that eq. 23 now becomes

(24) $D(x)dx = dS$

Equation 24 is significant because it serves to describe completely the surface defects of the plates. When the plates move a distance x, the limits of the incremental area dS are defined to lie in a range of dx, which is the incremental component of the motion of the plates normal to the perfect plate. The intensity distribution over the entire area of the plates may then be charted to describe pictorially the surface irregularities as discussed by Chabbal. For the purposes of this paper, it will suffice to consider only how the summation of these incremental areas dS transmitting radiation σ_o changes with the scan. For example, if the plates were perfect, such a scan would produce lines of zero width, as depicted in fig. 8.

To describe these surface defects, Chabbal assumes that one may approximate their effects as the superposition of three functions. These are introduced as periodic variations in the surface contour. In descending order of period one has

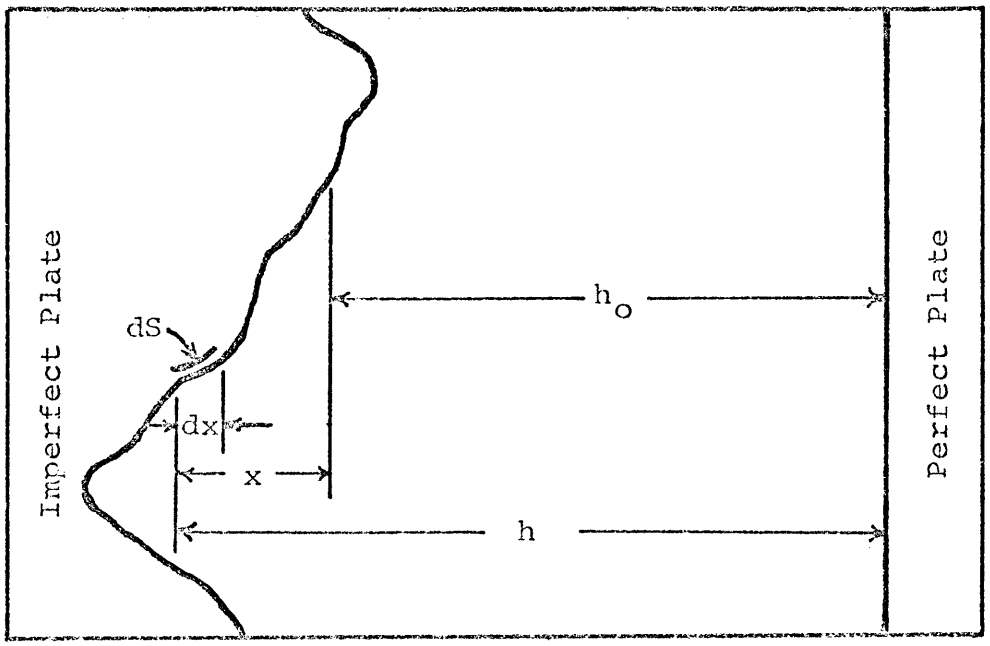

Figure 8. Irregular Spacing Between the Fabry-Perot Plates Due to the Surface Defects.

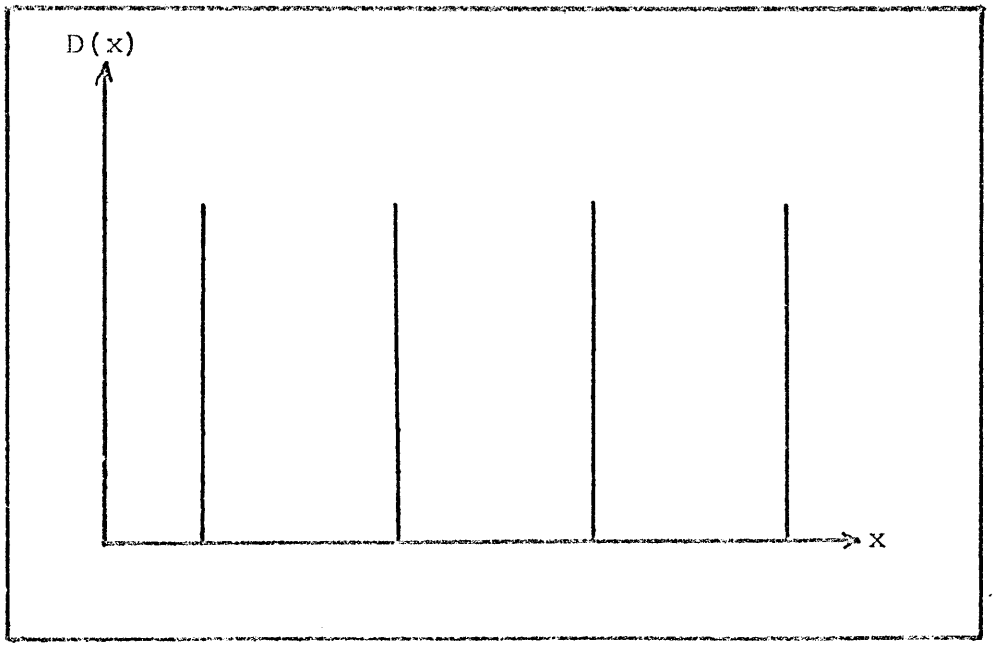

Figure 9. The Form of the Transmitted Fringes when the Interferometer is Perfect.

(1) Parallelism Function - $D_p(x)$ - A small angle α describes the deviation of the plates from parallelism. If c is the horizontal deviation when the imperfect plate makes an angle α with the perfect plate then

$$(25a) \quad D_p(x) = \frac{4S}{\pi c}\left(1 - \frac{3x^2}{b^2}\right)^{\frac{1}{2}} \quad \text{for } -\frac{c}{2} \leq x \leq \frac{c}{2}$$

where $b = \frac{3^{\frac{1}{2}}}{2} c$. $D_p(x)$ is sketched in Fig. 10a.

(2) Sphericity Function - $D_s(x)$ - The surface is spherical with maximum deflections, a, where

$$(25b) \quad D_s(x) = \frac{S}{a} \text{ (a constant) for } 0 \leq x \leq a$$

$$D_s(x) = 0 \quad \text{for } x < 0,\ x > a$$

where S is the total area of the plates. $D_s(x)$ is sketched in Fig. 10b.

(3) Roughness Function - $D_g(x)$ - The surface roughness is assumed to be a Gaussian distribution where

$$(25c) \quad D_g(x) = \frac{2S}{b}(\mathrm{Ln}2)^{\frac{1}{2}} \varepsilon^{-4\mathrm{Ln}2\left(\frac{x}{b}\right)^2}$$

$D_g(x)$ is sketched in fig. 10c.

Since an order change occurs as a result of irregularities in the plate spacing, one has by eq. 11

$$(26) \quad \Delta m = \frac{2\Delta h}{\lambda_o}$$

The functions in eq. 25 are expressed in the more convenient parameter, m

$$(a) \quad D_p(m) = \left\{1 - \frac{3(\Delta m)^2}{b^2}\right\}^{\frac{1}{2}} \quad \text{for } -\frac{c}{2} \leq x \leq \frac{c}{2}$$

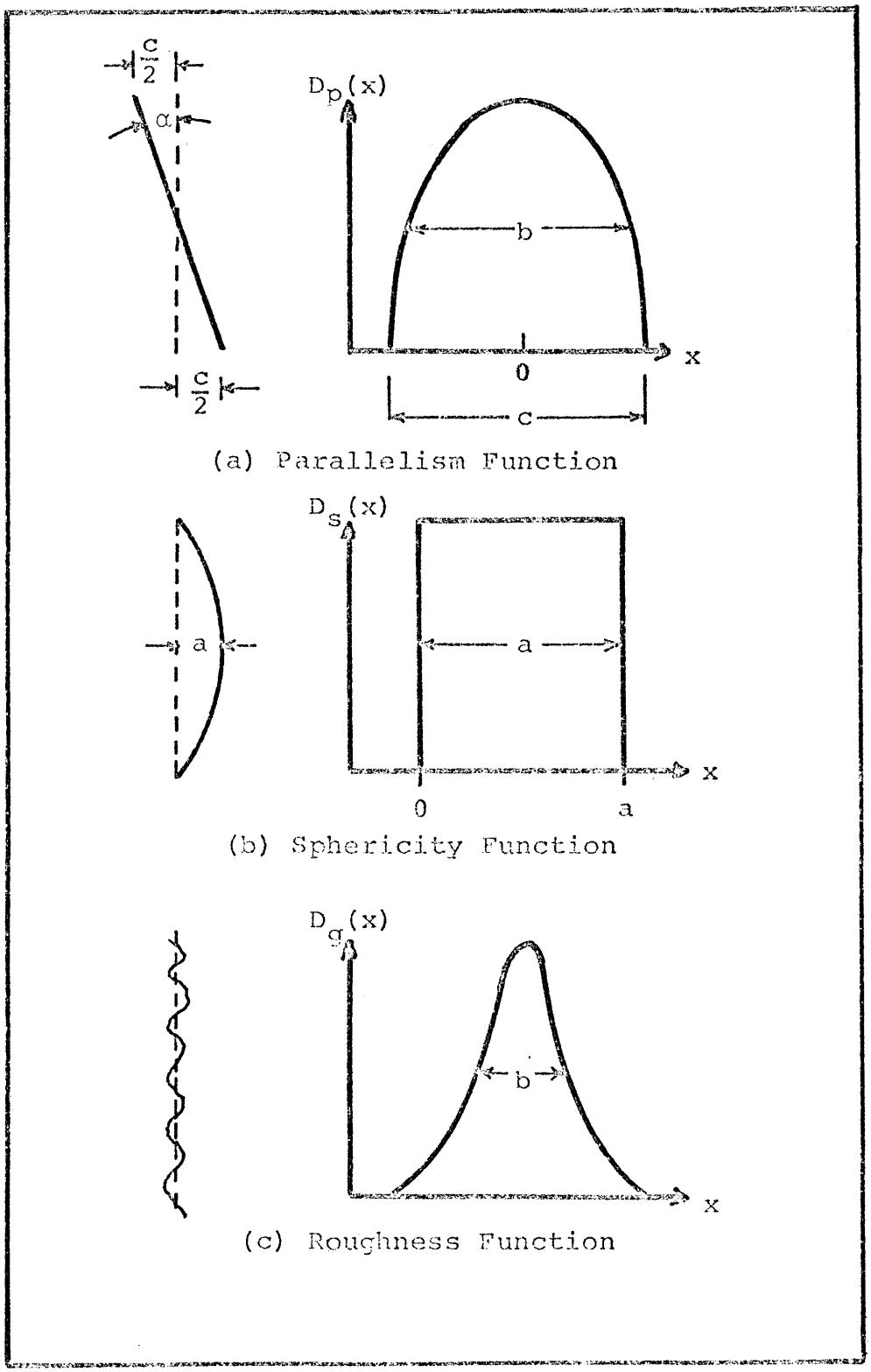

Figure 10. The Intensity Contours of the Surface Defect Functions.

$$
\begin{aligned}
&(b) \quad D_s(x) = 1 \quad \text{for } 0 \leq x \leq a \\
&\qquad D_s(x) = 0 \quad \text{for } x < 0,\ x < a \\
&(c) \quad D_g(m) = \varepsilon^{-4 \ln 2 \left(\frac{\Delta m}{b}\right)^2}
\end{aligned}
\tag{27}
$$

where the functions in eq. 27 are the normalized forms of eq. 25.

Today optical flats are commercially available at reasonable prices with specifications on flatness to $\lambda/50$ of the green line of Hg (5470 $\mathring{A}$). If one assumes a maximum deflection for sphericity, a, and a horizontal deviation, c, each with a magnitude of $\lambda/50$ and a half width for the Roughness Function of $\lambda/100$, the corresponding half width in fractions of an order number of each Surface Defect Function can be calculated by using eq. 26. However for the function $D_p(m)$ a half width $b = .02\lambda$ is used instead of $b = .0173\lambda$ so that the half width $D_p(m)$ in units of order number has been overestimated. One thus has

For $D_p(m)$ $b = 0.044$ order

For $D_s(m)$ $b = 0.044$ order

For $D_g(m)$ $b = 0.022$ order

Each of the above Surface Defect Functions are convolved with the Airy Function of half width 0.071 order and peak width 0.011 order, and the broadening of the resulting convolution is illustrated in figs. 11, 12, and 13, and compared to the corresponding broadening of the Airy Function.

The widths measured from these figures are

For $D_p(m)*A(m)$ b = 0.080 order p = 0.013 order

For $D_s(m)*A(m)$ b = 0.084 order p = 0.015 order

For $D_g(m)*A(m)$ b = 0.080 order p = 0.011 order

c-2. The Pinhole Function and Its Convolution With the Airy Function

Line broadening due to the pinhole is next investigated. The extreme case of such broadening is first considered. Imagine a pinhole sufficiently wide to transmit a large range of ϕ so that, as one of the plates moves, intensity of a ring of integral order will be transmitted at every instant. The photocell will detect a constant intensity at all times and continuously record a straight line (see sec. c-3 and fig. 7).

If one now contracts the pinhole to the diameter (e.g. the diameter calculated in sec. b-4) where the range of ϕ covered by the pinhole is such that a ring of integral order will not be transmitted, peak intensity will be reduced. Consequently the broadening function that is formed will be rectangular, and its width will be related to the pinhole diameter as shown below (see also Fig. 14).

To determine the corresponding order change due only to the pinhole diameter (the interferometer is otherwise assumed ideal), one has at $\phi = 0$

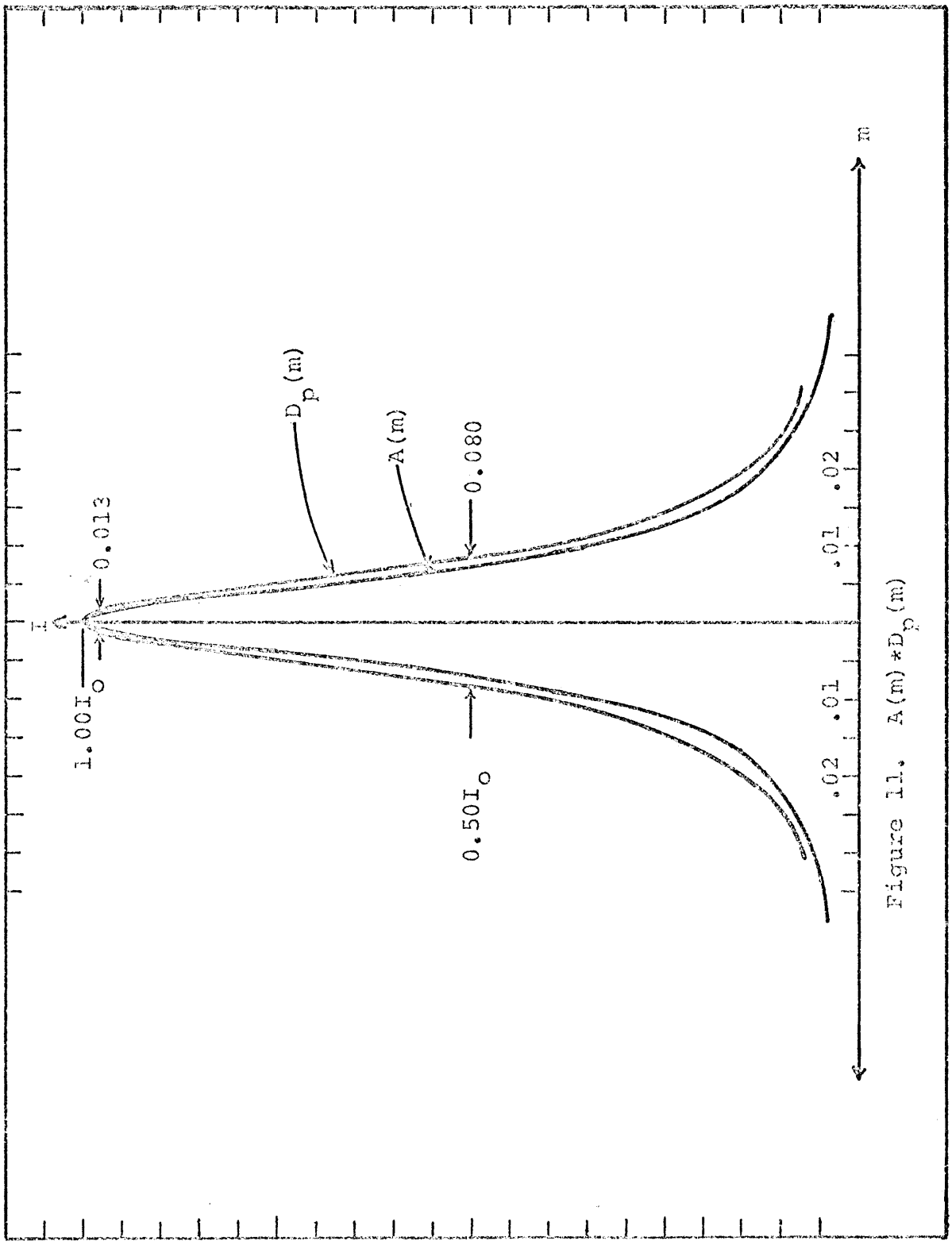

Figure 11.

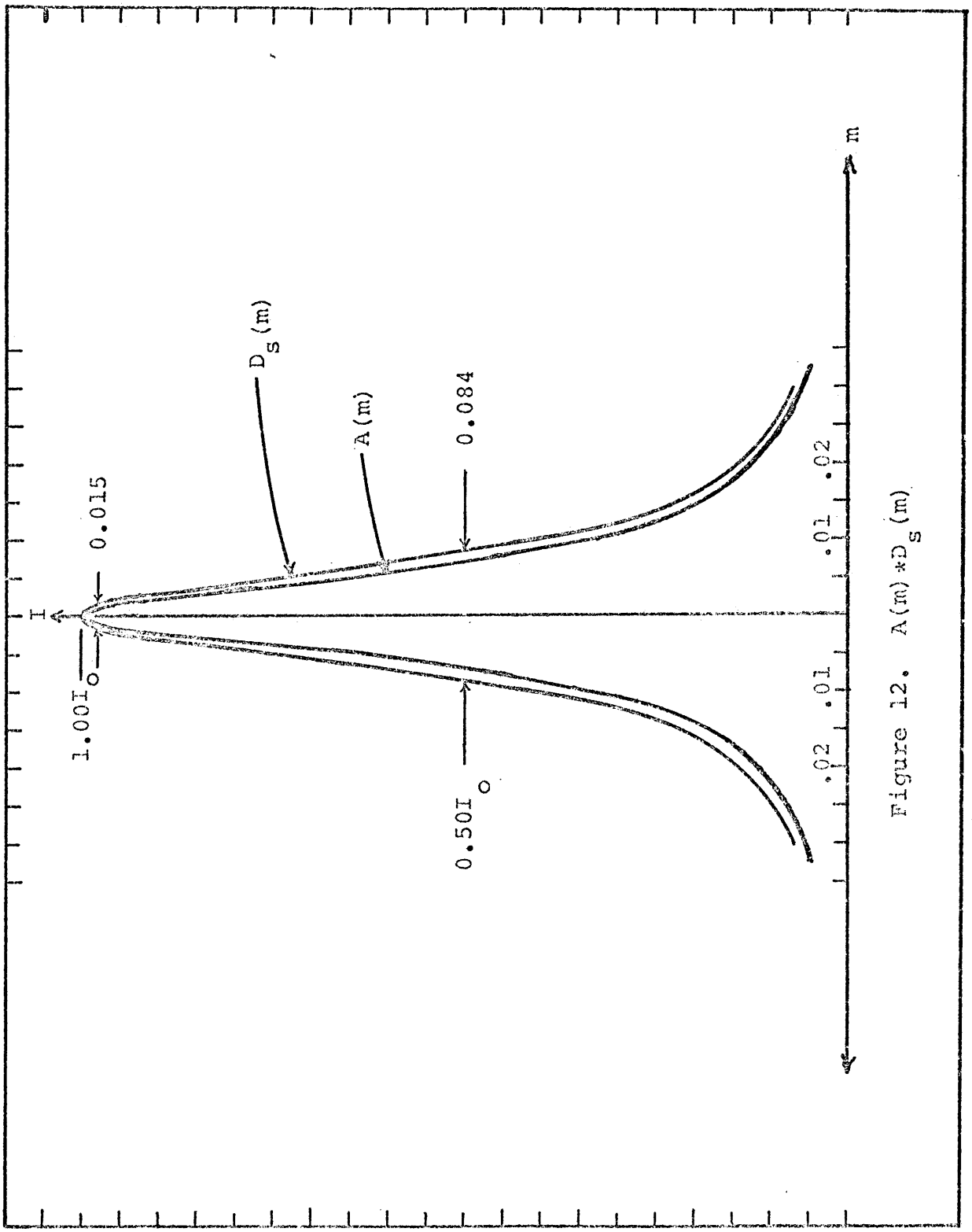

Figure 12.

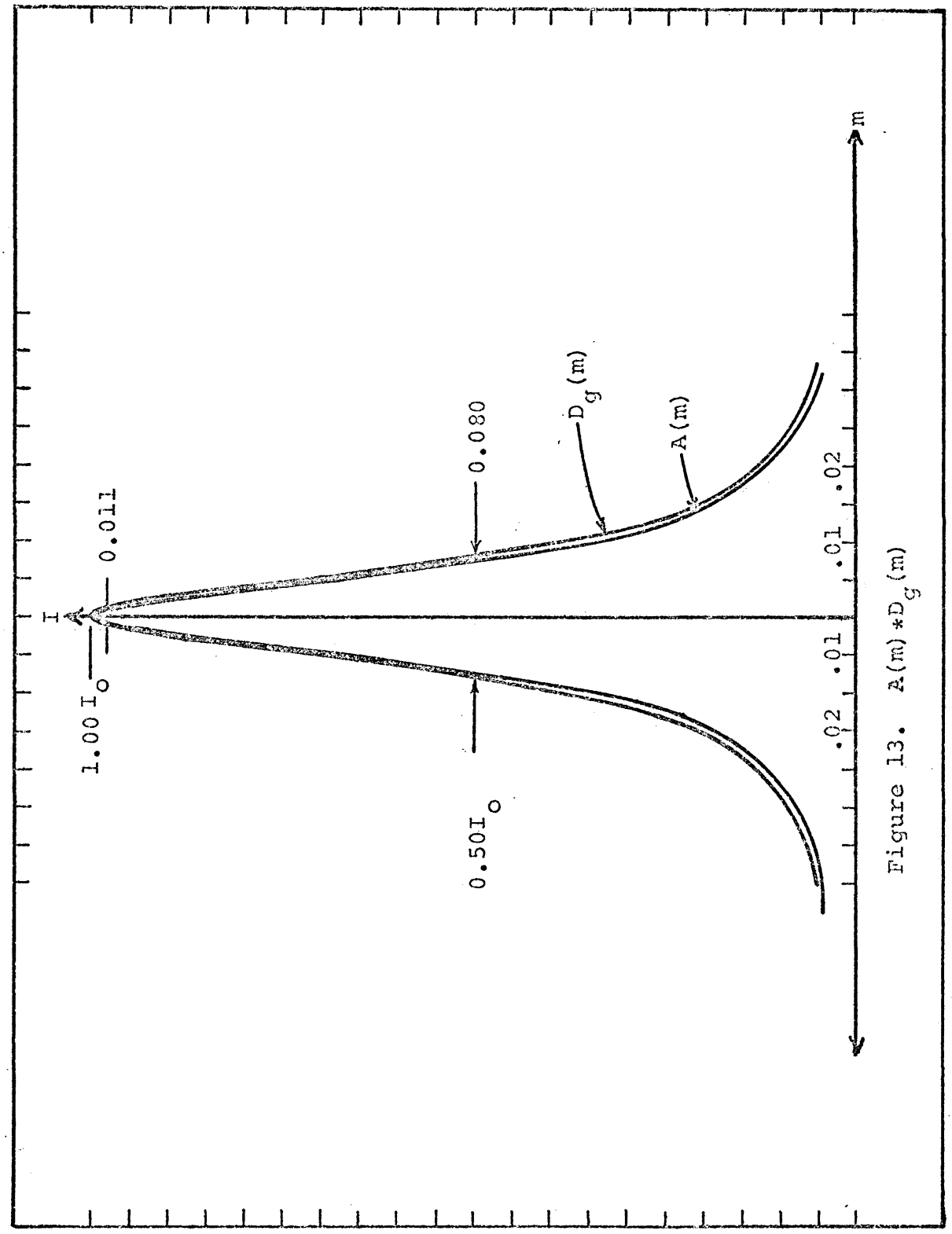

Figure 13. A(m)*D_g(m)

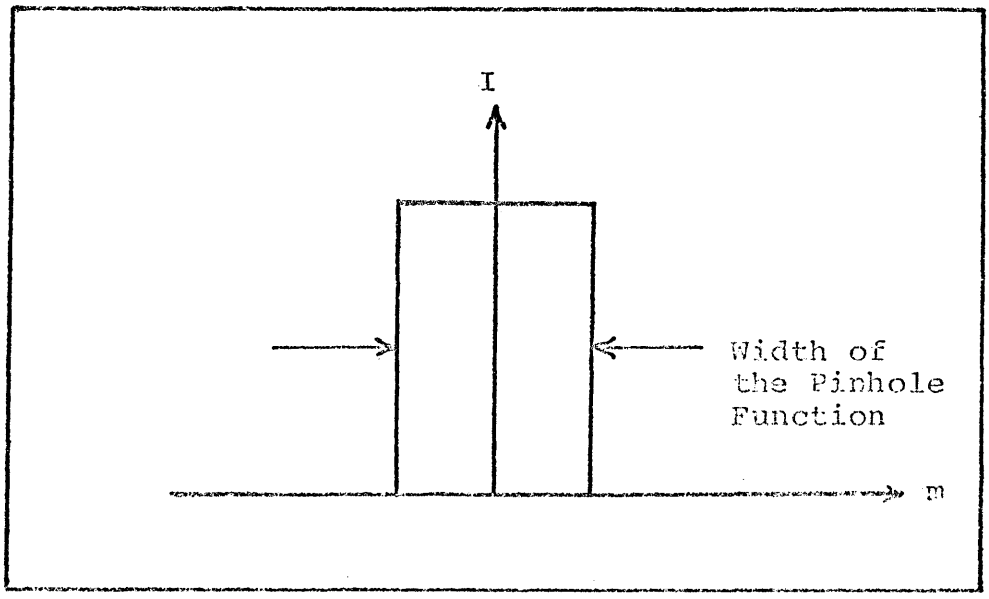

Figure 14. The Intensity Contour of the Pinhole Function.

$$m = 2h\sigma_o$$

and at the outer rim where the pinhole radius corresponds to an angle change $\Delta\phi$

$$m-\Delta m \simeq 2h\sigma_o(1-\Delta\phi^2/2)$$

so that Δm becomes

(28a) $$\Delta m \simeq h\Delta\phi^2/\lambda_o$$

and the pinhole radius is

(28b) $$\rho_p = f(\Delta m\lambda_o/h)^{\frac{1}{2}}$$

Again assuming h = 3 mm, λ_o = 5016 $\mathring{A}$, ρ_p = 0.020 in. and f = 3.5 in., one may calculate Δm to be 0.2 order which is much larger than the Airy half width. It is desirable to reduce half width to 0.1 order by decreasing the plate separation h to 1½ mm. Then by use of the normalized Pinhole Function having a half width of 0.1 order, the resulting convolution illustrated in Fig. 15 yields a half width and peak width of 0.120 order and .020 order respectively.

c-3. The Source Function S(m) and Its Convolution With A(m)

Monochromatic light is an idealization and is not found to exist in nature. Much of the wavelength spread found to exist in "monochromatic" lines is due to several broadening processes. These include natural broadening, Doppler broadening, pressure broadening, and broadening due to self absorption.

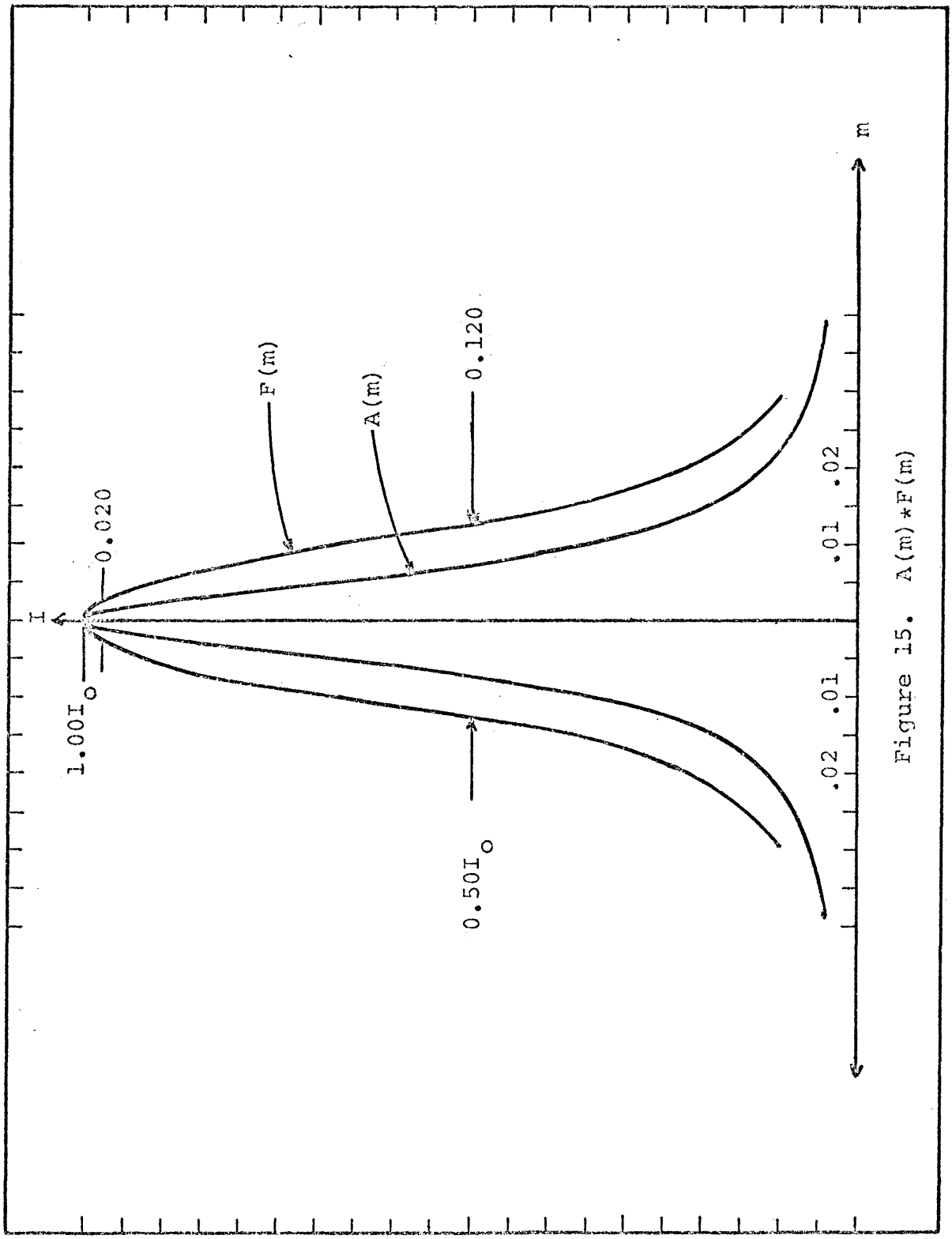

Figure 15. A(m)*F(m)

Broadening of monochromatic lines due to high pressure is difficult to calculate (oral communication with J. Cooper, Joint Inst. for Lab. Astrophysics, Boulder, Colorado, 1967). But informed opinion (oral communication with J. Cooper, J. V. Kline, CSM, 1967; and written communication with H. P. Larson, Purdue University, 1967) is that pressure broadening is small at 7 torr (1 torr = 1 mm Hg), the pressure of the source at room temperature (written communication from A. D. MacKay Co., New York City, 1967). This assumption will be shown to be justified when the half width measured from the recording compared favorably with the half width of the instrumental function (see ch. V, secs. A and C).

Natural width occurs because atoms emit wave trains in pulses degrading the monochromaticity of the line. As a rule the Doppler width is much larger and easily masks the natural width. Natural widths in frequency units are published by the Natural Bureau of Standards (Wiese and others, 1966). The natural half width in $\overset{o}{A}$ can be calculated from the expression

$$\Delta\lambda = -\frac{\lambda_o^2}{c}\Delta\nu$$

where $\Delta\nu$ is the half width in frequency units. Substituting in the appropriate values $\lambda_o = 5016\ \overset{o}{A}$, $c = 3 \times 10^{10}$ cm/sec, and $\Delta\nu = 1.3 \times 10^{7}$ Hz., the natural half width becomes

$$\Delta\lambda = 1 \times 10^{-12}\ \text{cm} = 1 \times 10^{-4}\ \overset{o}{A}$$

The Doppler effect results from the motion of atoms towards and away from the observer due to thermal agitation. If radiation of frequency ν_o is emitted by these atoms, it will be perceived by the observer as a radiation of frequency $\nu_o \pm \Delta\nu$. It is thus seen that the Doppler effect will be greater at higher temperatures and lower molecular masses. Candler (1951, p. 16-19) shows that the intensity distribution due to the Doppler effect is Gaussian in λ where

$$(29a) \quad I = I_o \, \varepsilon^{\frac{-mc^2}{2kT}\left(\frac{\lambda-\lambda_o}{\lambda_o}\right)^2}$$

and if b is the half width in $\mathring{A}$

$$(29b) \quad b = 2\lambda_o(2kIn2/M_Hc^2)^{\frac{1}{2}}(T/M)^{\frac{1}{2}}$$

k = Boltzmann Constant
= 1.372×10^{-16} ergs/^oK

c = the velocity of light
= 2.998×10^{10} cm/sec

m = MM_H - Mass of the molecule in g

M = the atomic mass of the gas in amu

M_H = Mass of the hydrogen atom in $\frac{g}{amu}$
= 1.668×10^{-24} g/amu

T = Temperature of the emitting gas in ^oK

Equation 29b becomes upon substitution of the above numerical values

$$(29c) \quad b = 7.14\lambda_o(T/M)^{\frac{1}{2}} \times 10^{-7}\mathring{A}$$

Equation 29a may be re-expressed in terms of fractions of an order number Δm and the half width b

$$(29d) \quad I = I_o \, \varepsilon^{4 \ln 2 (\frac{\Delta m}{b})^2}$$

The difficulty involved in calculating the Doppler half width is in obtaining the temperature of the emitting gases at the source. Temperatures in Geissler tubes may range as high as 2000°C but it has been suggested (Cooper, oral communication, 1967; Larson, written communication, 1967) that a temperature of about 300°C be used in this calculation.

If a helium discharge tube is operated at seven torr and a temperature of 300°C, then the Doppler half width is

$$b = 7.14 \times 10^{-7} \times 5016 \times (600/4)^{\frac{1}{2}} \text{ Å}$$

$$b \approx 0.05 \text{ Å}$$

To determine the half width in fractions of an order number, one has from eq. 11

$$(30) \quad \Delta m_h = 2b \times h/\lambda^2 < 0.07 \text{ order}$$

where Δm_h is the Doppler half width in order number.

Self absorption occurs because the emitting gases will appreciably reabsorb their energy emissions at resonance frequencies. It is found that broadening increases with the length of the emitting gas column. For example, Kline (1952) shows that self-absorption broadening of various lines in

the infra-red range of the helium spectrum becomes appreciable when the helium-discharge lamp is observed "end on" (the line of sight is along the axis of the discharge tube). However the broadening appears small when the lamp is observed with a line of sight that is normal to its axis. Tentatively based on this observation the self-absorption width will be assumed to be small so that the broadening at the source will be characterized only by the Doppler width.

The normalized Airy Function and Source Function which uses b = 0.07 order are convolved and the results are summarized in the graph of Fig. 16. It shows that the resulting contour has a half width of 0.120 order. The peak width is increased from 0.011 order to about 0.02 order.

c-4. Conclusions

In this last section the total loss of accuracy resulting from peak broadening will be considered. In addition it will be shown how the Fabry-Perot interferometer might be used to produce displacements to the desired accuracy.

The peak widths of the broadened functions determined in the above sections indicate that the Source and Pinhole Functions contribute the largest part of the broadening at the peak. Each of these functions approximately doubles the Airy peak width, whereas the Surface Defect Functions widen

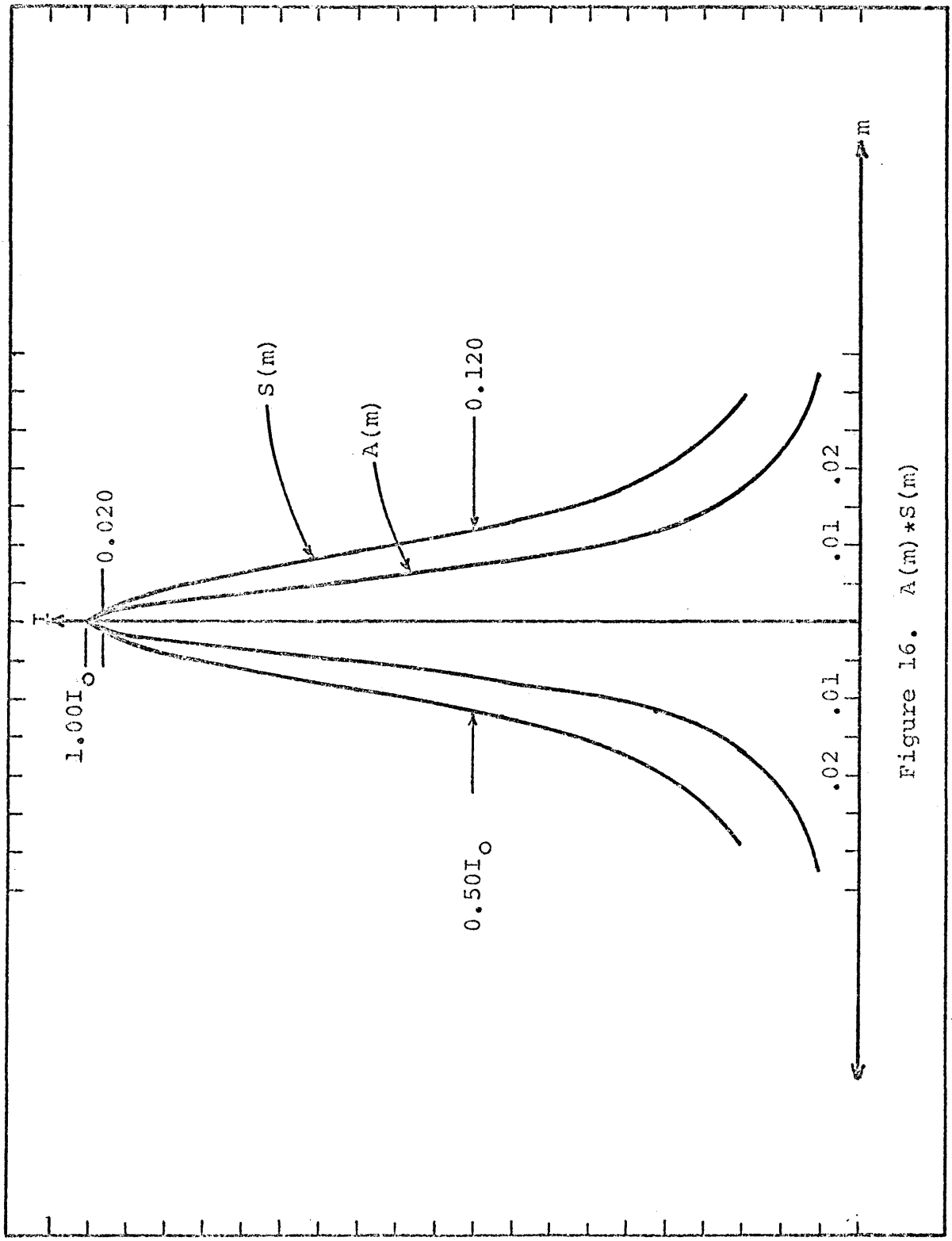

Figure 16. A(m)*S(m)

the peak by about a factor of one half. It is thus instructive to estimate the broadening resulting when the functions A(m)*F(m) and S(m) are convolved. The outcome of this operation is displayed in Fig. 17, where the half width is 0.150 order, but surprisingly the peak width remains about the same as that of A(m)*F(m) at 0.025 order. Finally the resulting Instrumental Function W(m) illustrated in Fig. 18 shows that the half width and the peak width have values of 0.160 order and 0.025 order respectively. Indeed it is observed that the contours of W(m) and A(m)*S(m)*F(m) are almost the same.

The conclusion to be drawn is clear. The Doppler and Pinhole effects constitute the main sources of peak broadening. In order to improve the accuracy of the wavelength scale, this broadening must be reduced. Although the Doppler effect at the light source is difficult to eliminate, the Pinhole Function may be reduced by decreasing the thickness of the gap h between the flats and by using a smaller pinhole. For example the pinhole half width may be reduced by a factor of 10 (b = 0.01 order) by using a plate separation of ½ mm (1/2 x 10^7 Å). Then by eq. 28b the pinhole radius may be calculated to be

$$\rho_p = 3.5 \text{ in. } \left\{\frac{5016}{0.5 \times 10^7} \times 0.01\right\}^{\frac{1}{2}}$$

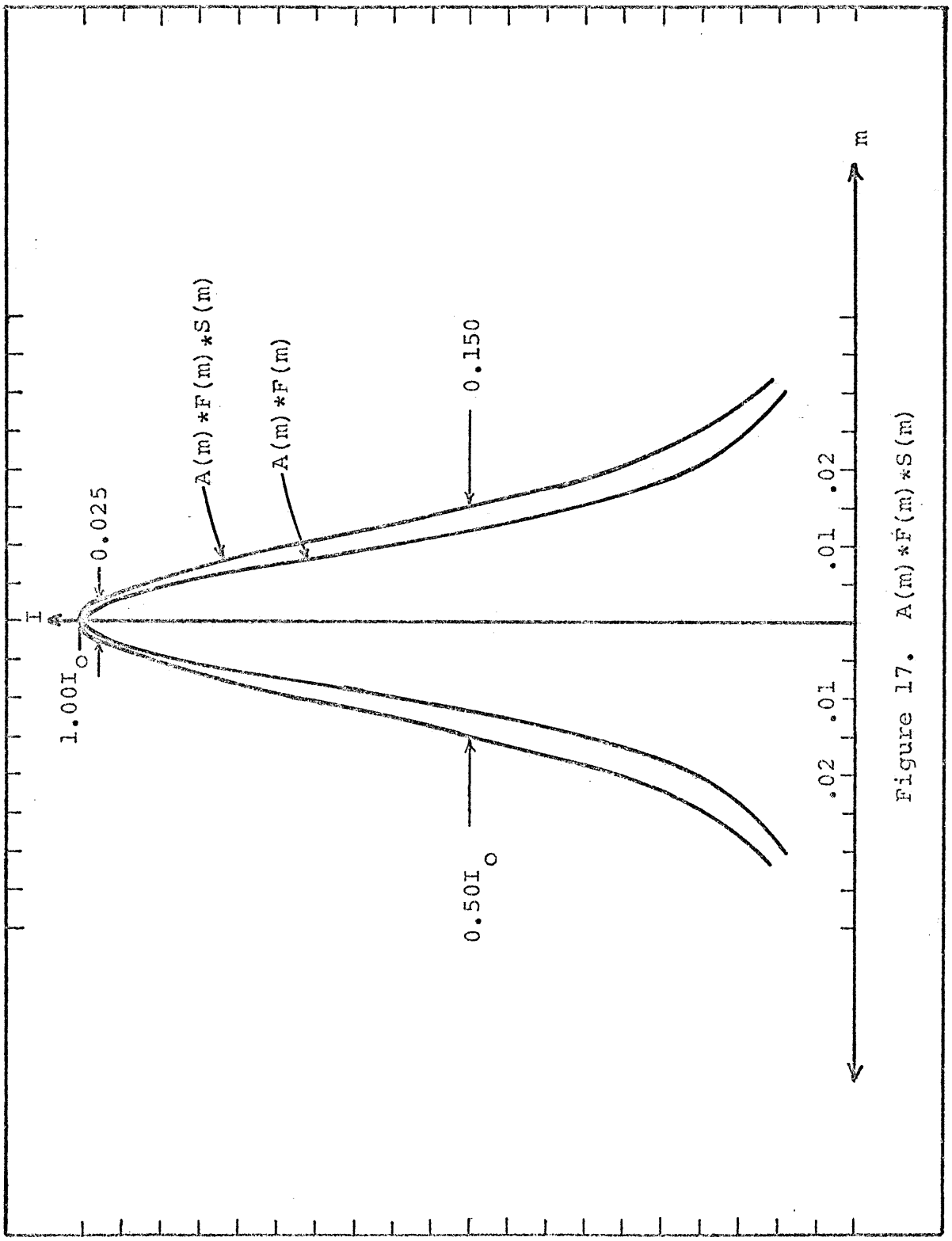

Figure 17. A(m)*F(m)*S(m)

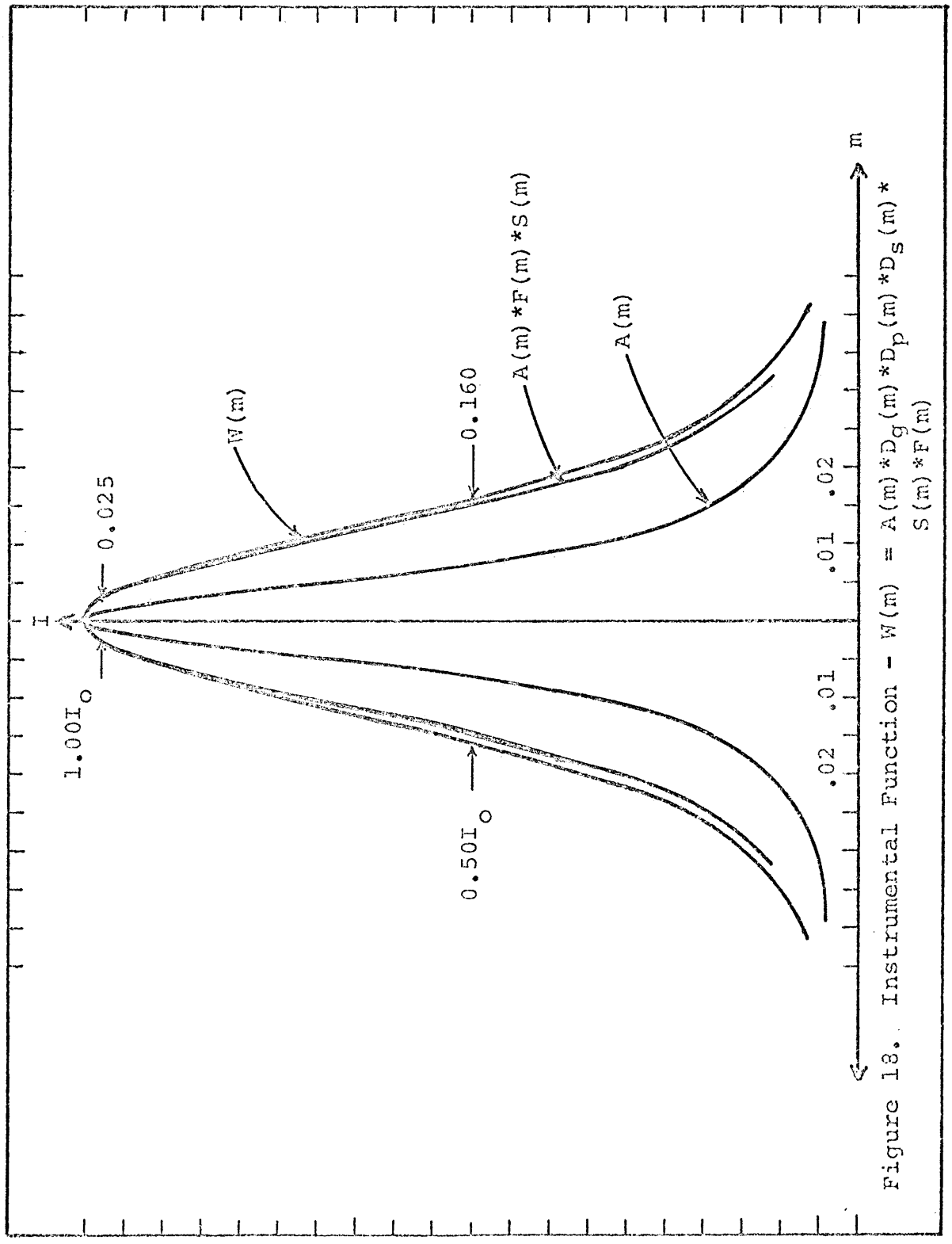

Figure 18. Instrumental Function - W(m) = A(m)*D_g(m)*D_p(m)*D_s(m)*S(m)*F(m)

$\rho_p = 0.011$ in.

In decreasing the spacing of the plates to 1/2 mm, the interferometer would also be made somewhat less sensitive to the Doppler effect for by eq. 30

$\Delta m_h = 0.024$ order

which is of the same size as the half width of the Roughness Function; and since the latter is Gaussian as well as the Source Function, the broadening effect on both peak widths is about the same.

If the pinhole diameter of 0.040 in. and interplate spacing of 1½ mm is retained, then according to Fig. 18 the Instrumental Function peak width of 0.025 order will yield a 2.5-percent error per wavelength scale division. However, if one allows one of the plates to scan at least three orders, the desired 1-percent measurement with the wavelength scale will be achieved, and a scan of 10 to 15 orders will further reduce the uncertainty.

If the suggested pinhole diameter of 0.022 in. and plate spacing of 1/2 mm is used, the broadening effects of the Source and Pinhole will be diminished to such an extent that the Airy peak width will now dominate the peak broadening. If further improvement in the accuracy is desired, higher reflection coefficients provided by dielectric films may be used to reduce the Airy peak width so that only the

Surface Defect Functions will be the limiting factors.

In the above discussion it has been assumed that the parallelism between the plates can be kept to within the flatness tolerance of the plates. The problem of parallelism becomes especially acute if the plates are moved. In the following chapters this problem will be examined, and the loss of accuracy due to degrading of parallel motion when one of the plates is moved will be calculated.

III. INSTRUMENT DESIGN

The optical system to be used with the interferometer should transmit all available intensity from the filtered light source to the photocell and select only those rays incident normally on the Fabry-Perot plates.

The optical system has two pinholes and three convex lenses, two of which are of equal focal length. The arrangement of these optical elements are shown in fig. 19. The first lens L_1 having the odd focal length focuses an image of the extended source onto the first pinhole, which is centered on the optical axis and lies at the focal point of lens L_2. When the Fabry-Perot plates are adjusted perpendicular to the optical axis, the light rays will be incident normally on the plates. Lens L_3 focuses the light rays emerging from the plates, onto a point on the optical axis where the second pinhole has been placed. The photocell positioned behind this pinhole receives the light passing through the pinhole. The second pinhole is needed because

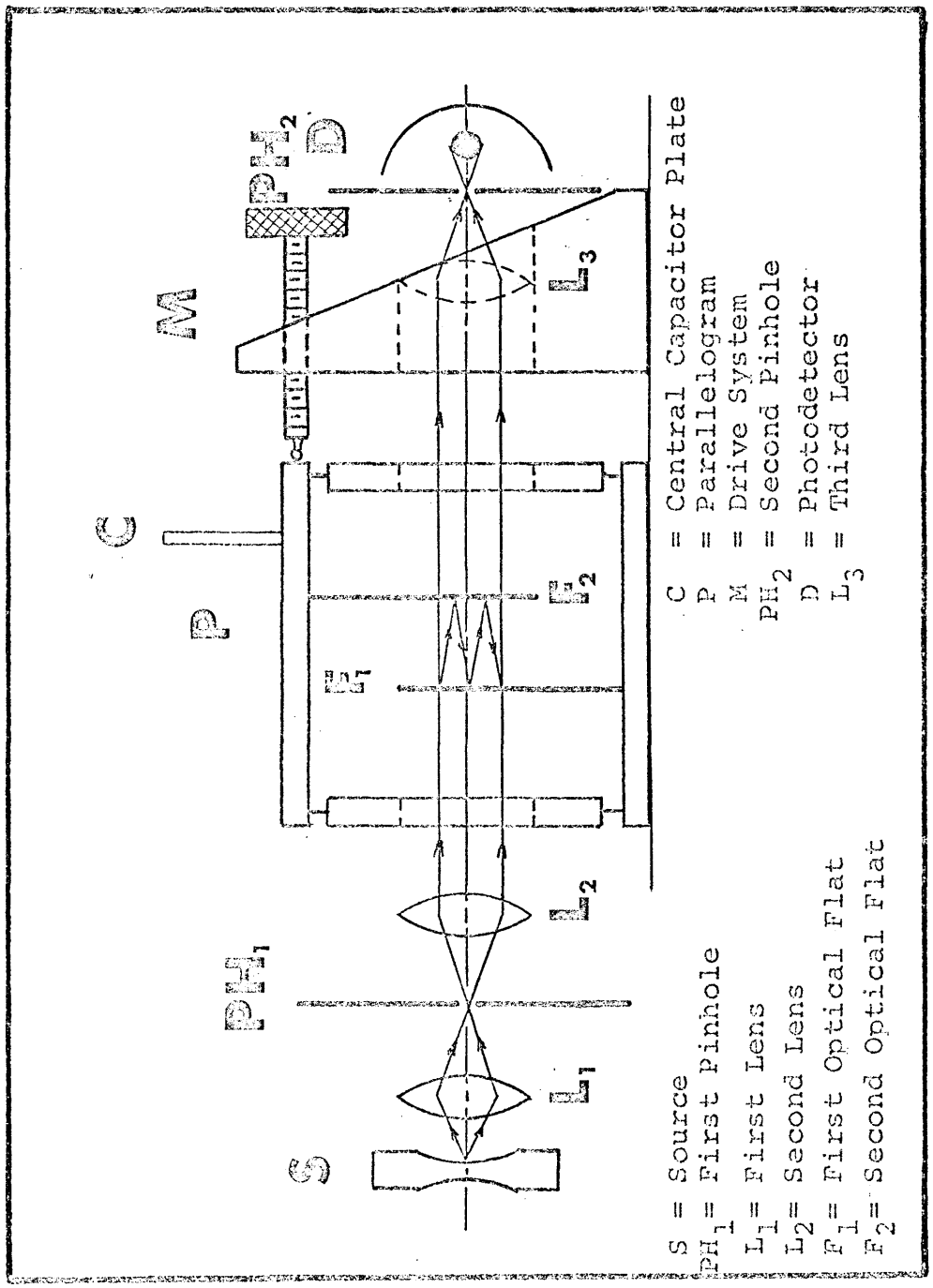

Figure 19. A Schematic Drawing Showing the Construction of the Variable Spacing Fabry-Perot Interferometer.

it prevents transmission of scattered light that would otherwise increase the "background" between the peaks, and possibly produce spurious peaks.

In the mechanical construction of the interferometer a driving system must be designed that will move one of the Fabry-Perot plates parallel to the other with a motion that is both slow and smooth. Measurement of displacement requires that only one interferometer plate be moved while the other is held fixed as shown in fig. 19.

The strainmeter transducer has already been described in ch. I. Therefore only those features of the transducer that contribute to the design of the interferometer as a calibrating device will be considered here.

The sensing element of the transducer consists of two parallel capacitor plates between which is placed a single capacitor plate of the strainmeter (see fig. 20a). The capacitors C6 and C7 formed by the plates of the transducer and the strainmeter are variable and are each part of an L-C resonating circuit that is driven by a 1.5 Mc. oscillator. Any movement of the central plate will change the resonating frequency of both tank circuits and produce a change in the rectified voltage output that can be related directly to this movement.

Both the optical flat and the central capacitor plate

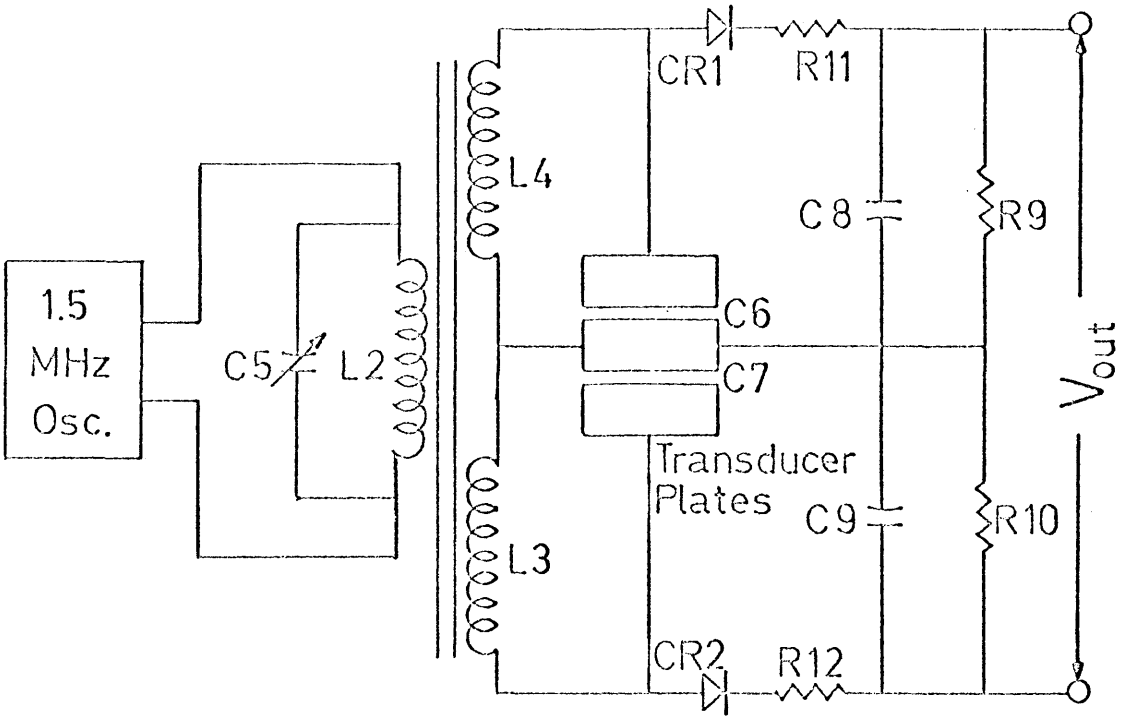

DISCRIMINATOR CIRCUIT

Figure 20a

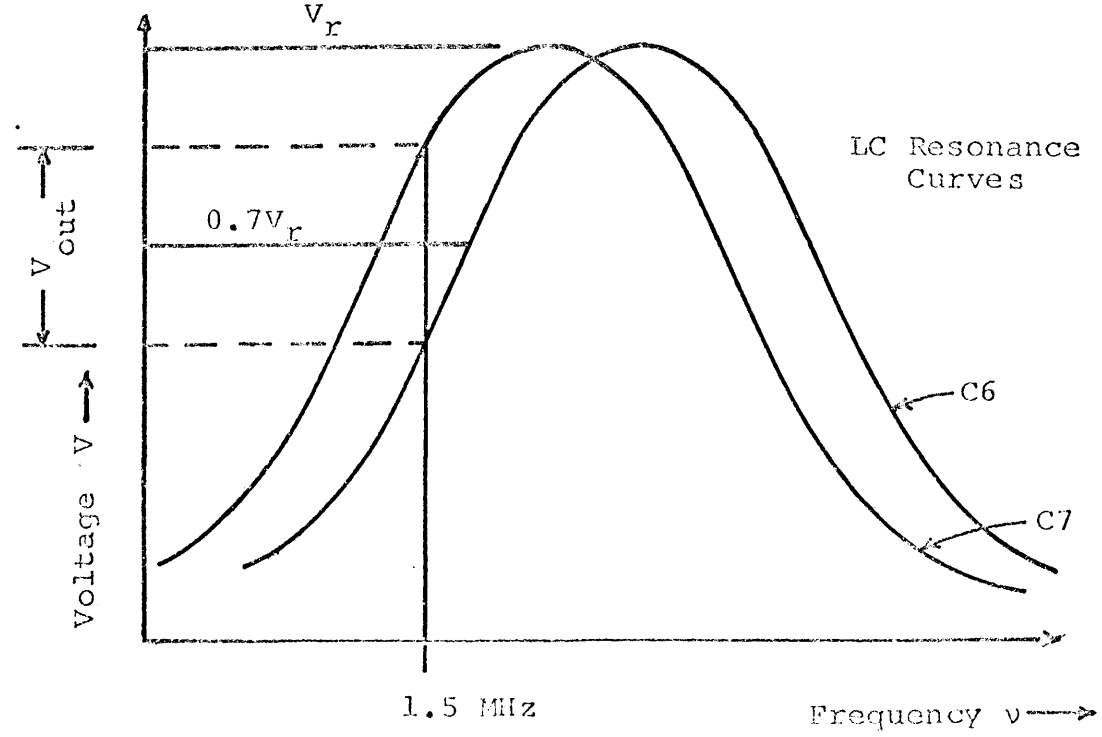

PRINCIPLE OF OPERATION OF DISCRIMINATOR

Figure 20b

are mounted on the moving element of the parallelogram as shown in fig. 19 and described in more detail in sec. C of this chapter. Both transducer and interferometer record simultaneously any movement of this element. Comparison of the two records will yield the scale factor of the transducer.

A. Basic Problems in the Instrument Design

The above description of the ideal form of the instrument stressed the functions to be performed by it without regard to error occurring while in performance of these functions. Below is outlined a number of limiting factors that must be considered in order to transform the ideally conceived instrument to a practical operating instrument.

(1) Material is not rigid and is therefore subject to strain, creep, warping, and vibration.

(2) Friction causes erratic motion when fine smooth motion is desired.

(3) Temperature changes cause expansion and contraction of the material.

(4) Fringes transmitted through the interferometer may be broadened by the following disturbing effects:

a) Surface defects in the geometry of the optical flats
b) "Monochromatic" light of finite bandwidth transmitted through the interferometer
c) Finite size of the pinhole
d) Nonparallelism of the optical flats

(5) Motion of the central capacitor plate may not be parallel to the motion of the Fabry-Perot plate along the optical axis.

(6) The refractive index of air is not exactly one, and it may vary due to fluctuations in atmospheric pressure and temperature.

(7) Light intensity may be reduced as it is transmitted through the optical system.

In the following sections a description of the construction of the calibration system is presented. In most cases the effects of the limiting factors cited above have been reduced through specific design features incorporated in the instrument.

B. The Optical System

A description of the optical system employed is presented below. This system is composed of two parts, the monochromatic light source and the interferometer. These are illustrated in fig. 21, a schematic diagram of the optical system.

The Light Source

The light source should emit a spectral line conforming to the specifications cited in ch. I. It should also be reasonably priced and readily available. The 5016 Å line has been chosen because of its use as a secondary standard (Terrien, 1960, p. 95-107). This line is sufficiently

THE OPTICAL SYSTEM

Fig. 21

(1) The light source (Geissler tube) and aluminum casing

(2) Housing unit to reduce stray light

(3) Convex lens - 44.5 mm focal length

(4) Plane mirror - 1 in. x 1 in.

(5) Pinhole #1

(6) Monochromatic filter

(7) Lens #2 - 93 mm focal length

(8) Two optical flats

(9) Lens #3 - 93 mm focal length

(10) Pinhole #2

(11) Photodetector

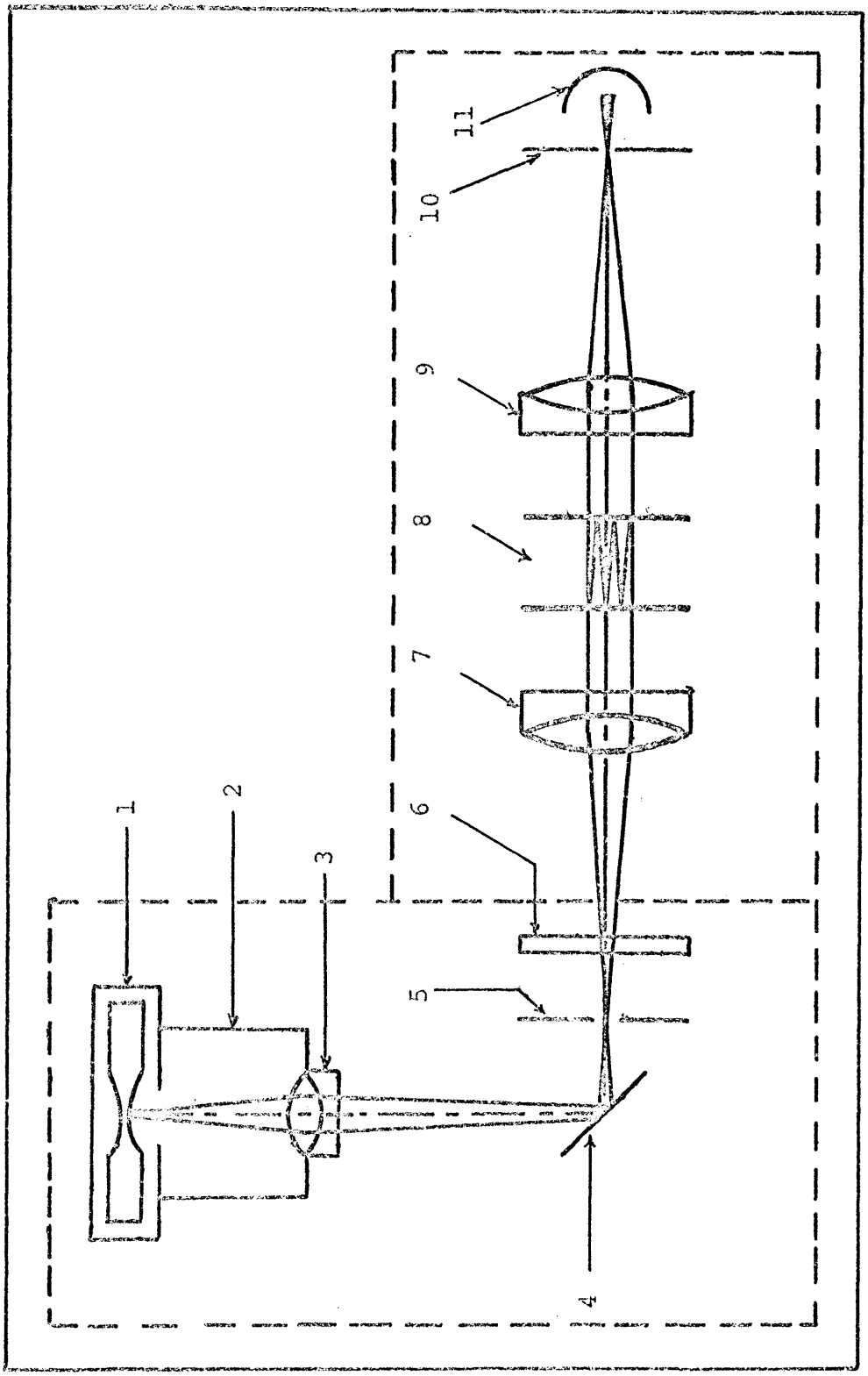
11
10
9
8
7
6
5
4
1
2
3

isolated from its nearest neighbors in the helium spectrum, and calculations show that the peak width due to the Doppler effect is sufficiently narrow to be used as a wavelength scale (see ch. II, sec. c-3). A. D. MacKay Co., New York City, manufactures helium discharge tubes that are reasonably priced.

The light source is encased in an aluminum tube whose inner walls have a mirror-like finish. The aluminum tube serves two optical purposes: it blocks off extraneous light from reaching the photocell and doubles the intensity when the light source is placed at the center of the tube so that the image of the light source is reflected onto the source itself.

Lenses

In general images formed by a lens will be deformed. Since the pinhole lies on the optical axis and the source is monochromatic, only spherical aberration of the pinhole image will be important. Reasonably priced lenses that are corrected for chromatic aberration (called achromats) are also approximately corrected for spherical aberration. Several achromats of about 1-in. diam were purchased from Edmond Scientific Co., Barrington, N. J. Convex lenses having focal lengths of 44.5 mm and 93 mm were used. The 44.5-mm lens was utilized in the light source unit while the two 93-mm

lenses were utilized in the interferometer.

The Filter

An interference filter of the Fabry-Perot type is being used to filter the 5016 Å line. A Bausch and Lomb filter was originally used but was found to transmit He lines at 5875 Å and 4470 Å at about $\frac{1}{10}$ the peak intensity of the 5016 Å line. Subsequently a custom-made filter was purchased from Spectrum Systems Inc., of Waltham, Mass., with the following specifications: The filter transmits a monochromatic line at 5016 Å at 45- to 55-percent peak transmission and a half width of 30 Å. Transmission of side bands are reduced to less than $\frac{1}{100}$ of peak transmission. The physical dimensions of the filter are 1 by 1 in. (see fig. 22).

The Fabry-Perot Plates

Two optical flats were purchased from Perkin Elmer Corp. of Norwalk, Conn. The specifications state that the two optical flats use an aluminum reflection film which permits 10-percent transmission of the 5016 Å line. The surfaces of the plates are flat to within $\lambda/50$ with an overcoat of SiO for protection from humidity. The flats are made from borosilicate glass with a 1-in. diam and 0.375 in. thickness.

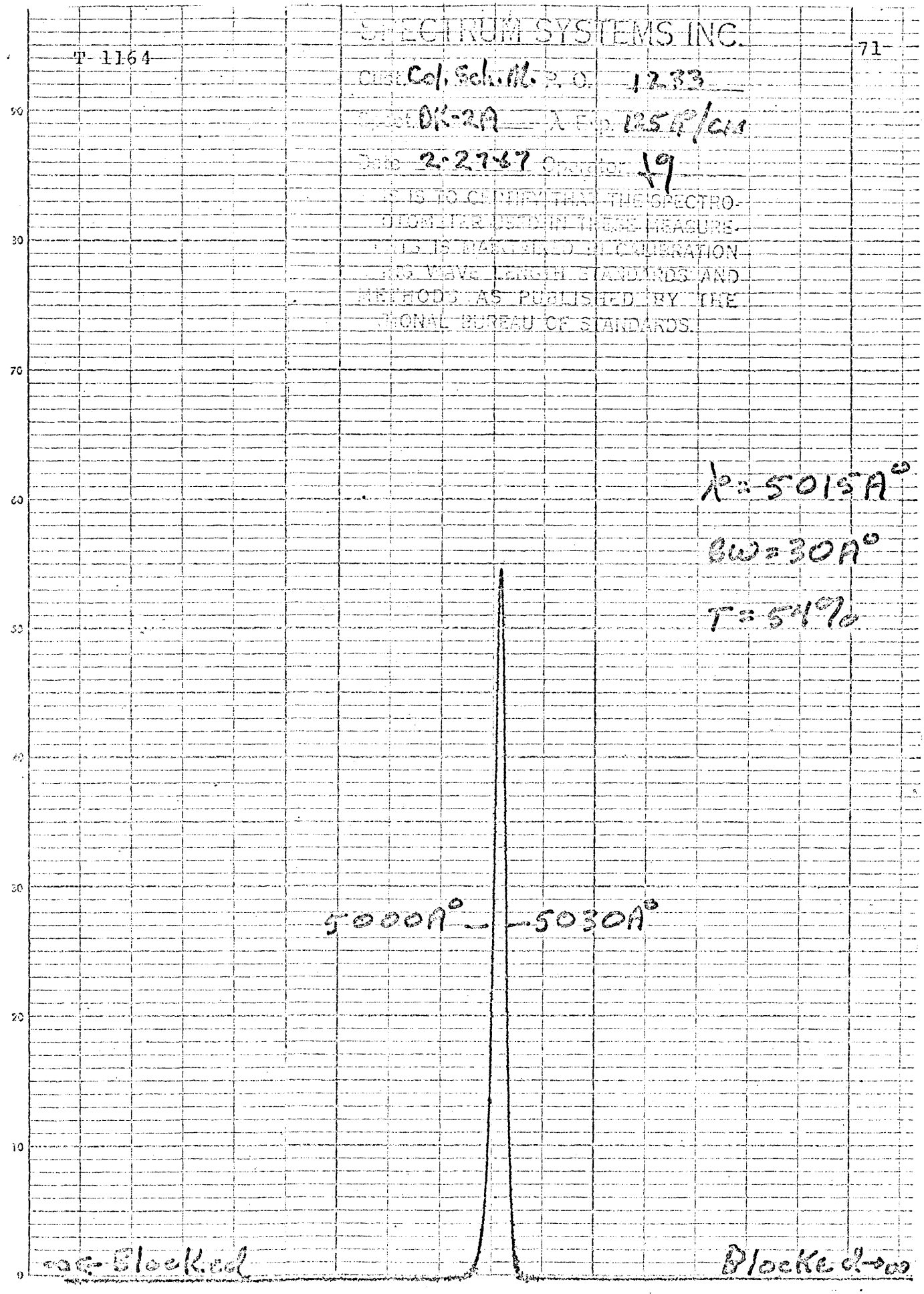

Figure 22. Specifications of the Spectrum Systems Filter.

C. Mechanical Construction of the Fabry-Perot Interferometer

The mechanical functions performed by the interferometer include:

(1) Changing the plate spacing smoothly and slowly.

(2) Adjusting the plates parallel and maintaining the parallelism while one of the plates is moved.

(3) Simultaneous movement of the capacitor and Fabry-Perot plates.

Unless otherwise stated, the material used to construct the interferometer was an aluminum alloy 6061-T6 selected because it machines well and is relatively inexpensive. In those parts of the instrument requiring accurate flatness, i.e. the parallelogram, stock was used that was flat to 0.001 in. Mating parts of moving devices were constructed of both brass and aluminum (e.g. sliding plates, threaded holes, threaded rods, etc.) because of the tendency of sliding aluminum surfaces to stick together. All leaf spring used was made of phosphorous bronze.

c-1. Adjustment and Motion of the Interferometer Plates

The most common means of producing parallel motion is that of the slide. If parallel motion is to be accurate and smooth, the slide will fall far short because of the expense involved in machining an accurate sliding surface and because of the inevitable presence of stick and slip friction.

Instead, a device that is being used more frequently is the parallelogram (Kline, 1952; British . . ., 1963). It consists of two plates coupled together by reinforced leaf spring in the form of a parallelogram as shown schematically in fig. 19. Once the plates are adjusted accurately parallel, they will remain parallel when they are moved. In addition no stick and slip friction will be present since it moves by bending instead of sliding. A feature that makes this device practical as a micron displacement transducer is that small movements up to 0.4 in. without derangement of the fringes may be produced when the plates of the parallelogram are adjusted to $\pm$.0002 in. (Kline, 1952, p. 39) at all four corners. The actual construction of the parallelogram is illustrated in fig. 23. If the upper plate bends as the parallelogram is moved, the upper plate will not move parallel to the base plate. The two ribs spanning the upper plate are designed to reduce this bending. The spacing between the top and bottom plates was adjusted at all four corners to within 0.001 in. This adjustment was found to be adequate with movements up to 150μ in. in the assembled instrument.

The mounting for the interferometer plates consists of a cell to hold each optical flat and two supporting brackets to provide for adjustment of the Fabry-Perot plates (see figs. 24 and 25). In the cells holding the optical

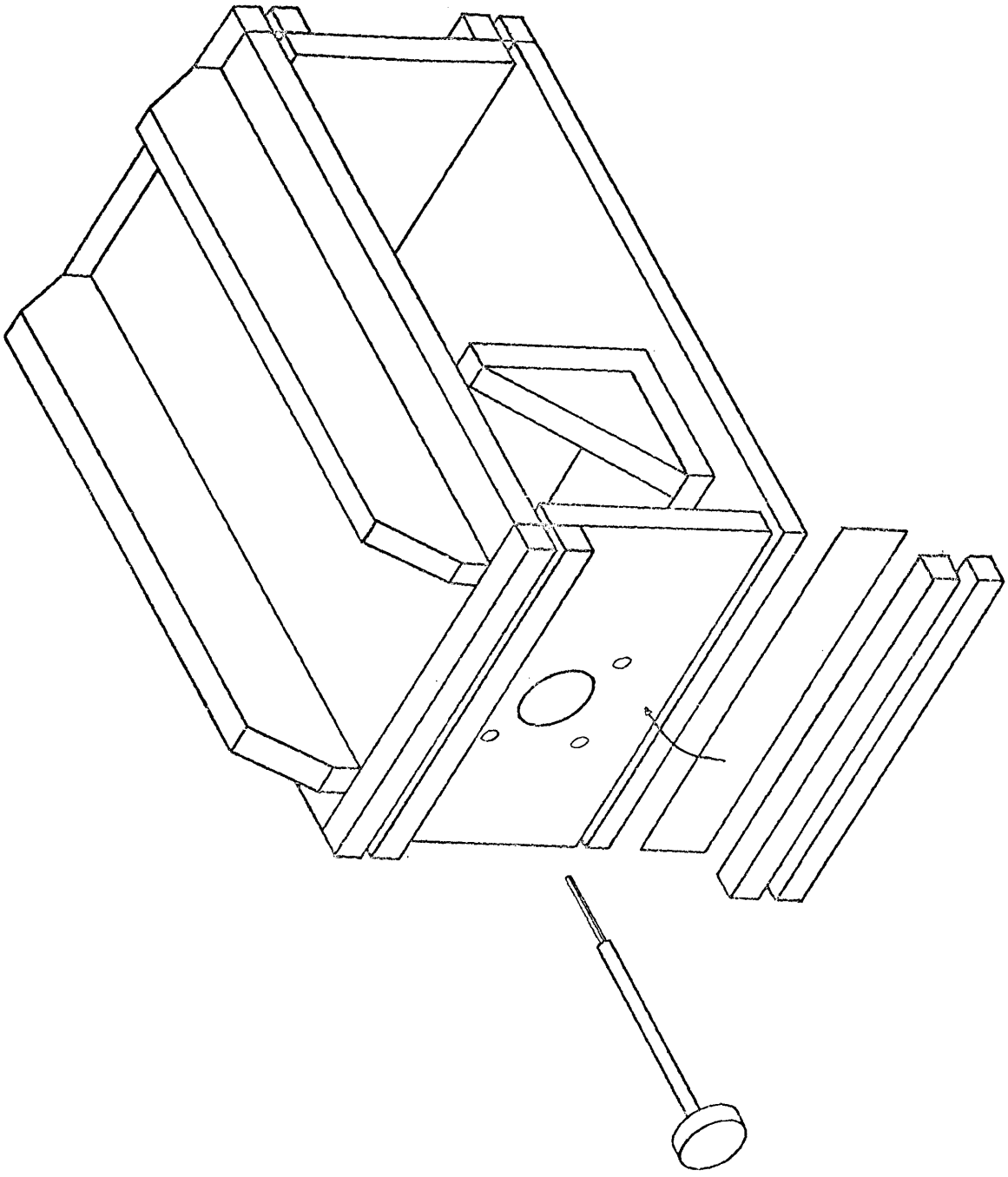

Figure 23. Isometric View of the Parallelogram.

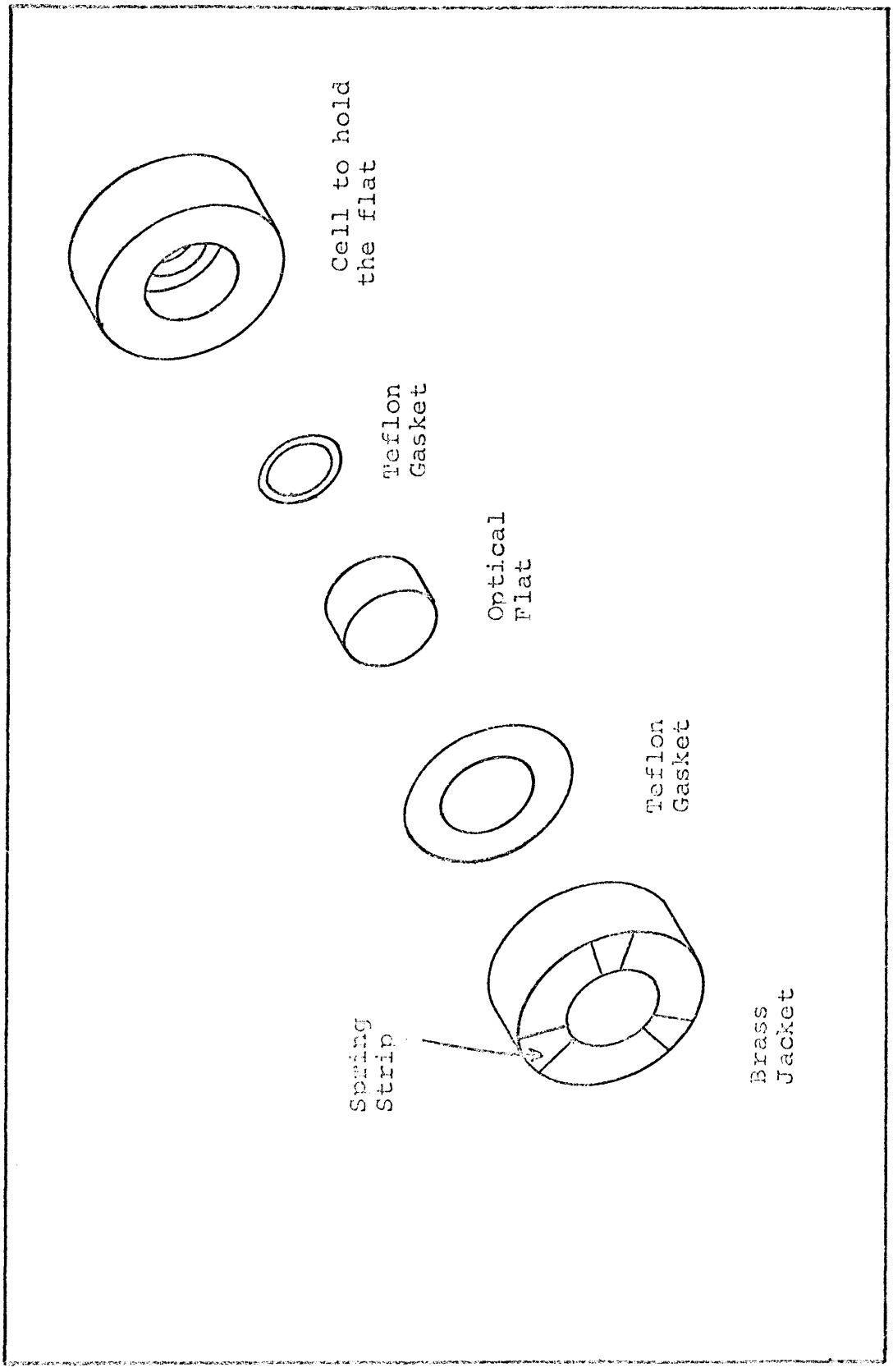

Figure 24. Exploded View of the Flatholding Cell.

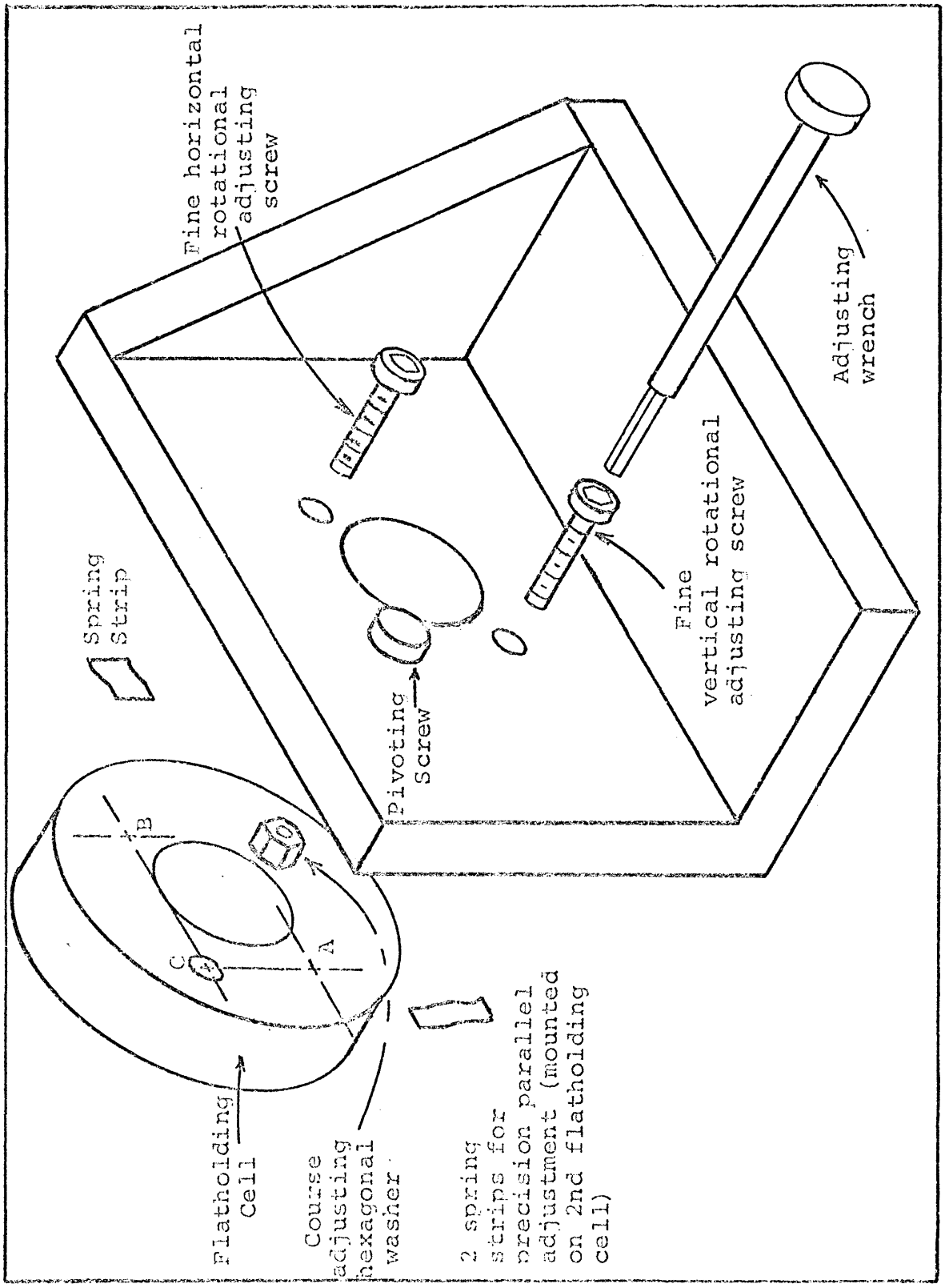

Figure 25. Exploded View of the Mounting for the Optical Flat.

flats, Teflon washers and gaskets are used to prevent direct contact between the glass and metal surfaces. The brass jacket which fits over both the flat and cell has three spring strips (see fig. 24) which provide gentle but steady pressure to hold the flats fixed within the cell.

The supporting bracket in fig. 25 is constructed from angle stock and is reinforced at the sides by triangular plates to minimize any bending or warping. The adjusting mechanisms include a hexagonal washer, one face of which has been milled at about a one-degree angle to the second face. The washer is inserted between the cell and the bracket. With the cell pushing the washer against the bracket, a coarse parallel adjustment between the flats is obtained by a rotation of the washers. A finer adjustment is produced by two 4-40 Allen head screws pushing directly against the cell. Each screw is placed at right angles to lines AC and CB passing through the pivoting screw at C. Hence pressure applied by screw A will produce a vertical rotation of the cell about axis BC. Similarly screw B will produce a horizontal rotation about axis CA. On the second mount, two spring strips are fastened onto the cell as shown in fig. 25 so that now screws A and B will push against the springs, producing a finer controlled adjustment than that produced on the first mount. The springs reduce the torque to bend

the holding screw which gives the plate a smaller rotation for a given movement of the adjusting screw. The completed parallelogram is shown in fig. 26 and fig. 27.

c-2. The Drive System

The requirements to be put on the drive system are that the motion it produces be slow and smooth. Because the least count of the wavelength scale is about 10μ in. and the drum speeds of the chart recorder vary from 3/4 in. per min to 12 in. per hour, it becomes desirable to produce movements at about 10μ in. per min. With these slow velocities the recorded peaks would be sufficiently far apart so that the position of the peaks could be easily determined.

Initially two mechanical devices which are described below were tried, but due to the coarse, uneven motion produced they were rejected. Both devices made use of a commercial differential micrometer screw rated to produce linear movements of 250μ in. per revolution. First a screw drive using this micrometer with a worm and gear assembly was tried, but due to appreciable friction developed between the gears, this arrangement is not recommended.

The second arrangement using this micrometer screw was suggested by Dr. John V. Kline. For this particular arrangement a precision 10:1 spur gear assembly transmitted rotational motion from a 1 rpm clock motor to the screw. In

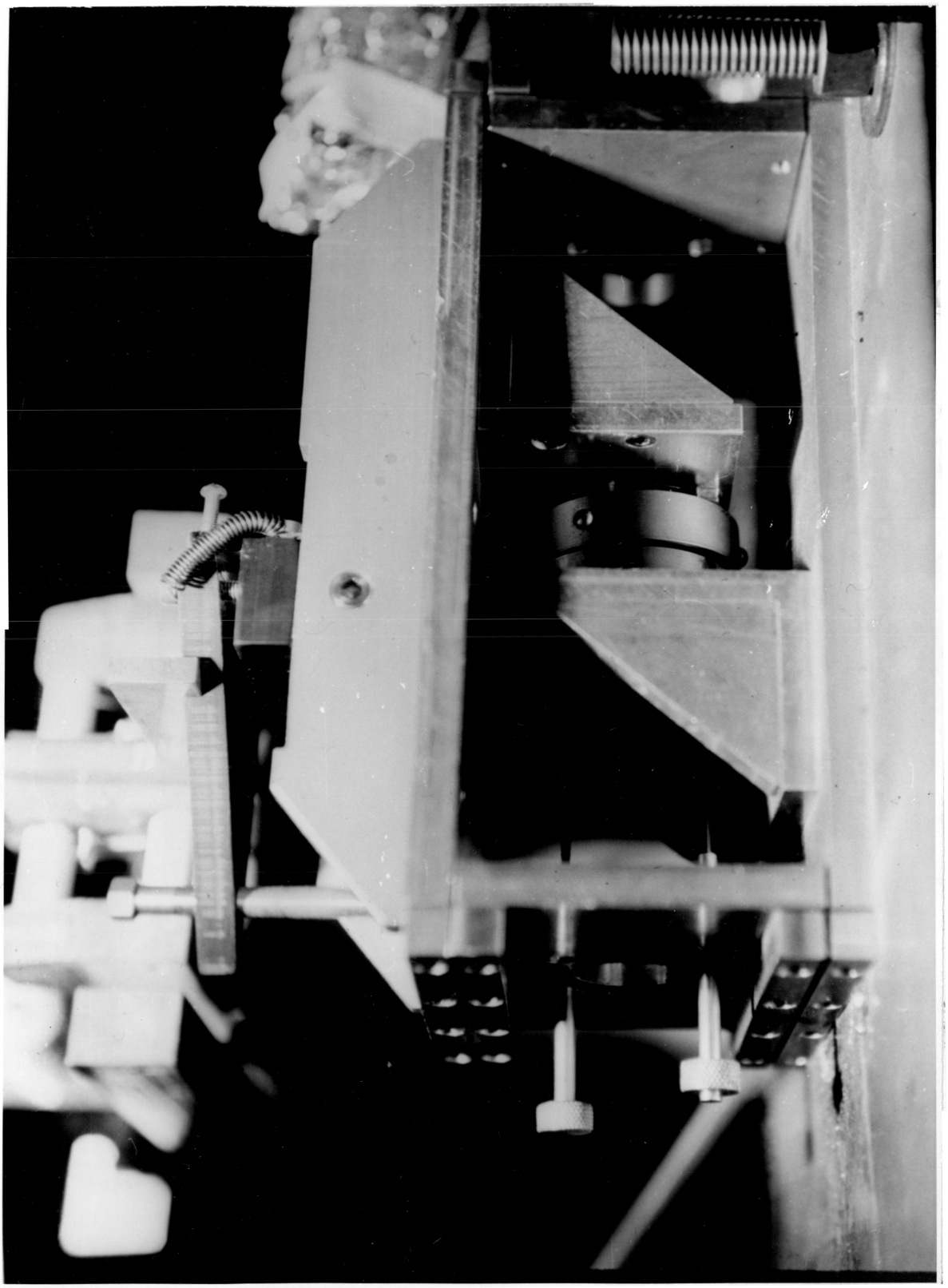

Figure 26. The Assembled Parallelogram.

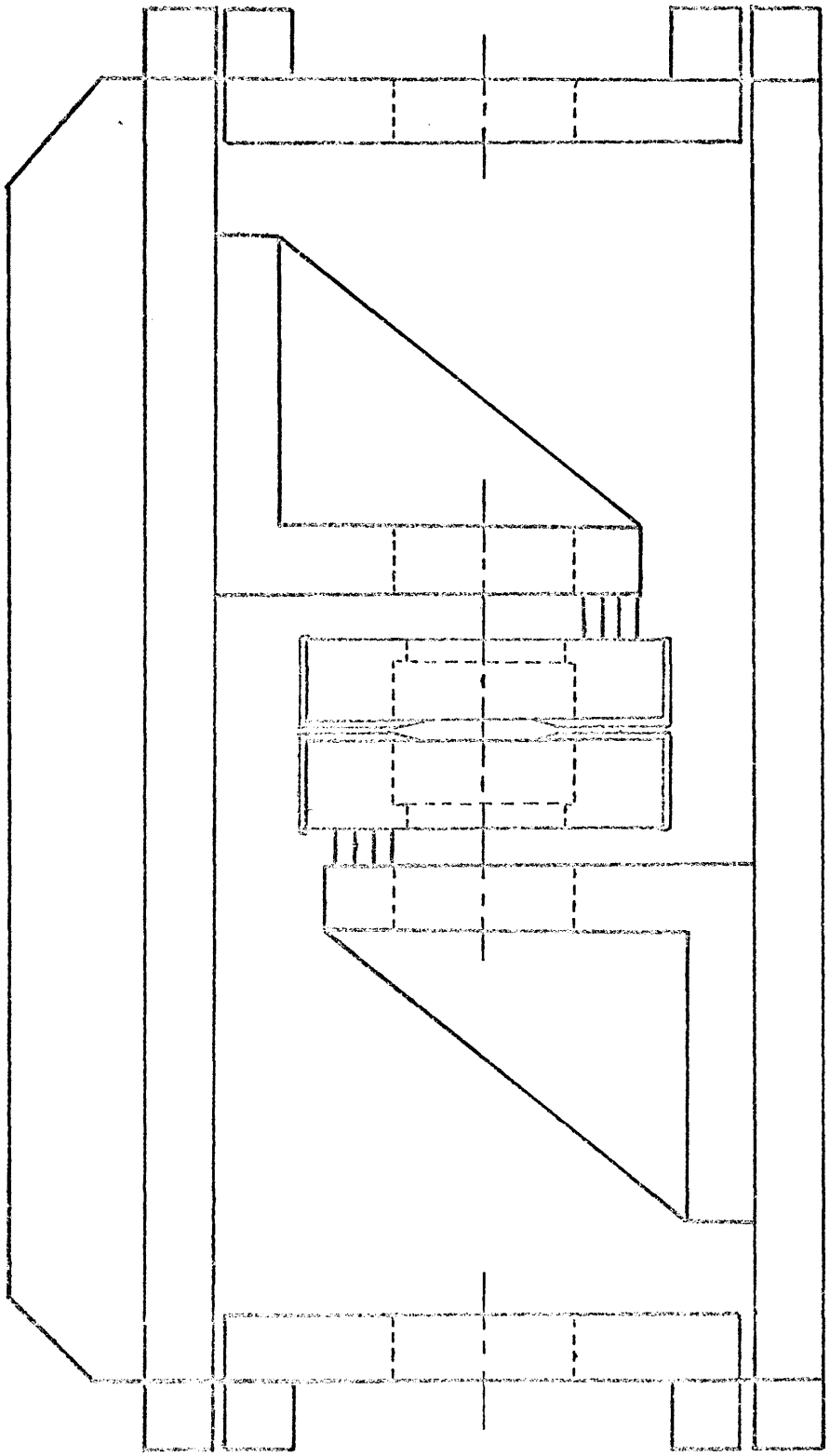

Figure 27. Profile View of the Parallelogram.

this mounting the motor was allowed to ride freely on the spur gear that was fastened to the body of the screw. This gravity coupling was able to absorb any eccentricity of the gears. The linear motion produced in this instance was 25μ in. per min. The unusual quietness of the clock motor accounted for the almost smooth motion transmitted to the plates. Unfortunately friction developed within the internal mechanism of the screw, and because this friction could not be immediately eliminated, the screw was abandoned.

In the method finally used, the parallelogram was spring-loaded against a steel tube that was allowed to expand and then contract when it was alternately heated and cooled. The heating element consists of a ceramic core which is wound with nichrome wire. The wire-wound core assembly is easily fitted into the tube and mounted as shown in fig. 28. Velocities down to 10μ in. per min were produced by controlling the current being supplied to the wire. This was accomplished by connecting a variable auto transformer to the primary of a 6.3-volt transformer.

Heat conducted from the tube to the parallelogram was substantially reduced by placing a bakelite spacer between the tube and the parallelogram and by covering the heating element with styrofoam and aluminum foil. The only real disadvantages of this system are that the velocity produced

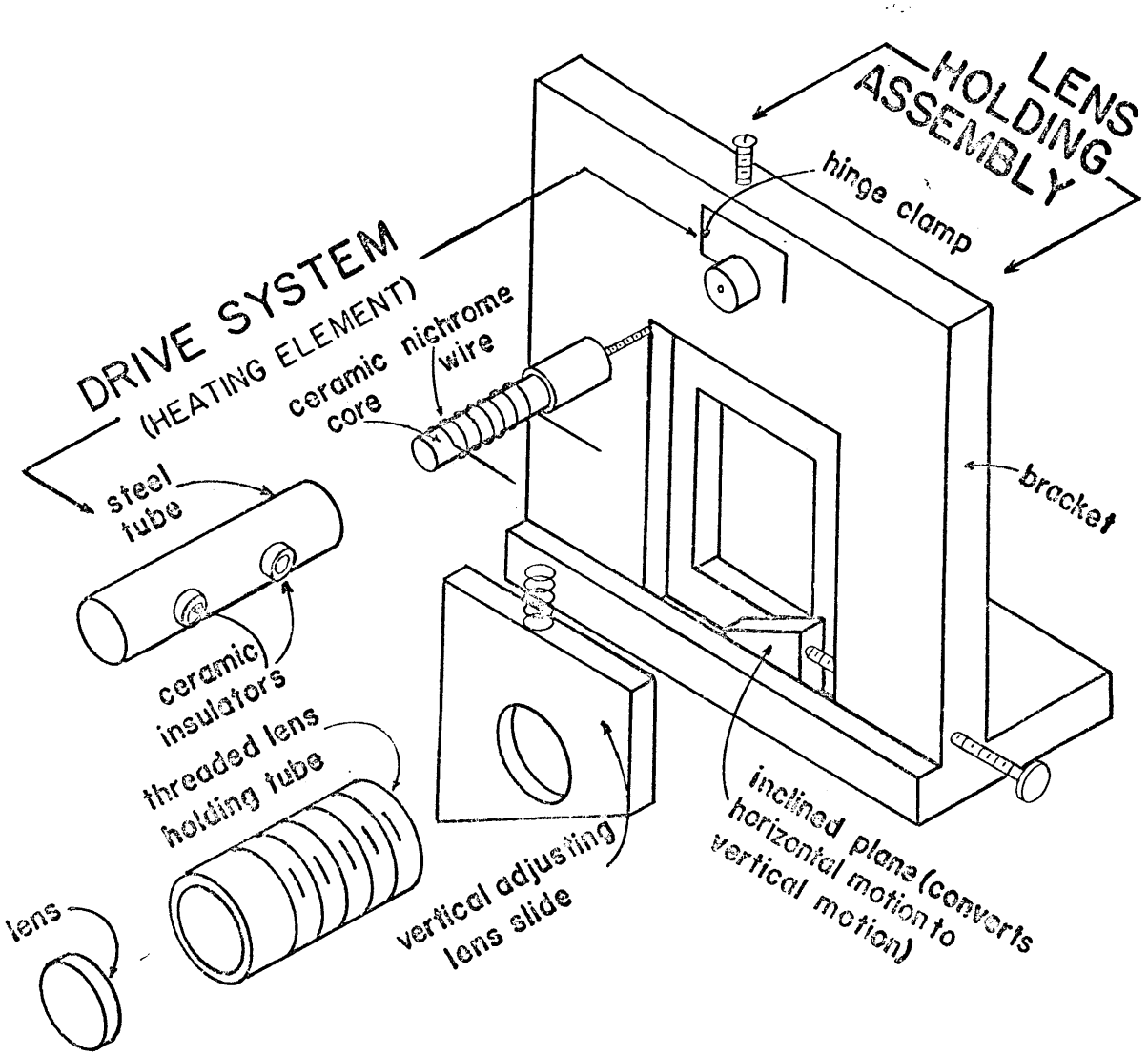

Figure 28. Exploded View of the Mounting for the Drive System and Lens #3.

is not constant, and the driving motion due to the heating element cannot be stopped at will. Nevertheless this driving system satisfies the requirements that the motion be slow and smooth, and in addition this arrangement is easy to construct and mount.

c-3. Mounting of the Central Capacitor Plate

The mounting which fixes the position of the central capacitor plate between the outer plates of the transducer is shown in figs. 29 and 30. The capacitor plate is set into a ¼-in. wide by ¼-in. deep groove which is milled into the adjusting base. The adjusting base is fastened to a supporting pedestal by a single brass screw P. Screw D pushes against and makes point contact with the upper surface of the pedestal. The lower portion of the pedestal is made of brass and is fastened to the upper plate of the parallelogram. The adjusting base and the upper portion of the pedestal are constructed from bakelite in order that a minimum separation of ½ in. be maintained between the metal parts of the interferometer and the transducer; thus stray capacitance between the transducer and the interferometer will be reduced.

The position of the capacitor plate is adjusted by screws A and B. Screw A with spring S produces a rotation about the vertical axis through P while screw B controls the

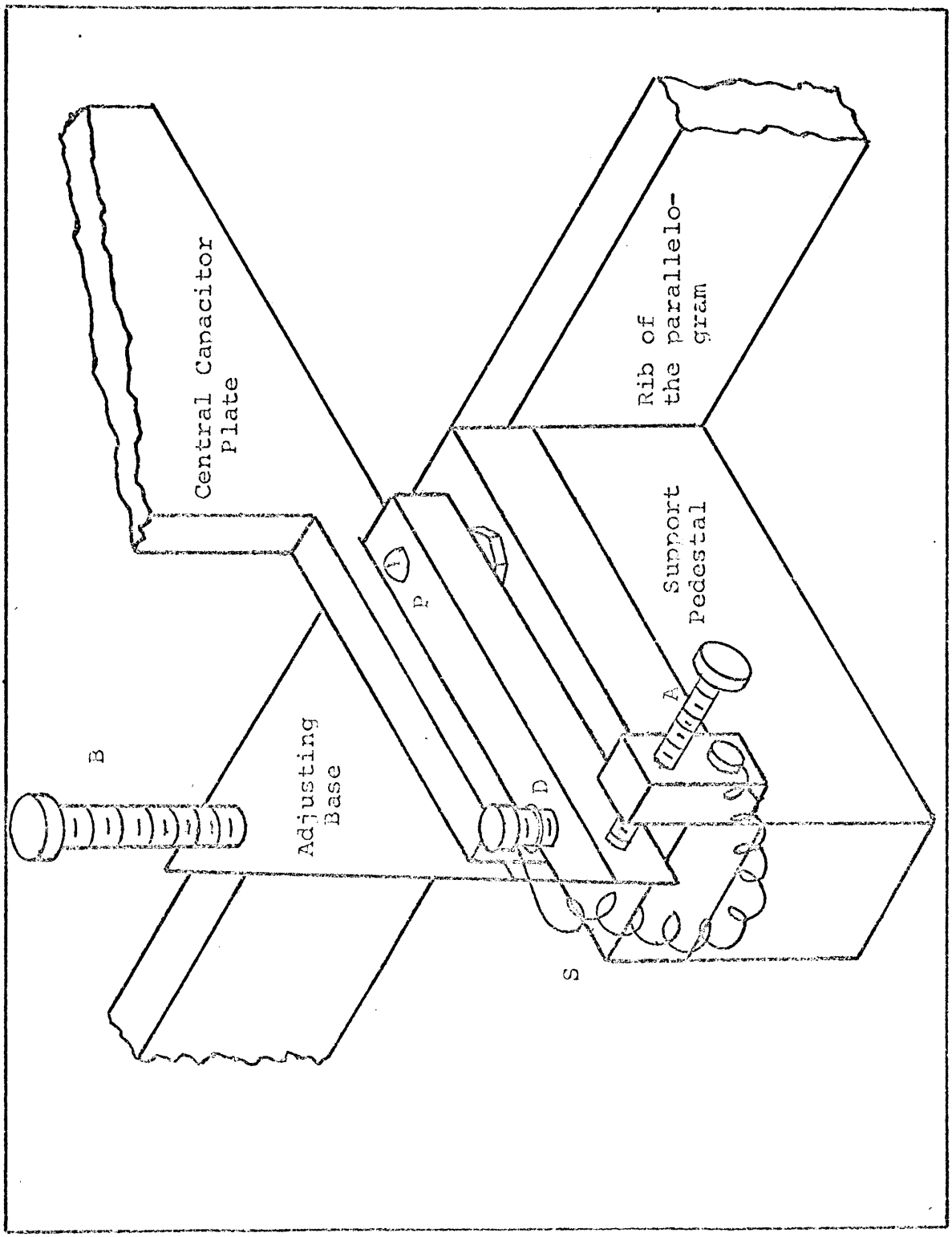

Figure 29. The Mounting for the Capacitor Plate.

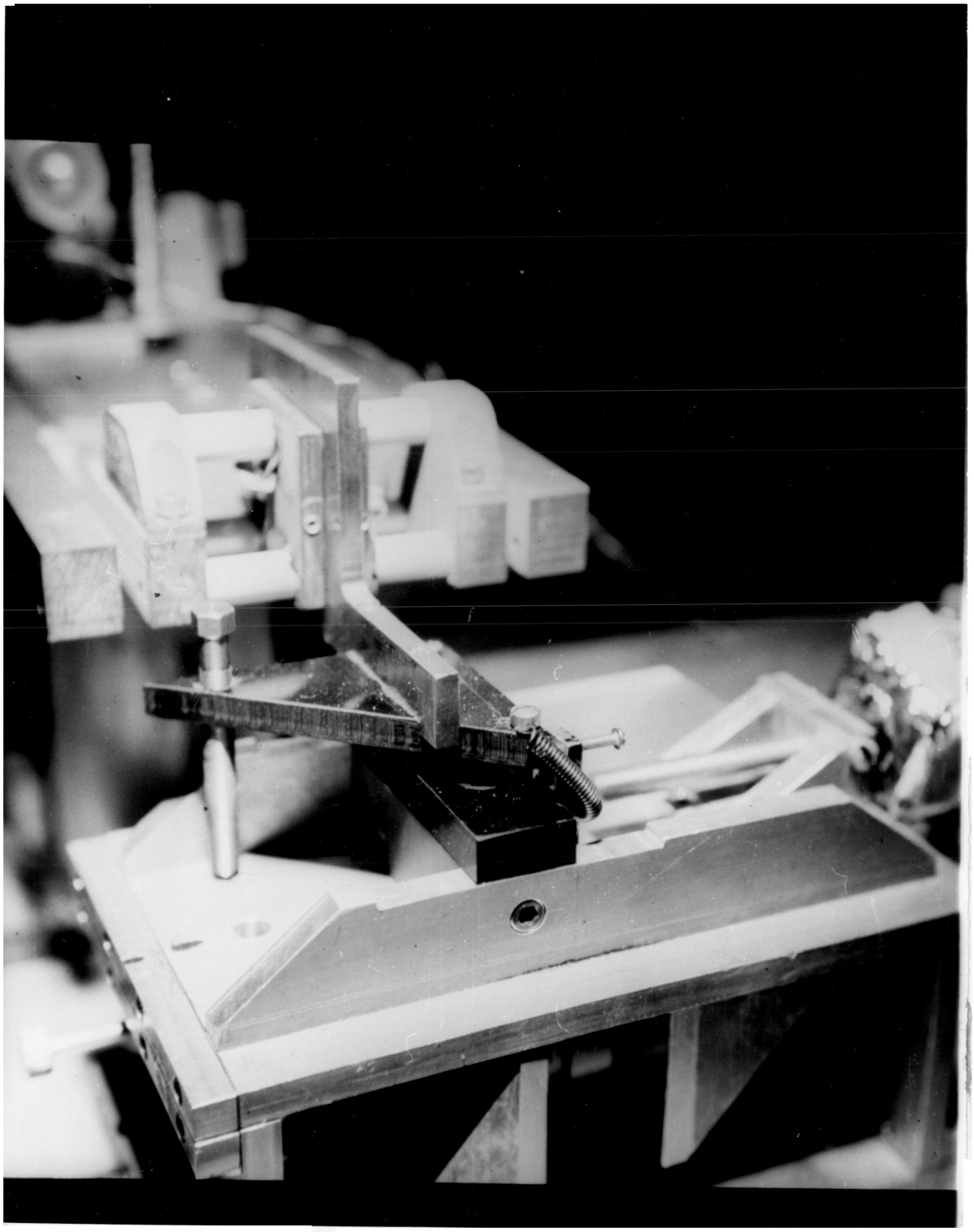

Figure 30. Capacitor Coupling of the Strainmeter Transducer to the Interferometer.

rotation of the base about the horizontal axis DP.

Spring S and screw D stabilize the entire assembly so that any motion of the parallelogram is transmitted simultaneously to the capacitor plate.

c-4. Pinhole and Lens Mountings

The mounts for the lenses and the pinholes are discussed together because they fix the direction of the optical axis. To bring these optical elements into final alignment, slides providing vertical and horizontal adjustments are used. For simplicity one pinhole has a vertical slide and the other a horizontal slide. Figure 31 illustrates the horizontal slide for pinhole #2 and fig. 28 illustrates the vertical slide for the lens #3.

In addition to vertical and horizontal control, the lenses which are set into a threaded tube with "Tackiwax," are advanced along the optical axis in order to place the pinholes at the focal point of the lenses.

c-5. Other Mechanical Structures

In this section the remaining mechanical elements are described.

(a) Mounting for the Light Source - The light source is encased in an aluminum tube, which in addition to the optical functions previously described, serves two

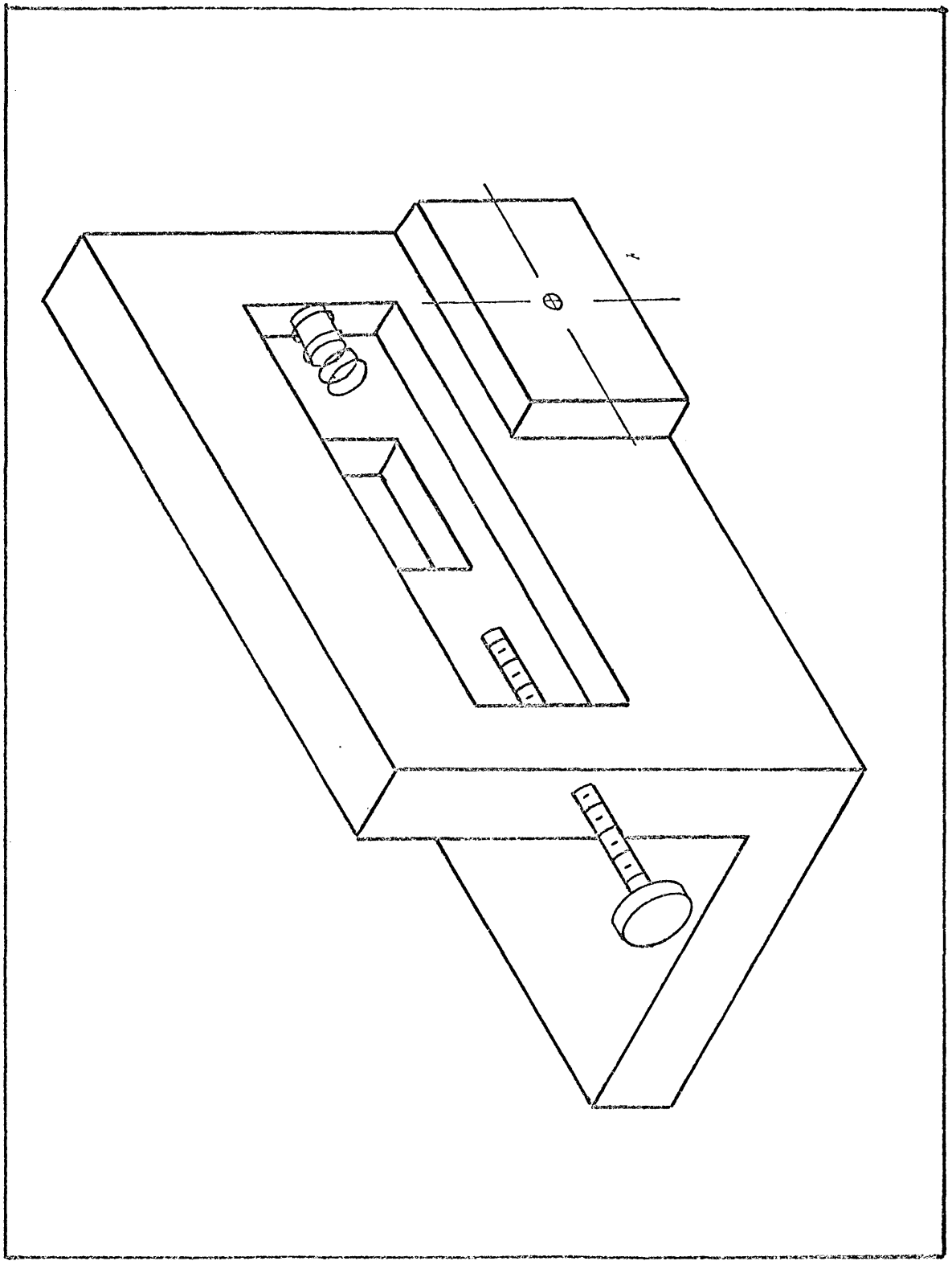

Figure 31. Mounting for Pinhole #2 Slide.

mechanical functions; it provides support for the light source and the water jacket. In the assembled instrument large drifts observed in calibration runs were traced to radiant heat transmitted from the light source to the strainmeter transducer. This heat radiation was considerably reduced by circulating water continuously through copper tubing that was wound about the aluminum tube (see fig. 32).

(b) Light Shield Housing Unit - The housing unit, designed to limit leak of stray light to the photocell, is a closed structure. It includes a mount for lens #1 (see figs. 32 and 36).

(c) Mirror Mounting - The mirror mount consists of an arbor and plate assembly which is clamped to a post fastened to the interferometer base plate. This is shown in fig. 32 and fig. 36. The mirror is held firmly to the plate with "Tackiwax." The clamp holding the mirror mount may be rotated in a vertical and horizontal plane. This clamp is commercially available from Cenco. The purpose of the mirror is to reduce the overall length of the instrument by bending the light from the source onto the principal axis passing through the interferometer.

(d) Mounting for the Filter - The filter has the dimensions 1 by 1 in. and is mounted in a 2-in. square aluminum

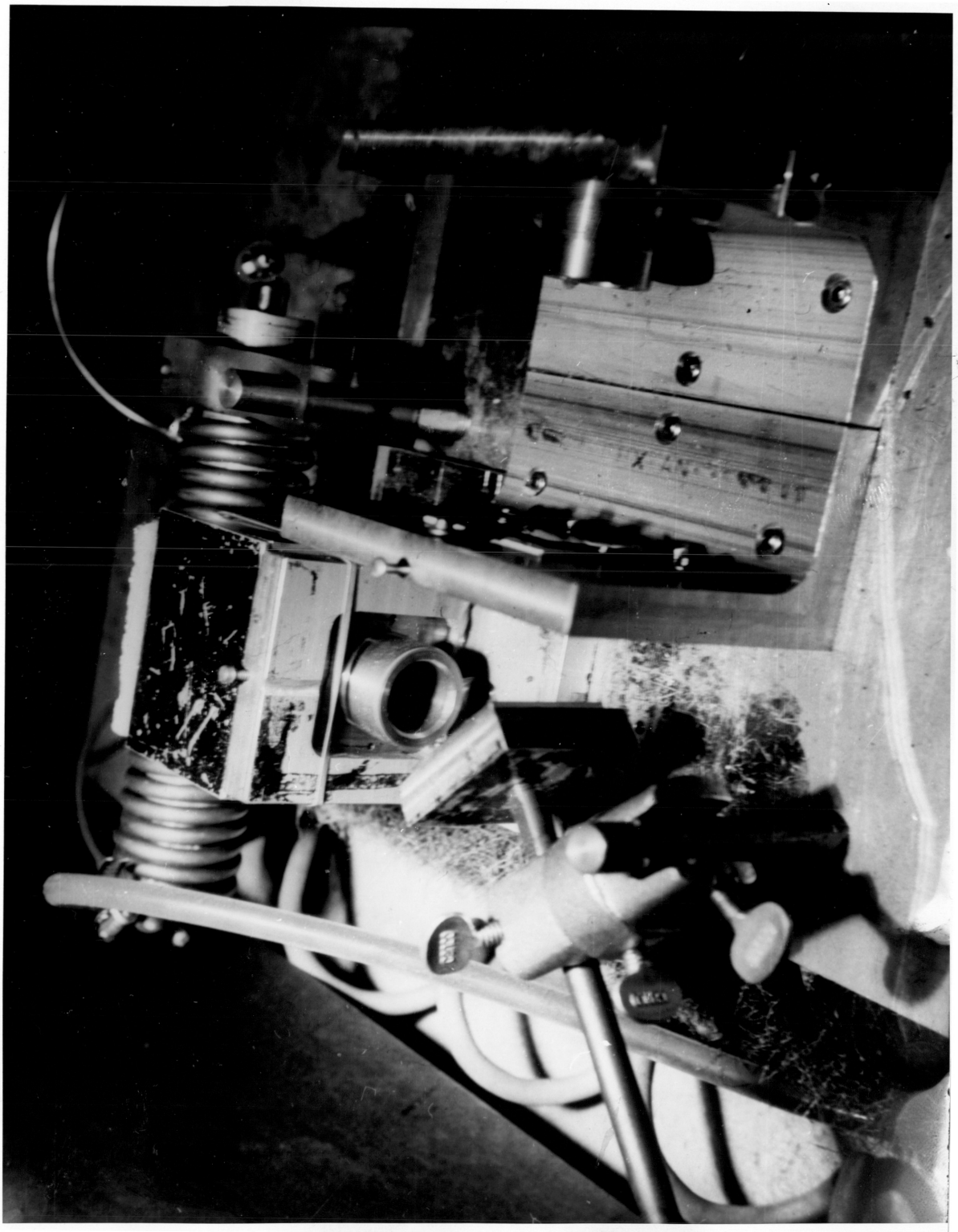

Figure 32. Construction of the Light Source.

frame. The frame is held by three spring clips in a recessed shoulder milled into the pinhole #1 bracket.

(e) Photocell Mounting - A photomultiplier tube which is 3¼ in. long is mounted on a minibox containing the photocell circuit. A light shield constructed of $1\frac{3}{8}$-in. diam. steel tubing is fitted over the tube and fastened to the minibox. An aperture just large enough to pass all light of the pinhole image, is drilled into the light shield.

D. Electrical and Electronic Components

(a) The Light Source

The light source is powered by a 5000-volt, 0.2-amp transformer. Transformers of this type are inexpensive and readily available from neon supply houses. The 60 Hz. alternating current (1 Hz. = 1 C/sec) operating the light source, causes emission of light with 120 Hz. flicker which must be considered in the design of the photodetector system.

(b) Photodetection System

Light from the interferometer is passed through the final pinhole onto a photomultiplier tube. The output current from the anode is rectified and smoothed, and is then recorded by an Esterline Angus pen recorder. Figure 33 is a block diagram giving an overall picture of the photodetection system.

The photomultiplier tube was chosen for its low noise and high gain characteristics. In particular a 931-A tube was selected because of low cost and suitable spectral response. It exhibits 70 percent of maximum sensitivity at 5000 Å. An operating voltage of 600 volts was required for operation of the tube with a sufficient gain to detect the interferometer signal. The circuit of the tube is shown in fig. 34.

In the design of the rectifier circuit, the following factors must be considered.

(1) The 600 volt D.C. on the high side of the signal output (at A in fig. 34) must be filtered out before the amplified photo signal is rectified.

(2) The 120 Hz. flicker of the light source is amplitude modulated by the movement of the interferometer plates. This 120 Hz. modulated carrier must be rectified before delivering the signal to a D.C. recorder.

Since the fringe velocity is about one fringe every 45 sec, the light flux will vary from the peak value to 1/10 peak value in about 4.5 sec (see ch. II, sec. c-2). This requires full-scale motion of the pen in a few seconds.

The rectifying circuit is coupled with the recorder as shown in fig. 35. The recording system used is an Esterline Angus 5-in. chart recorder-Series S model S-601-S. In this

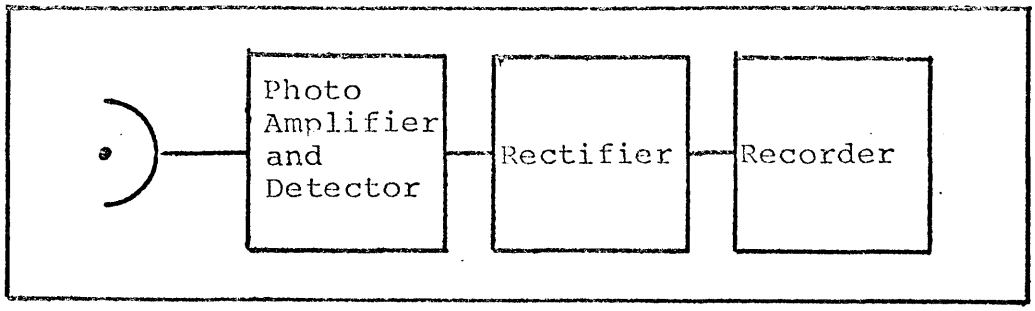

Figure 33. Block Diagram of the Photo Detection System.

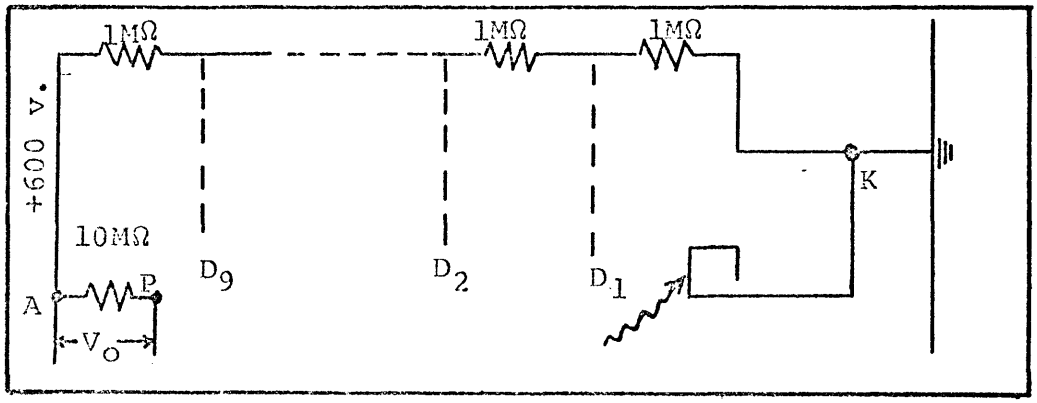

V_o = Signal Output D = Dynode
K = Cathode A = Anode

Figure 34. Circuit of the Photomultiplier Tube.

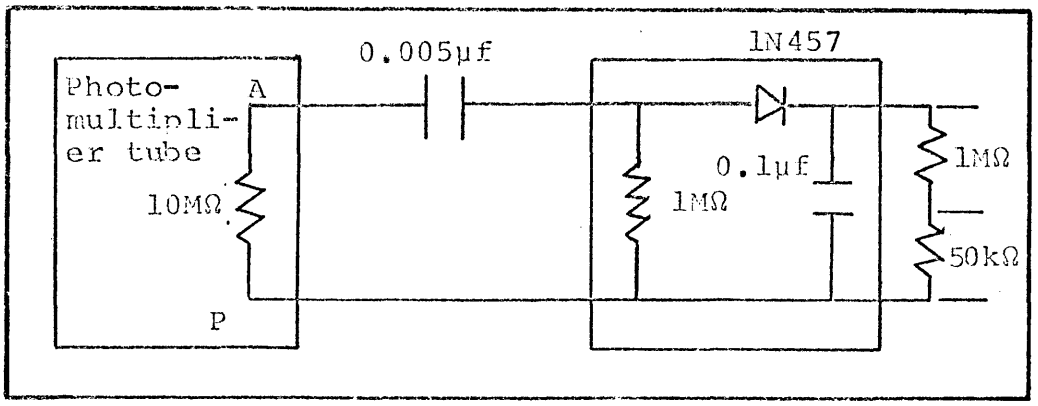

Figure 35. The Rectifier Circuit.

recorder the range of full-scale voltages go from 1 mv to 100 v. The chart may be operated at speeds ranging from 12 in./hr to 3/4 in./min.

E. Assembly and Mounting of the Interferometer

All mechanical and optical components are mounted on a 1-ft by 3-ft by 1¼-in. aluminum base plate as is schematically illustrated in fig. 36. The brackets mounting the optical components have been drilled with 1-in.-diam holes (except for the pinhole #2 slide, fig. 31) in order to pass light from the source to the photocell. Before the parallelogram and the other optical elements were permanently fastened upon the base plate, it was necessary to adjust the flats approximately parallel (see ch. IV, sec. a-1). This adjustment allows one to mount all optical elements so that the principal axis may be properly oriented by having it pass near the centers of all apertures in the optical system. Once assembly of the interferometer is completed, the base plate, which is then fastened to a cement pier, is partially insulated from the pier by rubberized packing.

F. Mounting of the Transducer

The mounting of the transducer consists of a hollow cylindrical pedestal which has three screws providing stable

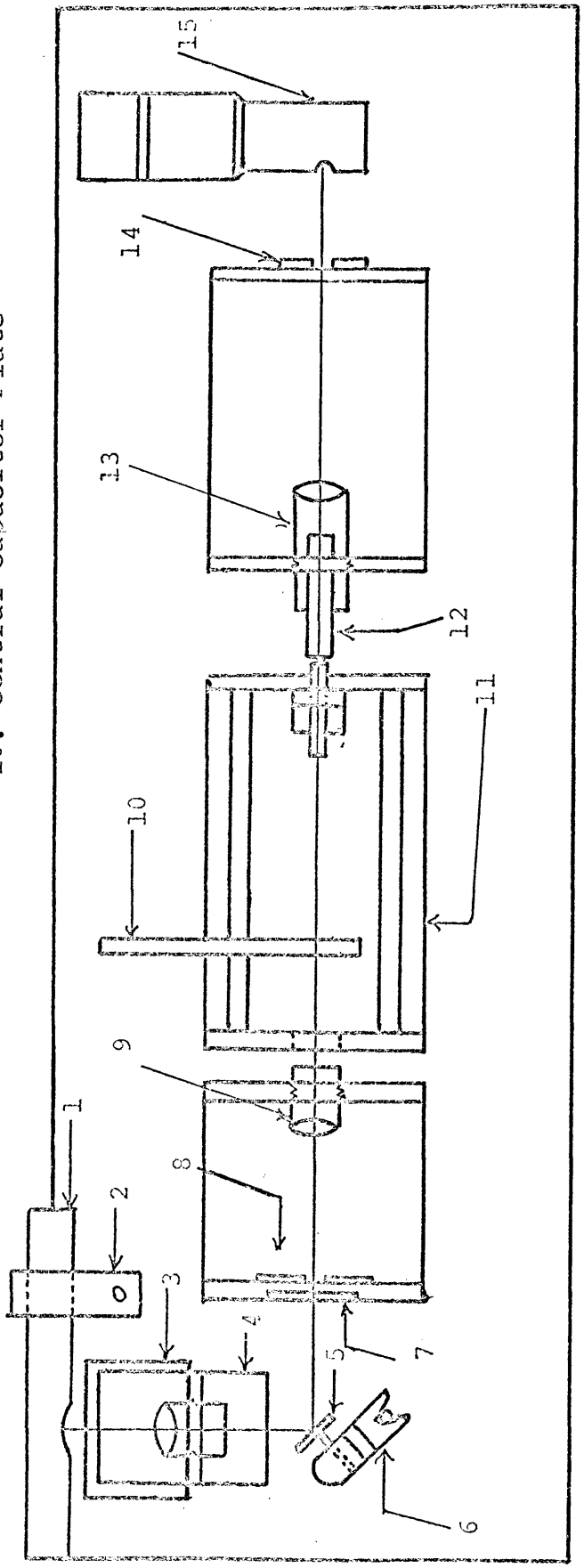

Figure 36. The Assembled Interferometer.

support in the form of a three-point kinematic mount. The transducer is mounted on the pedestal in such a way that the central capacitor plate on the parallelogram and those on the transducer will intermesh (see fig. 30). In order to minimize the edge effects of the capacitor plates, the 3-in. square central plate is centered with respect to the 2-in. square outer plates of the transducer. The transducer is firmly mounted by passing a threaded rod through the center of gravity of the transducer and anchoring the rod to the cement pier.

The transducer is designed so that the gap on either side of the ¼-in.-thick central plate is 0.013 in. The central plate may be centered approximately between the outer plates by both rotating the transducer and adjusting the position of the central capacitor plate as described in sec. c-3.

With the construction of the interferometer completed, (see fig. 37) the calibration system may now be set up for operation as described in ch. IV.

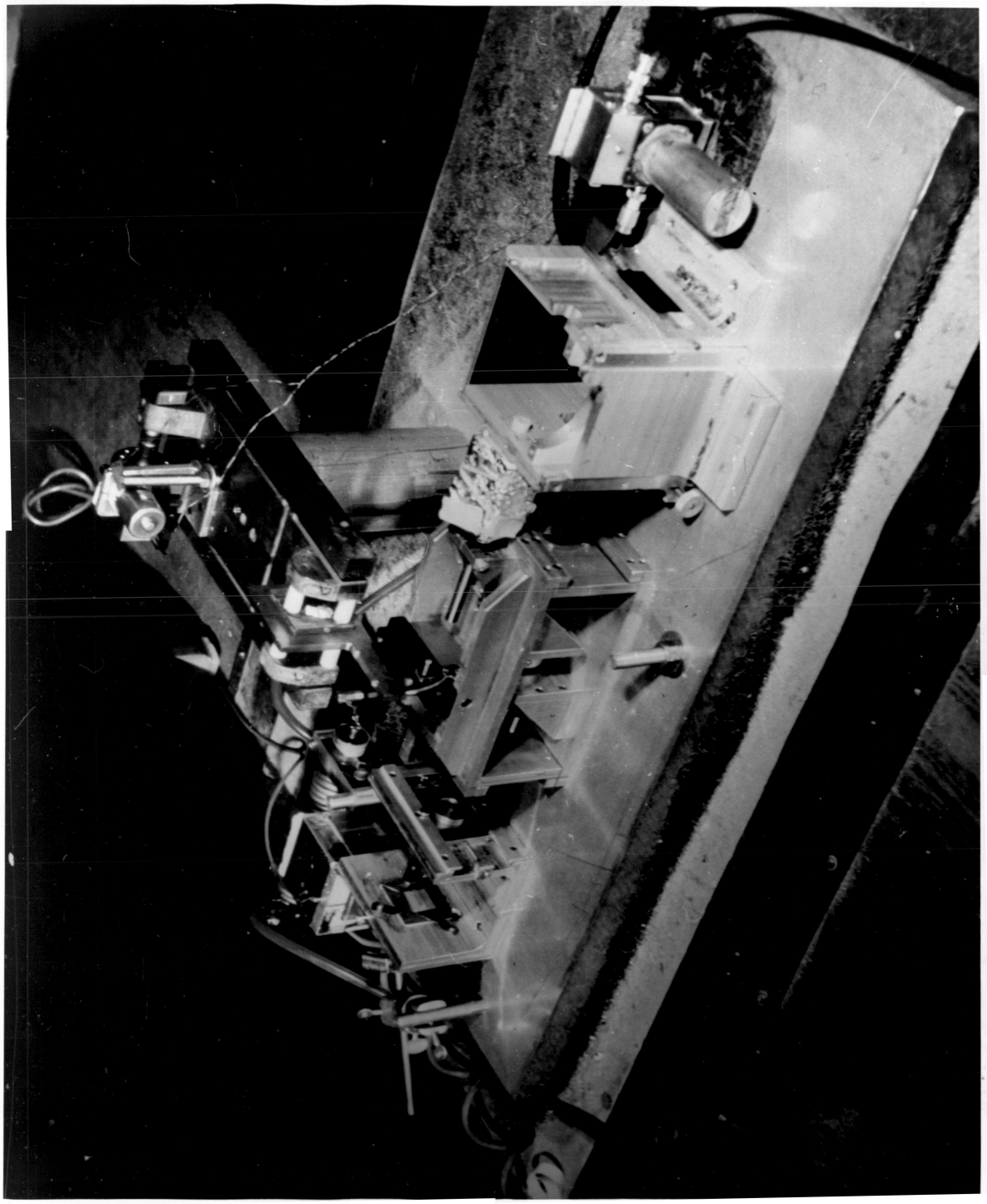

Figure 37. Side View of the Interferometer.

IV. OPERATION

This chapter describes the adjustments of the interferometer and the transducer. In addition the calibration operation and the procedure for computing the calibration scale factor for the strainmeter transducer is described.

A. Adjustment of the Interferometer

A preliminary parallel adjustment of the Fabry-Perot plates is needed to find the optical axis of the interferometer (see ch. III, sec. E). The procedure for adjusting the interferometer is outlined below (see also figs. 21 and 36):

(1) a - The Fabry-Perot plates are set roughly parallel to each other.
    b - The optical components are mounted on the base plate so that the principal axis of the interferometer is approximately determined.

(2) The lenses are adjusted so that their focal points and the positions of the corresponding pinholes coincide.

(3) The pinholes are centered onto the principal axis of the optical system.

(4) The Fabry-Perot plates are precisely set parallel to each other.

a-1. Preliminary Adjustment of the Interferometer Plates

The interferometer plates may be approximately adjusted by one of two methods. In the first, the images of the plates transmitted through the apertures of the parallelogram, are observed directly with the eye. Manipulation of the adjusting screws on the cells holding the flats makes visible an interference pattern containing rings (fringes of equal inclination).

In the first adjustment the hexagonal washers (illustrated in fig. 25) on both cells are rotated until fringes of equal thickness (dark and light bands) appear indicating that the wedge angle between the plates is small. Adjustment of the finer controls will make the plates almost parallel when the fringes become circular. If the central zone of the ring pattern is made to coincide with the center of the aperture, the Fabry-Perot plates will be normal to the principal axis. The final adjustment before the parallelogram is mounted on the base plate is accomplished by moving one's eye vertically and horizontally. Any change in the size of the circular fringes will indicate that the plates are not yet parallel. The spring adjusting screws are then manipulated until no expansion or contraction of

the rings is observed. This will make the plates sufficiently near parallelism to suffice until the other adjustments of the interferometer optical system are completed.

The above method is fairly long and difficult. A simpler procedure is to use a laser beam as the light source and to project the image of the source onto a screen. The plates will be nearly parallel when their adjustment causes the images to coincide. Since the interference pattern is not directly observed, other means will be used to adjust the plate approximately normal to the optical axis. The laser beam is used to define an approximate optical axis. By rotation of the hexagonal washer one may cause the laser beam, reflected from the plates to fall back on the source. At this point the plates are perpendicular to the beam. Then manipulation of the adjusting screws will make the Fabry-Perot plates almost parallel when the projected images coincide.

The parallelogram is now bolted to the base, and the remaining optical components are set up on the base.

a-2. Lens Adjustments

For ease in description use is made of the nomenclature in figs. 21 and 36.

Three adjustments are required. In the first adjustment lens #2 is manipulated until its focal point lies at

pinhole #1. Lenses #2 and #3 are first placed in their mounts and, second, a long focal length microscope is set up behind the pinhole #2 mount so that a sharp image of the transmitted interference pattern is observed with the microscope. Pinhole #1 is now mounted, and lens #2 is adjusted until the image of pinhole #1 becomes sharp. The image of pinhole #1 now coincides with that of the interference pattern so that light rays emerge from lens #2, parallel to the optical axis.

The next adjustment is to move lens #3 so that its focal point lies at pinhole #2. First pinhole #1 is removed and a reference point, i.e. point of a surface gage, is placed at pinhole #2 where the focal point is to lie. The microscope is now focused sharply on this point. Lens #3 is moved until a sharp image of the interference pattern appears in the field of view of the microscope. The focal points of lens #3 and the microscope now lie in the vicinity of pinhole #2. Replacing the reference point by the pinhole #2 slide, the focal point of lens #3 is exactly positioned at pinhole #2 so that both the images of the transmitted interference pattern and of pinhole #2 lie exactly at the focal point of the microscope.

After the focal points of lenses #2 and #3 are properly positioned, lens #1 is now adjusted so that the light

source is focused on pinhole #1. A preliminary adjustment is made by noting where the image of the source comes into sharp focus on the pinhole #1 slide. In order to focus the source precisely on pinhole #1, all pinholes slides are first removed without rotating the slide adjusting screws. The source is now viewed from an eye position behind the second pinhole. If the source image is not exactly at the focal point of lens #2, there will be parallax between the source image and the fringe pattern image. The source image will appear to lie at some finite distance from pinhole #2, where the interference pattern is focused. Lens #1 is now manipulated until no relative motion between the source and fringe pattern images is detected when the eye is moved up and down or sideways. With this final adjustment the exact location of the focal points of all three lenses is now completed.

a-3. Centering of the Pinhole on the Optical Axis

In the following adjustments, the images are viewed from a position behind the second pinhole. With the focal points now adjusted as described in sec. a-2, pinhole #1 is mounted and then positioned onto the optical axis by manipulating the vertical slide that carries pinhole #1 and the horizontal slide that carries lens #2. This adjustment is completed when the central zone is centered with the pinhole.

The filter is now mounted. The next adjustment of the slides will position the pinhole so that it is concentric with circular rings of scattered light that are in the plane of the pinhole slide. For the final adjustment, pinhole #2 is placed in its mount, and by a series of similar manipulations of the pinhole #2 slide and the lens #3 slide, pinhole #2 is aligned with pinhole #1.

This completes the optical alignment. At this point the photomultiplier tube is mounted as described in ch. III, sec. c-5.

a-4. Final Adjustment of the Interferometer Plates

Before the interferometer can be operated, the Fabry-Perot plates are adjusted as near to parallelism as the flatness tolerance of the plates will permit. The filter is mounted, and the eye is placed at the second pinhole so that the plates are observed with the intensity of the central zone. One of the plates is then moved a few wavelengths, and the corresponding intensity change is observed. The two plates are parallel within the flatness tolerance when manipulation of the spring adjusting screws cause an integral order (region of maximum intensity) to appear and disappear uniformly on the plates. If any motion of the plate causes this zone of maximum intensity to move across the field of view, the plates are not sufficiently near parallelism.

B. Adjustment of the Strainmeter Transducer

The electronic transducer circuit is put in operation before the light source is cooled. Hence the transducer may then be used to determine when the instrument assembly has reached a state of equilibrium.

First the interferometer capacitor plate is mechanically centered between the outer plates of the transducer, as outlined in ch. III, sec. F; and then the transducer oscillating circuit is adjusted.

The procedure for adjusting the transducer requires a variation of L (see p.63) in order to obtain a linear response of the transducer output when the central plate is moved between the outer plates of the transducer. Adjustments of L and C changes the resonant frequency of the two L-C circuits, thus causing a horizontal displacement of the curves in fig. 20b. Specifically the variable inductors L_3 and L_4 of both tank circuits are tuned until the voltage output of each L-C circuit (measured across R_9 and R_{10}) is about 0.7 of the maximum voltage (V_r in fig. 20b). In the region about this voltage, the curves C_6 and C_7 approximate a straight line so that a small change in C_6 and C_7 will cause the two resonance curves to be displaced across the line ν = 1.5MHz in a linear manner. The total voltage output will be zero when the two L-C circuits are tuned so that

both resonance curves in fig. 20b coincide. Consequently the recorder chart zero should be set at the same time the two L-C circuits are tuned. The transducer is now adjusted, and once thermal equilibrium is reached, the transducer will be ready for operation.

C. Calibration

c-1. Operation of the Calibration System

To handle the calibration operation more efficiently, two devices are built into the instrument. A pentagonal cam mounted on the barrel of the screw shorts the transducer output about every fifth of a revolution. A shorting switch is also connected across the input of the transducer chart recorder. Its purpose is to superimpose manually the wavelength scale onto the transducer record.

Calibration was performed in a room where no special attempts at environmental control were made other than in cooling of the light source. The recording system was set up in an adjacent room so that calibration could be performed without the presence of an operator at the instrument site. It has been observed that any disturbances introduced at the instrument site (i.e. temperature change and vibration) produce large nonlinear drift in the transducer recording. The drift becomes small and linear in about an hour after

the disturbances are removed. Before and after each transducer run, the drift should be monitored for at least 10 minutes so that the drift corrections may be made when necessary.

Calibration of the transducer is performed in two steps. In the first step the central capacitor plate is fixed, and the motor driven differential screw is rotated through several revolutions, moving the outer plates of the transducer. The displacement velocity is inferred from the transducer output, which is directly read out in voltage change per minute. Because a periodic error may exist in the pitch of the screw threads, the velocity of the capacitor plates is not linear. But on the average the same displacement will be shown to occur each time the screw is turned through one complete revolution (see fig. 39). Measurements from the recording are used to calculate the scale factor in units of voltage change per screw revolution (rev).

The second step is to fix the outer plates at one position and move the upper plate of the parallelogram. Consequently the displacement of the central plate will be recorded simultaneously by the interferometer and the transducer. The latter recording includes the superimposed wavelength scale already described. From the transducer output,

the scale factor in half wavelengths ($\frac{1}{2}\lambda$) per unit voltage change is derived.

The product of the above two scale factors give the desired calibration in $\frac{\frac{1}{2}\lambda}{\text{rev}}$. The primary calibration is observed to be independent of the voltage response of the transducer to displacement. According to Romig (oral communication, 1967) any response variation will be small over periods of weeks. Hence a primary scale factor (in $\frac{\frac{1}{2}\lambda}{\text{rev}}$) that is independent of the transducer detection system can be achieved because variations in the transducer sensitivity are negligible during the normal 30-minute calibration run. Consequently the electronic detection system may be completely replaced without altering the primary calibration. This feature is also of great value in long-term strain studies because the voltage sensitivity is not stable over long time intervals.

c-2. Procedure for Computing the Calibration Factor

The calibration factor may be computed graphically. A second procedure, the method of least squares, provides a means of obtaining both the calibration factor and its uncertainty. However the graphical procedure may obtain the desired results more quickly. In general the results produced by the graphical procedure are almost as accurate as those obtained by the least-square method, but the uncertainty

in the measurement can only be estimated. Both methods will be used with the graphical procedure being demonstrated in this chapter and the least-square method in ch. V.

As already noted, calibration is performed in two operations. First the differential screw moves the transducer capacitor plates producing a recording with the output shorted five times per revolution of the screw. With a scan through several revolutions, one may plot the output versus each revolution scanned (Revolution number). Figure 38, a typical transducer recording, shows that the screw has been rotated through at least four revolutions. Hence from five sets of points (each set of points is identified by the letters A, B, C, D, and E), five lines may be drawn as illustrated in Fig. 39. The slopes in voltage change per screw revolution measured from these lines are then averaged to yield the scale factor of the transducer run.

Next the steel tube is alternately heated and allowed to cool (see ch. III, sec. c-2). Thus the steel tube drives the moving assembly of the interferometer in two opposite directions so that the voltage change recorded by the transducer varies continuously in one direction and then the other. Also at each peak of the interferometer wavelength scale (Fig. 43), the transducer output is shorted as described in sec. c-1 (see Fig. 40). The voltage reading

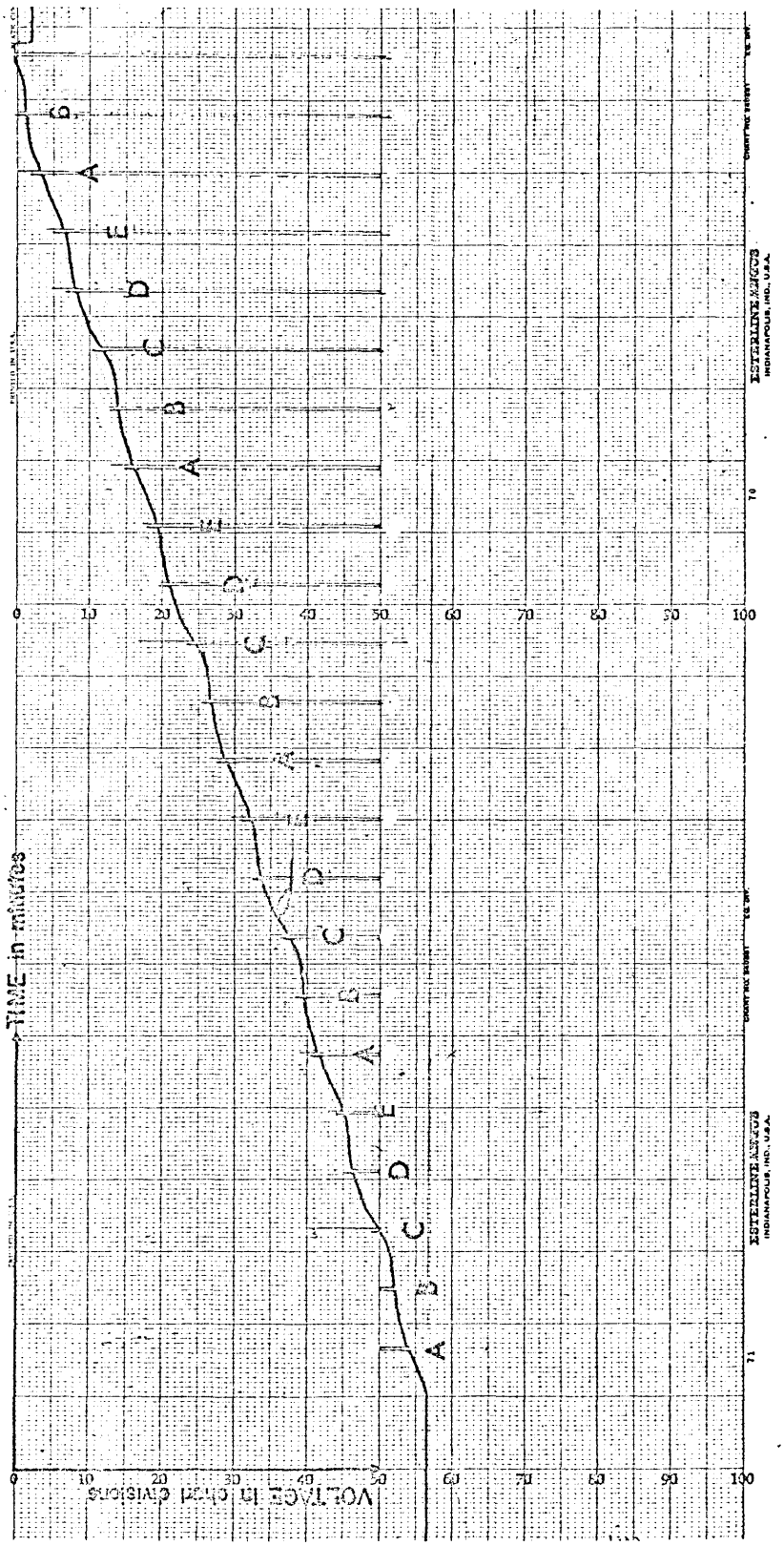

Figure 38. The Output Recording of the Transducer as Produced by a Displacement of the Transducer Capacitor Plates.

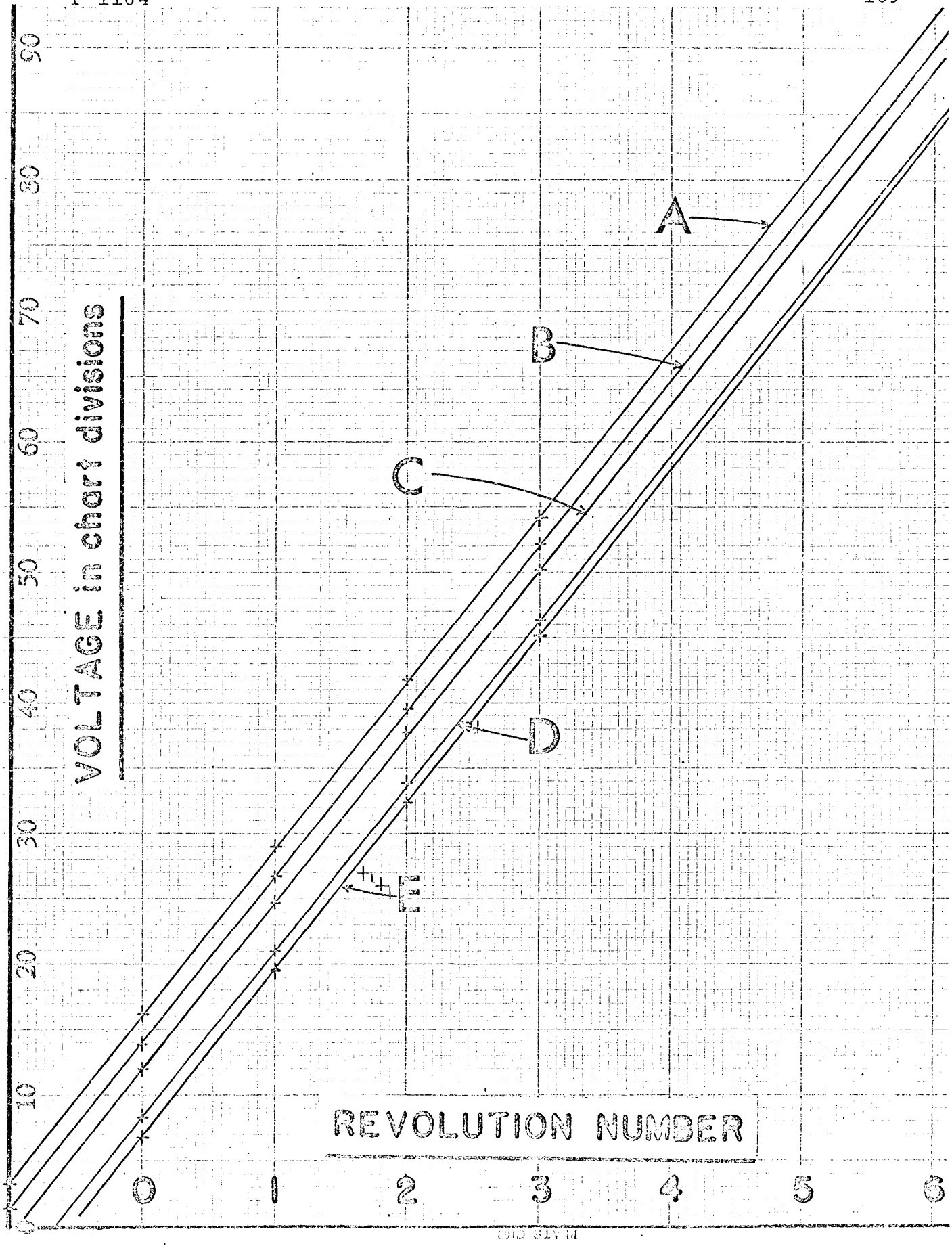

Figure 39. Graph of the Voltage vs. Revolution Number.

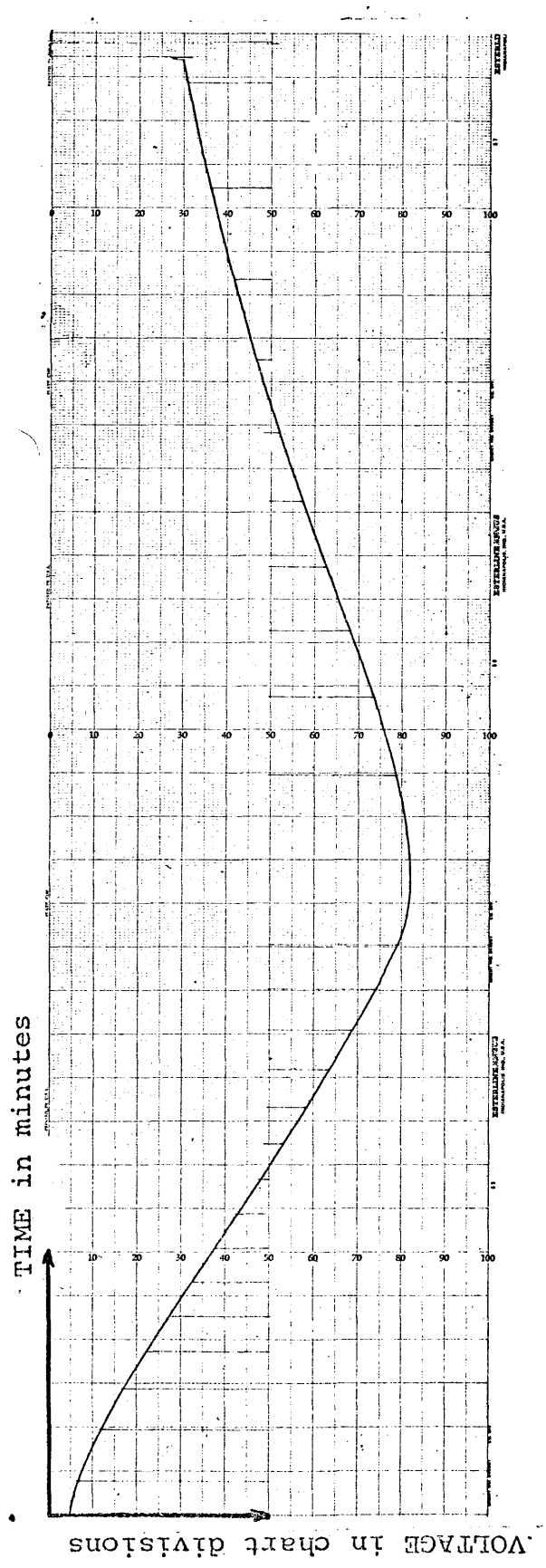

Figure 40. Typical Output Recording of the Transducer Produced by a Displacement of the Interferometer Capacitor Plate.

at each peak is plotted against the peak number (an integer) producing two straight lines: one due to the movement of the parallelogram when the steel tube is heated, and one when the tube cools. If there is no drift, the slopes of the two straight lines will be identical. The slope measured from this graph is the desired scale factor, which is in units of $\frac{1}{2}\lambda$ per unit voltage change (see fig. 42).

c-3. Sample Calculations

In this section the calibration scale factor is calibrated based on data taken from a set of transducer output recordings which have monitored both movements of the transducer and interferometer capacitor plates.

(1) Transducer Run

As noted in sec. c-2, the voltage readings at every fifth short of the output is plotted against the corresponding "Revolution number." A particular case exp $X\text{-}A_2$ is illustrated in fig. 38 from which five independent sets of data are plotted as five straight lines A, B, C, D, and E in fig. 39. The transducer scale factor, the average slope of the lines A, B, C, D, and E, is calculated. Each line is extended so that the corresponding voltage change for a scan through six revolutions is measured for each line and is enumerated in Table I. Because the full-scale voltage of

the chart recorder is not known, the average scale factor, computed in Table I, is expressed in chart div per rev.

Two additional runs of the transducer were performed where the screw moved the transducer capacitor plates in the direction opposite to that of the first run (exp X-A_2') and then back again. (Exp X-A_2"). Hence the three transducer runs were performed over approximately the same part of the screw so that one may state that all three were performed independently under similar conditions.

Table I

Computation of the Transducer Scale Factor for Exp X-A_2

Line	V_6	V_0	$\Delta V = V_6 - V_0$		
A	9.23	1.60	7.63		
B	9.00	1.40	7.60		
C	8.81	1.20	7.61		
D	8.41	0.82	7.59		
E	8.33	0.68	7.65	Avg ΔV	Avg Slope k_t
		Sum =	38.08	$\frac{\text{Sum}}{5} = 7.616$	$\frac{\Delta V}{6} = 1.269 \frac{\text{chart div}}{\text{rev}}$

From Table I the transducer scale factor k_t for exp X-A_2 is $1.269 \frac{\text{chart div}}{\text{rev}}$.

By a similar set of calculations (these are not shown),

the average scale factor for exp X-A_2' and exp X-A_2" are

$$\text{Exp X-}A_2\text{'} \qquad k_t' = 1.288 \frac{\text{chart div}}{\text{rev}}$$

$$\text{Exp X-}A_2\text{"} \qquad k_t'' = 1.297 \frac{\text{chart div}}{\text{rev}}$$

If drift is present, it must be corrected. One way of applying the drift correction would be to measure the drift slope before and after each transducer run, and then add the averaged drift slope to the slope of the transducer output. However this necessitates the additional task of determining the slope of the recorded output which is in chart div per min. Once the transducer output is corrected for drift, it would have to be converted to the desired scale factor in chart div per rev.

A second method that is recommended has the advantage of correcting for drift by operating directly on the scale factors calculated in Table I. It is recalled that in the consecutive transducer runs the screw was rotated in opposite directions. Since the average drift is the same for two consecutive runs, it will cancel out when the respective scale factors are averaged (see appendix A). However drifts should be sampled before and after each transducer run, first to check on the linearity of the drift and second to determine if the drifts differ appreciably for each transducer run. For the second case it may be desirable to apply the first

method for drift correction.

For the three transducer runs described above, the drifts were determined to be approximately zero. But using the second method for drift corrections, the averaged scale factors for the first and last pair of transducer runs are $K_1 = 1.279 \frac{\text{chart div}}{\text{rev}}$ and $K_2 = 1.293 \frac{\text{chart div}}{\text{rev}}$. Averaging these two results yields the best estimate of the transducer scale factor, $K_t = 1.286 \frac{\text{chart div}}{\text{rev}}$.

(2) Interferometer Run

In the calculation of the transducer scale factor described above, a choice existed between two methods in calculating the drift. However no such choice is available for calculating the drift during the interferometer run. Because of the difficulty in sampling drift once the interferometer is allowed to scan, one must by necessity use the results of appendix A. Equations 4a and 4b of appendix A are expressions for the transducer scale factor K_1 corrected for the average drift occurring during a complete interferometer run. These equations are repeated below.

(a) $K_1 = k + \frac{M_d}{u}$

(1)

(b) $K_1 = k' - \frac{M_d}{u'}$

k and k' are the transducer scale factors, in chart div of output per ½λ of movement, produced when the parallelogram is moved forward by the expanding tube (unprimed) and then moved backward by the contracting tube (primed).

u and u' are the velocities in ½λ per min, imparted to the parallelogram by the expansion and contraction of the steel tube respectively.

M_d is the average linear drift in chart div of output per min occurring during a complete scan of the interferometer. M_d is calculated from eq. 5 in appendix A and restated below

$$(2) \qquad M_d = \frac{(k-k')uu'}{u+u'}$$

In applying eqs. 1 and 2, k, k', u, and u' are measured from the transducer recording of the interferometer scan shown in fig. 41. k and k' are obtained by plotting the voltage positions at the superimposed wavelength peaks versus "peak number." The results of this plot are shown in fig. 42. Here two separate straight lines are plotted, one resulting from the expansion drive (fig. 41a) and one from the contraction drive (fig. 41b). The slopes k and k' measured from fig. 42 are respectively 0.520 and 0.515 chart div per ½λ. The fringe velocities u and u' are obtained by plotting peak number versus time. This graph is shown in the lower portion of the transducer records (figs. 41a and 41b). The slopes of the straight lines plotted are the velocities u = 1.177 ½λ per min and u' = 0.697 ½λ per min.

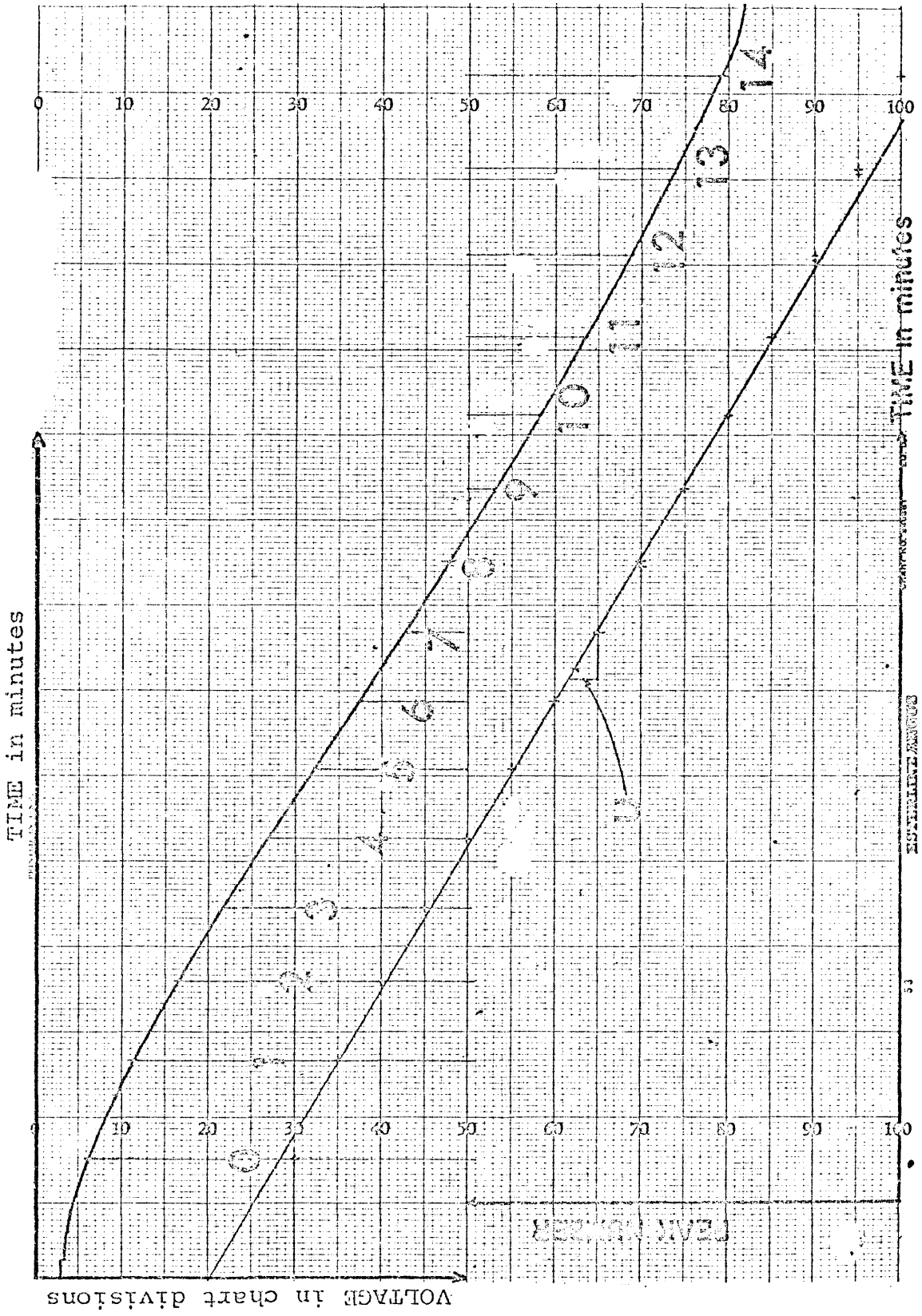

Figure 41a. Transducer Recording of the Interferometer Expansion Drive.

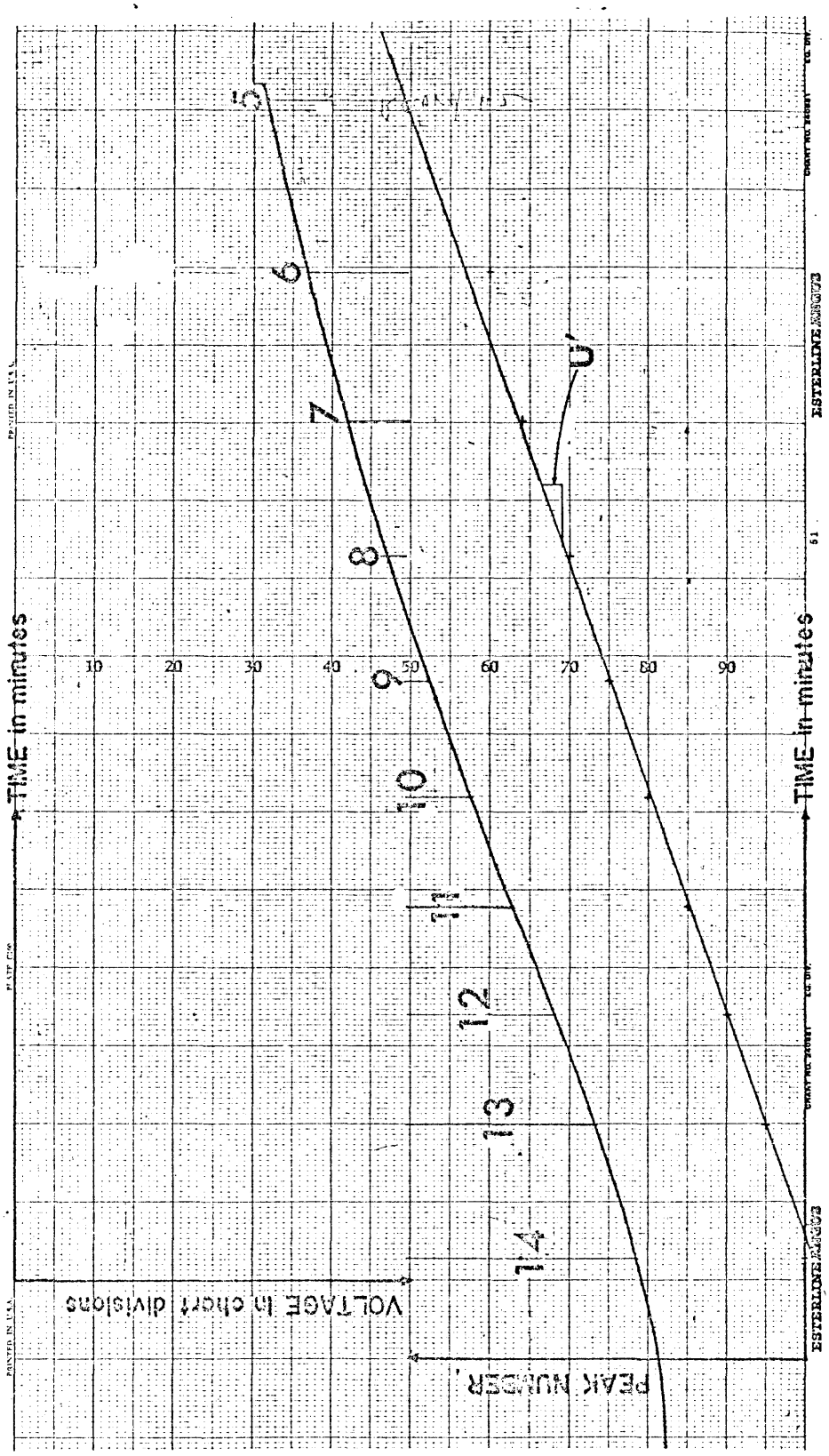

Figure 41b. Transducer Recording of the Interferometer Contraction Drive.

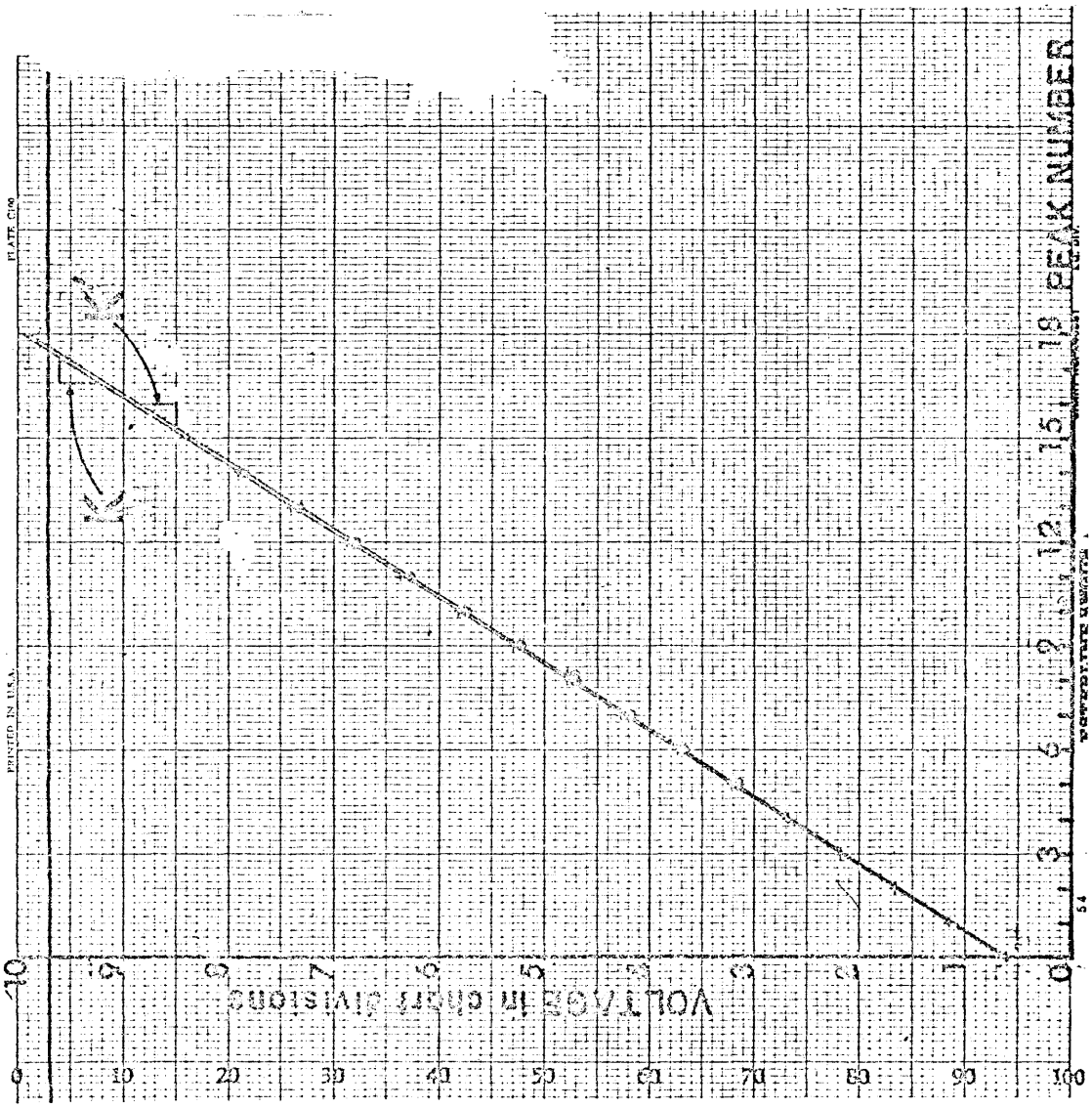

Figure 42. Graph of the Voltage vs. Peak Number.

From eq. 2 the average drift M_d is calculated.

$$M_d = (0.515 - 0.520)\ \frac{(1.177 \times 0.697)}{1.177 + 0.697}$$

$$M_d = -0.002\ \frac{\text{chart div}}{\text{min}}$$

From eq. 1 the required scale factor is computed

$$K_I = 0.520 - \frac{0.002}{1.177} = 0.518\ \frac{\text{chart div}}{\frac{1}{2}\lambda}$$

$$K_I = 0.515 + \frac{0.002}{0.697} = 0.518\ \frac{\text{chart div}}{\frac{1}{2}\lambda}$$

A second interferometer run performed under similar conditions yielded the scale factor

$$K_I' = 0.522\ \frac{\text{chart div}}{\frac{1}{2}\lambda}$$

The best estimate of the interferometer scale factor K_b is 0.520 chart div per $\frac{1}{2}\lambda$.

(3) Computation of the Calibration Scale Factor

Then using the scale factors K_t = 1.286 chart div per rev and K_b = 0.520 chart div per $\frac{1}{2}\lambda$, one may calculate the primary scale factor K in $\frac{1}{2}\lambda$ per rev,

$$K = \left(1.286\ \frac{\text{chart div}}{\text{rev}}\right)\left(\frac{1}{0.520}\ \frac{\frac{1}{2}\lambda}{\text{chart div}}\right)\left(2508\ \frac{\overset{\circ}{\text{A}}}{\frac{1}{2}\lambda}\right)$$

$$\left(10^{-8}\ \frac{\text{cm}}{\overset{\circ}{\text{A}}}\right)\left(0.3937\ \frac{\text{in.}}{\text{cm}}\right)$$

$$K = 24.4 \frac{\mu \text{ in.}}{\text{rev}}$$

or in microns

$$K = 0.620 \frac{\mu}{\text{rev}}$$

V. ERROR ANALYSIS

It is the purpose of this chapter to demonstrate that the uncertainty incurred in calibrating the strainmeter transducer will be about 1 percent. This will be shown in three parts. First the uncertainty in calculating the calibration scale factor will be determined. In the second part four systematic errors will be discussed, and their contributions to the uncertainty will be shown to be less than 1 percent. Finally in the third section it will be shown that the theoretical calculations will closely predict the form of the fringe recorded by the interferometer.

A. Recorded Uncertainty in the Calibration Scale Factor

In ch. IV, sec. c-1, it was shown that the determination of scale factor involves two sets of measurements.

(1) The screw-operated transducer produces an output measured in voltage change per screw revolution. The output is shorted five times per revolution of the

screw. The uncertainty in determining the voltage change per screw revolution depends on how precisely a revolution of the screw will be repeated. To determine this uncertainty, the screw was rotated through one revolution, and the position of the screw was read just as the transducer output was shorted. The position of the screw can be read to one part in 250 using the screw vernier scale. The uncertainty in reproducing a rotation of the screw was determined to be no worse than one part in 250. For calculation purposes a ½-percent uncertainty will be used.

(2) Simultaneous operation of the interferometer and the transducer produces a transducer record from which the scale factor in ½λ of displacement per unit voltage change is obtained. The accuracy in measuring the scale factor depends in part on how closely the time in the passage of a peak can be determined. This is a function of the recorded peak width, which is determined in the following section.

a-1. Measurement of the Recorded Peak Width

The peak width is defined as the distance in fractions of an order number between points on the fringe contour at 0.98 peak value. The peak is measured from the recording

and then converted to order number by taking the ratio of the peak width to the peak separation (distance between consecutive peaks). Unfortunately, due to the nonuniform velocity of the moving assembly of the interferometer, the recorded peaks will not be uniformly spaced nor symmetrical. Therefore an average value of the peak separation and the fringe width at 0.98 peak magnitude should be determined in order to obtain the best estimates of the peak width and the half width. Figures 40, 41, and 43 are sample records from which the scale factor and its uncertainty will be calculated. Figure 43 is a record of the interferometer scan. It is found that peaks 4 to 9 due to the "expansion drive" (expansion of the heated tube which moves the parallelogram) exhibit a velocity that is constant within 3 percent, whereas in the "contraction drive" only peaks 10 to 13 maintain a velocity that is equally constant (see Table II).

From fig. 43, fringes 5, 6, and 7 are enlarged and reproduced in fig. 44, in which sample measurements of the peak width and the peak separation are shown. Table II tabulates these measurements and the calculations evaluating the peak and half widths. All measurements are made with a Vemco ruler whose least count is 1/50 in. Measurements with this ruler are expressed in units of 0.2 in.

One may conclude from the results shown in Table II

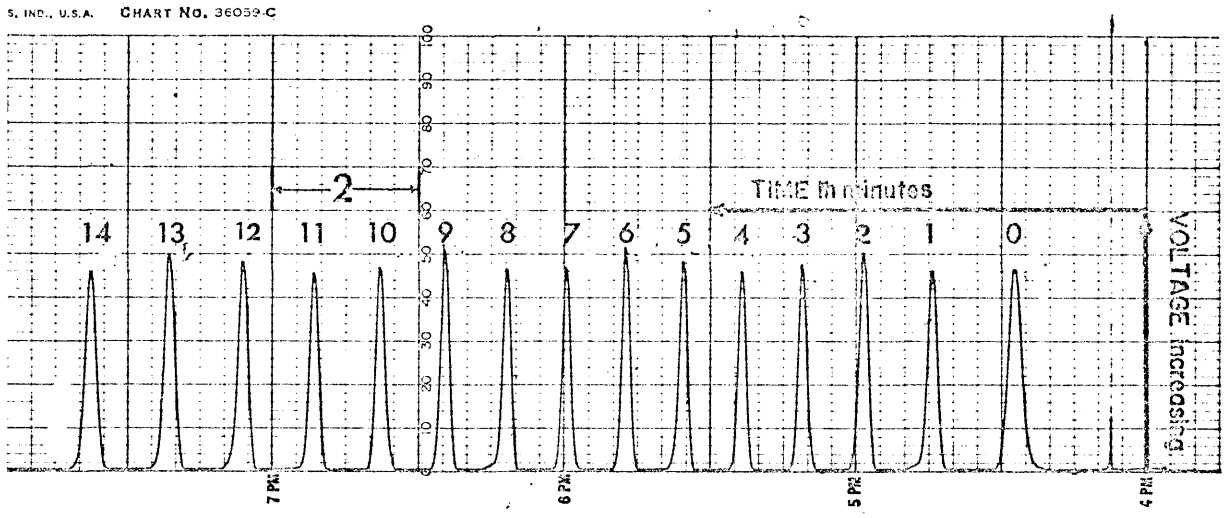

a. Expansion Drive

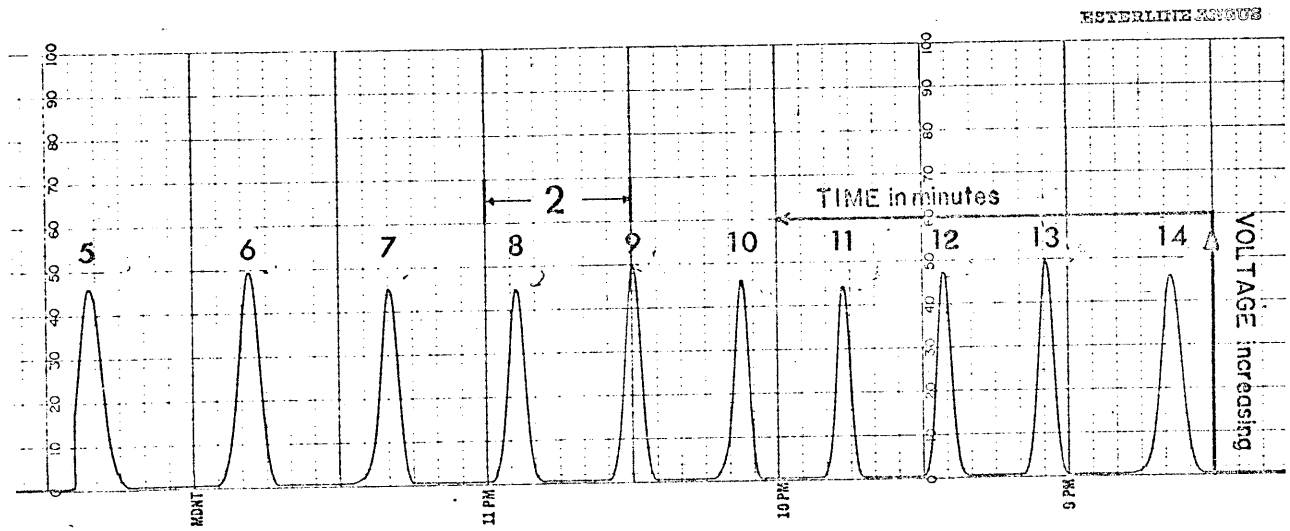

b. Contraction Drive

Figure 43. Output Recordings of the Interferometer Scan With the Bausch and Lomb Filter.

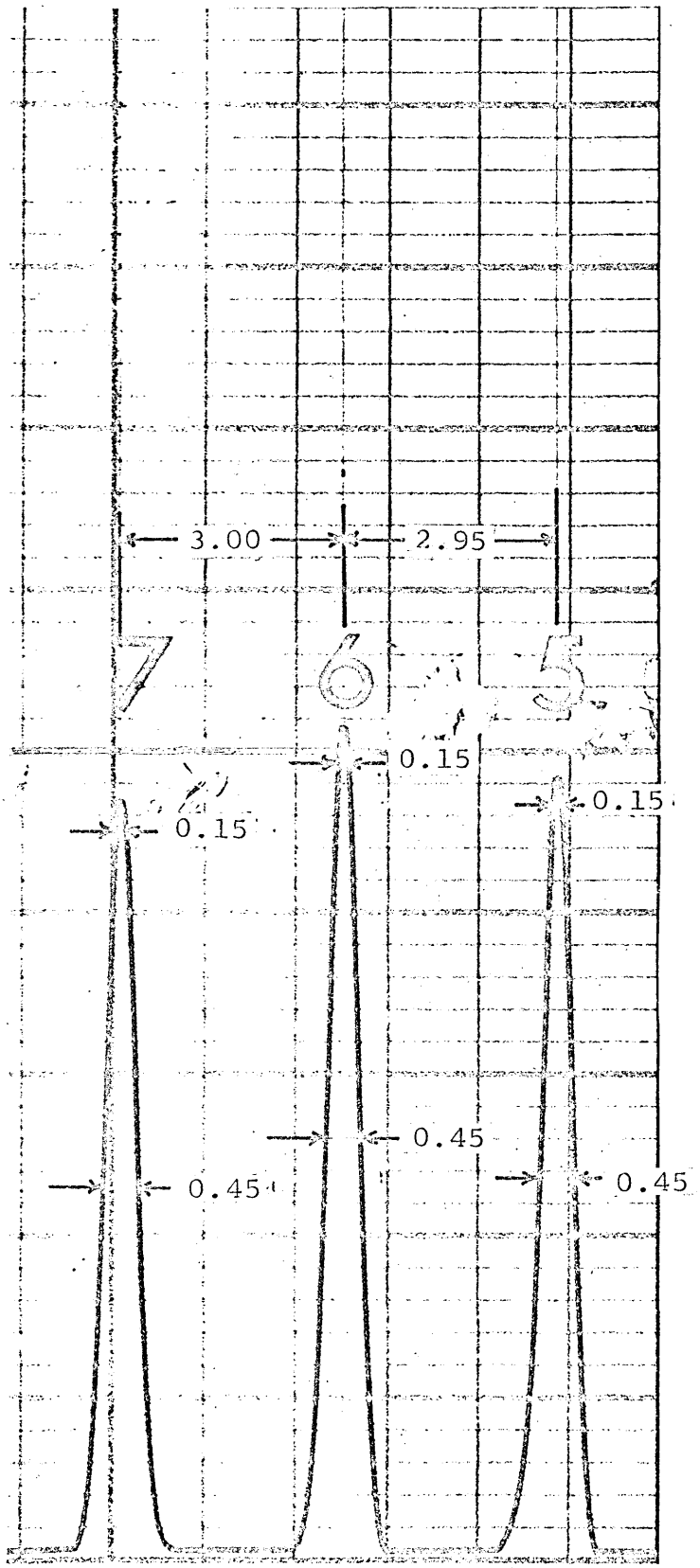

Figure 44. Sample Measurements of the Peak and Half Widths.

that broadening at the peak is about .05 order, yielding a 0.5-percent uncertainty for a scan through ten peaks. The half width shown in Table II is 0.15 order, which compares favorably with the value of 0.160 order obtained theoretically in ch. II, sec. D.

a-2. Determination of the Interferometer Scale Factor and Its Uncertainty

From ch. IV, sec. c-3, the interferometer scale factor was evaluated by plotting the peak number versus the corresponding voltage readings. In this section it will be shown that the graphical procedure is sufficiently accurate for the particular interferometer run illustrated to yield an interferometer scale factor that is accurate to about 1 percent.

In the adaptation of the least-square method to the calculation of the interferometer scale factor and its uncertainty, one recalls from the graphical procedure in ch. IV (see fig. 42) that the abscissa is composed of successive integers (peak numbers). Therefore the slope, k, of the line that best fits the empirical points is calculated from the expression

$$(1) \quad k = \frac{6}{N(N^2-1)} \{(N-1)(V_{N-1} - V_o) + (N-3)(V_{N-2} - V_2) + \ldots\}$$

where N = the total number of points

Table II

Calculation of the Peak and Half Widths

All measurements are made on a 50 division per inch scale where 10 divisions (.2 in.) = 1 scale unit. All measurements are expressed in scale units. Chart speed = 3/4 in. per min.

Expansion Drive

Peak #	Peak Position	Peak Separation	Peak Width	Half Width
4	28.45			
		3.10		
5	25.35		0.15	0.45
		3.00		
6	22.35		0.15	0.45
		2.95		
7	19.40		0.15	0.45
		3.05		
8	16.35		0.15	0.50
		3.05		
9	13.30			
		Sum=15.15	Sum=0.60	Sum=1.85
		Avg= 3.03	Avg=0.15	Avg=0.46

Contraction Drive

Peak #	Peak Position	Peak Separation	Peak Width	Half Width
10	5.60			
		5.25		
11	10.85		0.15	0.75
		5.20		
12	16.05		0.25	0.85
		5.20		
13	21.25			
		Sum=15.65	Sum=0.40	Sum=1.60
		Avg= 5.22	Avg=0.20	Avg=0.80

Table II - continued

Uniformity of the Velocity Drive

(measured in $\frac{\Delta t}{t} \times 100$ where t = time in scale units)

	Maximum Deviation in Peak Separation
Expansion Drive	$\frac{0.08}{3.03} \times 100 = 3\%$
Contraction Drive	$\frac{0.03}{5.22} \times 100 = 1\%$

The Peak and Half Widths in Fractions of an Order Number

	Expansion Drive	Contraction Drive
Peak Width	$\frac{0.15}{3.03} = 0.050$	$\frac{0.20}{5.22} = 0.038$
Half Width	$\frac{0.46}{3.03} = 0.152$	$\frac{0.80}{5.22} = 0.153$

V_p = the voltage reading of the p^{th} peak - p goes from 0 to N-1

The standard deviation in k is defined by the expression

$$(2) \quad \sigma_k = \sigma_V \left(\frac{12}{N(N-1)}\right)^{\frac{1}{2}}$$

where σ_V is the root mean square error of a single reading. This error is a function of both the uncertainty, σ_p, in locating the position of a peak and the uncertainty, σ_L, in determining the voltage which corresponds to the position of the peak that is superimposed on the transducer output (see figs. 41a and 41b).

In the first case the deviation, σ_π, in the voltage reading due to the peak width is obtained from the expression

$$(3) \quad \sigma_\pi = \sigma_p k$$

Equation 3 is the result of the relationship between the empirical points and the line of "best fit" as described in fig. 45. In the second case the uncertainty, σ_L, of the voltage position at each point, results from the transducer output being a line of finite thickness. Measurement of this thickness parallel to the voltage axis gives the result $\sigma_L = \pm$ 0.015 chart div. From sec. a-1 the peak width, $_p$, was determined to be 0.05 order. The corresponding deviation in the voltage, σ_π, due to σ_p, is calculated from eq. 3, once k is computed by the method of least squares.

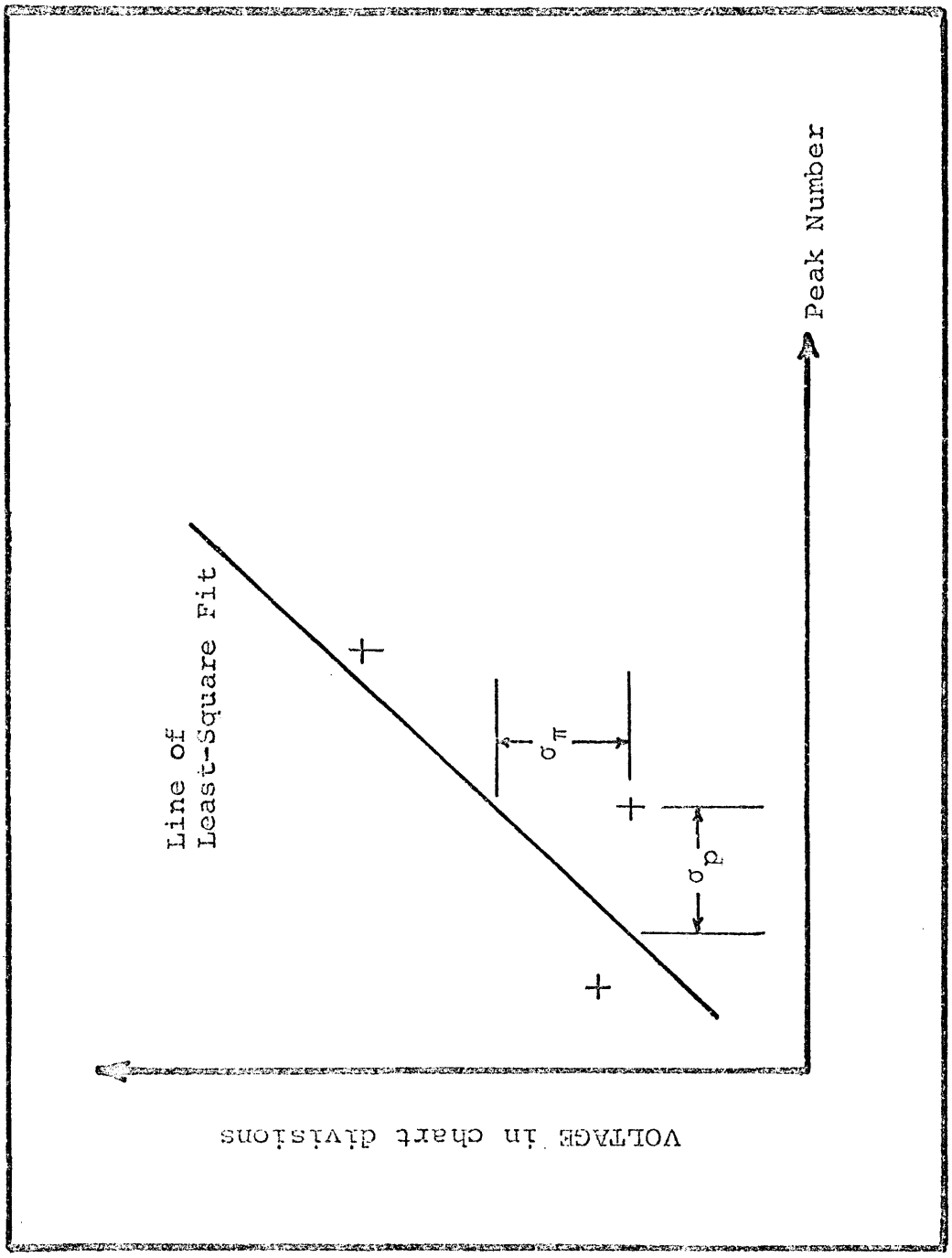

Figure 45. Geometric Relations Between the Line of Least-Square Fit and the Emperical Points.

From statistics the total uncertainty in the voltage reading may then be evaluated from the expression

$$(4) \quad \sigma_V = (\sigma_\pi^2 + \sigma_L^2)^{\frac{1}{2}}$$

Once σ_V is determined, the uncertainty in the scale factor k may be calculated from eq. 2. Sample calculations of both the slope k and of the uncertainty σ_k are shown in table III for exp X-B_2'. The data V_p in table III are read from the transducer output (figs. 41a and 41b). The slopes and the uncertainties for the expansion drive (unprimed) and the contraction drive (primed) are determined to be respectively

$$k_1 = 0.5211 \frac{\text{chart div}}{\frac{1}{2}\lambda} \qquad \sigma_k = 0.0018 \frac{\text{chart div}}{\frac{1}{2}\lambda}$$

$$\text{Relative uncertainty} = 0.34\%$$

$$k_1' = 0.5193 \frac{\text{chart div}}{\frac{1}{2}\lambda} \qquad \sigma_{k'} = 0.0033 \frac{\text{chart div}}{\frac{1}{2}\lambda}$$

$$\text{Relative uncertainty} = 0.64\%$$

A second independent interferometer run, exp X-B_1' was performed on the same transducer, X, (calculations are not shown). For this case the slopes and the uncertainties were determined to be

Table III

CALCULATION OF THE INTERFEROMETER SCALE FACTORS

AND ITS UNCERTAINTY - METHOD OF LEAST SQUARES

Uncertainties

$\sigma_L = \pm 0.015$ chart div $\quad \sigma_\pi = k\sigma_p$

$\sigma_p = 0.05$ order $\quad \sigma_V = (\sigma_\pi^2+\sigma_L^2)^{\frac{1}{2}} \quad \sigma_k = \sigma_V \left(\frac{12}{N(N^2-1)}\right)^{\frac{1}{2}}$

where N is the total number of points

The Slope of Best Fit and Its Uncertainty

$$k = \frac{6}{N(N^2-1)} \sum_p \sum_{p'} (p-p')(V_p-V_{p'}) , \quad \sigma_k = \left(\frac{12}{N(N^2-1)}\right)^{\frac{1}{2}} \sigma_V$$

where the integers p and p' are defined over specified ranges of peak number for the expansion drive and contraction drive.

Expansion Drive - N = 15

The peak number p goes from 14 to 7 while p' goes from 0 to 7.

$$k = \frac{1}{560} \{14(V_{14}-V_0)+12(V_{13}-V_1)+ \ldots\ldots + 0\} , \quad \sigma_k = 0.06\sigma_V$$

Contraction Drive - N = 10

The peak number p goes from 14 to 10 while p' goes from 5 to 9.

$$k' = \frac{1}{165} \{9(V_{14}-V_5)+7(V_{13}-V_6)+ \ldots\ldots + V_{10}-V_9\},$$

$$\sigma_k = 0.11\ \sigma_V$$

Table III - continued

Expansion Drive

p	V_p	p'	$V_{p'}$	$(V_p-V_{p'})$	(p-p')	(p-p')$(V_p-V_{p'})$
14	7.91	0	0.61	7.30	14	102.00
13	7.40	1	1.15	6.25	12	75.00
12	6.88	2	1.67	5.21	10	52.10
11	6.36	3	2.18	4.18	8	33.44
10	5.82	4	2.69	3.13	6	18.78
9	5.30	5	3.21	2.09	4	8.36
8	4.79	6	3.73	1.06	2	2.12
7	4.28	7	4.28	0.00	0	0.00
						S = 291.80

$k = \frac{S}{560} = 0.5211 \frac{\text{chart div}}{\frac{1}{2}\lambda}$ $\sigma_V = 0.030$ chart div

$\sigma_\pi = 0.05k = 0.026$ chart div $\sigma_k = 0.0018 \frac{\text{chart div}}{\frac{1}{2}\lambda}$

Contraction Drive

p	V_p	p'	$V_{p'}$	$(V_p-V_{p'})$	(p-p')	(p-p')$(V_p-V_{p'})$
14	7.85	5	3.18	4.67	9	42.03
13	7.32	6	3.69	3.63	7	25.41
12	6.80	7	4.20	2.60	5	13.00
11	6.28	8	4.71	1.57	3	4.71
10	5.73	9	5.20	0.53	1	0.53
						S' = 85.68

$k' = \frac{S'}{165} = 0.5193 \frac{\text{chart div}}{\text{rev}}$ $\sigma_V = 0.030$ chart div

$\sigma_\pi = 0.05k' = 0.026$ chart div $\sigma_{k'} = 0.0033 \frac{\text{chart div}}{\frac{1}{2}\lambda}$

$$k_1 = 0.5170 \frac{\text{chart div}}{\frac{1}{2}\lambda} \qquad \sigma_k = 0.0018 \frac{\text{chart div}}{\frac{1}{2}\lambda}$$

$$\text{Percent Relative uncertainty} = 0.35\%$$

$$k_{1'} \doteq 0.5321 \frac{\text{chart div}}{\frac{1}{2}\lambda} \qquad \sigma_k = 0.0034 \frac{\text{chart div}}{\frac{1}{2}\lambda}$$

$$\text{Percent Relative uncertainty} = 0.64\%$$

From appendix A, eq. 4 is now applied to determine the drift corrected interferometer-scale factor K. Equation 4 is restated below for convenience.

$$(5) \quad \text{(a)} \quad K = k + \frac{M_d}{u}$$

$$\text{(b)} \quad K = k - \frac{M_d}{u'}$$

where the average drift slope M_d is

$$(6) \quad M_d = (k'-k) \frac{uu'}{u+u'}$$

k and k' are the slopes calculated from the transducer record by the method of least squares

u and u' are the approximate velocities of the interferometer moving assembly in $\frac{1}{2}\lambda$/min for the expansion and contraction drive as measured from figs. 41a and 41b respectively.

In Table IV the drift correction is applied and K_1 and K_2 are calculated from the interferometer runs exp X-B'$_1$ and exp X-B$_2$' respectively. The uncertainties of K_1 and K_2 due

Table IV

THE DRIFT CORRECTED INTERFEROMETER SCALE FACTOR

$$K = k + \frac{M_d}{u}$$

$$M_d = (k'-k)\,\frac{uu'}{u+u'}$$

	$X-B_1'$	$X-B_2'$
k	0.5170	0.5211
k'	0.5321	0.5193
k'-k	0.0151	0.0018
u	1.243	1.177
u'	0.605	0.697
uu'	0.7520	0.8204
u+u'	1.848	1.874
$\frac{uu'}{u+u'}$	0.4069	0.4378
M_d	0.0061	0.0008
$\frac{M_d}{u}$	0.0050	0.0007
K	0.5220	0.5218

to the drift correction are computed in appendix B. The results are listed below:

$$\text{for exp X-B}_1\text{'} - K_1 = 0.5220 \pm 0.0040 \ \frac{\text{chart div}}{\frac{1}{2}\lambda}$$

$$\text{for exp X-B}_2\text{'} - K_2 = 0.5218 \pm 0.0040 \ \frac{\text{chart div}}{\frac{1}{2}\lambda}$$

Now turning to statistics, the best estimate of the interferometer scale factor K_1 based on the data from exps X-B_1' and exp X-B_2' is

$$(7) \quad K_I = \frac{\frac{K_1}{\sigma_1^2} + \frac{K_2}{\sigma_2^2}}{\frac{1}{\sigma_1^2} \quad \frac{1}{\sigma_2^2}}$$

and the uncertainty in this estimation is

$$(8) \quad \frac{1}{\sigma_I^2} = \frac{1}{\sigma_1^2} + \frac{1}{\sigma_2^2}$$

Using these two equations, K_I and σ_I are calculated in Table V and the accepted value of the interferometer scale factor is determined to be

$$K_I = 0.5219 \pm 0.0030 \ \frac{\text{chart div}}{\frac{1}{2}\lambda}$$

In Table VI a comparison is made between the scale factors determined graphically and the corresponding scale

Table V

CALCULATION OF THE FINAL INTERFEROMETER SCALE FACTOR AND ITS UNCERTAINTY

$$K_I = \frac{\frac{K_1}{\sigma_1^2} + \frac{K_2}{\sigma_2^2}}{\frac{1}{\sigma_1^2} + \frac{1}{\sigma_2^2}} = \frac{S_2}{S_1}$$

$$\frac{1}{\sigma_I^2} = \frac{1}{\sigma_1^2} + \frac{1}{\sigma_2^2} = S_1$$

	X-B$_1$'	X-B$_2$'
K	0.5220	0.5218
σ_K	0.0040	0.0040
σ_K^2	16×10^{-6}	16×10^{-6}
$\frac{1}{\sigma_K^2}$	6.25×10^4	6.25×10^4
$\frac{K}{\sigma_K^2}$	3.2625×10^4	3.2613×10^4

$S_1 = 12.50 \times 10^4$

$S_2 = 6.5238 \times 10^4$

$$K_I = \frac{S_2}{S_1} = 0.5219 \ \frac{\text{chart div}}{\frac{1}{2}\lambda}$$

$$\sigma_I = \left(\frac{1}{S_1}\right)^{\frac{1}{2}} = \pm 0.0030 \ \frac{\text{chart div}}{\frac{1}{2}\lambda}$$

Table VI

COMPARISON BETWEEN GRAPHICAL AND LEAST-SQUARE RESULTS

	K_1	K_2	K_I
Least Square	0.522	0.522	0.522
Relative Uncertainty	0.77%	0.77%	0.58%
Graphical	0.522	0.518	0.520
Percent Difference	0%	0.77%	0.38%

factors determined by the method of least squares. The relative uncertainties in Table VI are computed from the uncertainties calculated by the statistical method in Table V. The row labelled percent difference describes the percent difference between the graphical and least-square values. From these calculations it is seen that the worst discrepancy is in K_2, which has a maximum deviation of 1.44 percent. However the uncertainty in the final scale factor K_I when determined graphically is seen to be 0.96 percent, a result that is about 1 percent.

a-3. Determination of the Transducer Scale Factor and its Uncertainty

Corresponding to the two interferometer runs treated in sec. a-2, three separate calibration runs of the screw-operated transducer were performed under similar conditions. Figure 38 is a record of one of these calibration trials, exp X-A_2. It is observed that the output is shorted five times per revolution, and with a scan of about four revolutions, 22 data points are obtained. With this data the voltage readings at each revolution were plotted against the corresponding "revolution number" in fig. 39 (see ch. IV, sec. c-3). The results of this plot yielded five straight lines whose slopes, when averaged, produced the final form of the transducer scale factor. In this section the least-square

method is now applied to the calculation of the transducer scale factor and its uncertainty.

From these five sets of data in fig. 38 (A, B, C, D, and E), five straight lines are fitted by the least-square method. The slopes k_A, k_B, etc., and their corresponding uncertainties σ_A, σ_B, etc., are computed in Table VII by the same procedure followed in Table III in sec. a-2.

The uncertainties σ_A, σ_B, etc., depend on three quantities: the uncertainty resulting from the number of points available for constructing the line (this is determined by the least-square method); the uncertainty, σ_r, produced when a revolution of the screw is not precisely repeated; and the uncertainty σ_L, produced when the voltage at each revolution is measured from the recorded line having a finite thickness. The uncertainty, σ_L, is $\pm$ .02 chart div; and the uncertainty, σ_r, is $\pm$ 0.005 rev. The total uncertainty in measuring the voltage at each revolution is $\sigma_V = \pm (\sigma_L^2 + \sigma_\pi^2)^{\frac{1}{2}}$ where σ_π is 0.005k, k being the transducer scale factor in $\frac{\text{chart div}}{\text{rev}}$. From Table VII, σ_π computed for all five lines is 0.0064 chart div, which is considerably smaller than the uncertainty σ_L. σ_L is thus the controlling factor limiting the accuracy in the calculation of the transducer scale factor. Conversely, in the interferometer run (see Table III), it is the peak width

Table VII

CALCULATION OF THE TRANSDUCER SCALE FACTOR AND ITS UNCERTAINTY - METHOD OF LEAST SQUARES

Uncertainties

$\sigma_L = \pm 0.02$ chart div

$\sigma_r = \pm 0.005$ rev

$\sigma_\pi = k\sigma_r$

$\sigma_V = (\sigma_\pi^2 + \sigma_L^2)^{\frac{1}{2}}$

$\sigma_k = \sigma_V \left\{\frac{12}{N(N^2-1)}\right\}^{\frac{1}{2}}$

The Slope of Best Fit and its Uncertainty

When N = 5 points

$$k = \frac{1}{20} \sum_r \sum_{r'} (r-r')(V_r - V_{r'}) = \frac{1}{20} \{4(V_5 - V_1) + \ldots + 0\}$$

$\sigma_k = 0.316\ \sigma_V$

where the revolution number, r, goes from 5 to 3 and the revolution number, r', goes from 1 to 3

When N = 4 points

$$k = \frac{1}{10} \sum_r \sum_{r'} (r-r')(V_r - V_{r'}) = \frac{1}{10} \{4(V_4 - V_1) + (V_3 - V_2)\}$$

$\sigma_k = 0.447\ \sigma_V$

where the revolution number, r, goes from 4 to 3 and the revolution number, r', goes from 1 to 2.

Table VII - continued

Line	r	V_r	r'	$V_{r'}$	$V_r - V_{r'}$	r-r'	(r-r')($V_r - V_{r'}$)
A	5	5.41	1	0.33	5.08	4	20.32
	4	4.18	2	1.62	2.56	2	5.12
	3	2.90	3	2.90	0.00	0	0.00
							S_A = 25.44
							$k_A = \frac{S_A}{20} = 1.272 \frac{\text{chart div}}{\text{rev}}$
							σ_π = 0.0064 chart div
							σ_V = 0.021 chart div
							$\sigma_A = 0.0066 \frac{\text{chart div}}{\text{rev}}$
B	5	5.21	1	0.12	5.09	4	20.36
	4	3.96	2	1.39	2.57	2	5.14
	3	2.68	3	2.68	0.00	0	0.00
							S_B = 25.50
							$k_B = \frac{S_B}{20} = 1.275 \frac{\text{chart div}}{\text{rev}}$
							σ_π = 0.0064 chart div
							σ_V = 0.021 chart div
							$\sigma_B = 0.0066 \frac{\text{chart div}}{\text{rev}}$
C	4	5.01	1	1.21	3.80	3	11.40
	3	3.78	2	2.48	1.30	1	1.30
							S_C = 12.70
							$k_C = \frac{S_C}{10} = 1.270 \frac{\text{chart div}}{\text{rev}}$
							σ_π = 0.0064 chart div
							σ_V = 0.021 chart div
							$\sigma_C = 0.0093 \frac{\text{chart div}}{\text{rev}}$

Table VII - continued

Line	r	V_r	r'	$V_{r'}$	$V_r - V_{r'}$	r-r'	$(r-r')(V_r-V_{r'})$
D	4	4.63	1	0.82	3.81	3	11.43
	3	3.39	2	2.10	1.29	1	1.29
							$S_D = 12.72$
							$k_D = \frac{S_D}{10} = 1.272 \frac{\text{chart div}}{\text{rev}}$
							$\sigma_\pi = 0.0064$ chart div
							$\sigma_V = 0.021$ chart div
							$\sigma_D = 0.0093 \frac{\text{chart div}}{\text{rev}}$
E	4	4.51	1	0.68	3.83	3	11.49
	3	3.23	2	1.95	1.28	1	1.28
							$S_E = 12.77$
							$k_E = \frac{S_E}{10} = 1.277 \frac{\text{chart div}}{\text{rev}}$
							$\sigma_\pi = 0.0064$ chart div
							$\sigma_V = 0.021$ chart div
							$\sigma_E = 0.0093 \frac{\text{chart div}}{\text{rev}}$

rather than the line thickness which contributes the largest part of the uncertainty incurred in measuring the interferometer scale factor.

From the five values of k (k_A, k_B, etc.), the best estimate k_1 is derived by taking the statistical average defined below.

$$(9)\quad k_1 = \frac{\frac{K_A}{\sigma_A^2} + \frac{K_B}{\sigma_B^2} + \frac{K_C}{\sigma_C^2} + \ldots.}{\frac{1}{\sigma_A^2} \quad \frac{1}{\sigma_B^2} \quad \frac{1}{\sigma_C^2} + \ldots..}$$

where σ_A, σ_B, etc., are the uncertainties in the slopes k_A, k_B, etc.

The uncertainty in k_1 is calculated from the expression

$$(10)\quad \frac{1}{\sigma_1^2} = \frac{1}{\sigma_A^2} + \frac{1}{\sigma_B^2} + \frac{1}{\sigma_C^2} + \ldots..$$

Using eqs. 9 and 10, k_1 and σ_1 are calculated in Table VIII where

$$k_1 = 1.273 \pm .0035 \ \frac{\text{chart div}}{\text{rev}}$$

From the two other transducer runs exp X-A_2' and exp X-A_2", the corresponding transducer scale factors were computed (these computations are not shown)

$$k_2 = 1.296 \pm 0.0027 \ \frac{\text{chart div}}{\text{rev}}$$

$$k_3 = 1.295 \pm 0.0031 \ \frac{\text{chart div}}{\text{rev}}$$

The drift is eliminated by averaging the transducer scale factors of two consecutive runs (see ch. IV, sec. c-3 and appendix A). Therefore one has

Exps $X\text{-}A_2$ and $X\text{-}A_2'$ $\quad k_t = \frac{1.273 + 1.296}{2} = 1.285 \ \frac{\text{chart div}}{\text{rev}}$

Exps $X\text{-}A_2'$ and $X\text{-}A_2''$ $\quad k_t' = \frac{1.296 + 1.295}{2} = 1.296 \ \frac{\text{chart div}}{\text{rev}}$

The uncertainties in k_t and k_t' are derived from the method of propagating uncertainties in functions of two variables. For the above specific case, one has

(11a) $\quad z = x + y$

(11b) $\quad \sigma_z^2 = \sigma_x^2 + \sigma_y^2$

The uncertainties σ and σ' are computed below:

For k_t $\quad \sigma_1 = .0035$

$$\sigma = (10^{-4})(1225+729)^{\frac{1}{2}} = \pm .0044 \ \frac{\text{chart div}}{\text{rev}}$$

$\sigma_2 = .0027$

For k_t' $\quad \sigma_2 = .0027$

$$\sigma' = (10^{-4})(729+961)^{\frac{1}{2}} = .0041 \ \frac{\text{chart div}}{\text{rev}}$$

$\sigma_3 = .0031$

and therefore

$$k_t = 1.285 \pm 0.0044 \ \frac{\text{chart div}}{\text{rev}}$$

$$k_t' = 1.296 \pm 0.0041 \ \frac{\text{chart div}}{\text{rev}}$$

The best estimate of the drift-corrected slopes k_t and k_t' are obtained statistically by eqs. 9 and 10. The computations are performed in Table IX, and the best estimate is determined to be

$$K_t = 1.291 \pm 0.0030 \ \frac{\text{chart div}}{\text{rev}}$$

Table X compares the accuracy of the graphical method with that of the least-square method. The maximum uncertainty in the graphical results is 0.65 percent for K_t, a result that is less than 1 percent.

a-4. The Calibration Scale Factor and its Uncertainty

In this section the calibration scale factor, K, in microns of movement per screw revolution is calculated. From secs. a-2 and a-3, the interferometer and transducer scale factors are

$$K_I = 0.5219 \pm 0.0030 \ \frac{\text{chart div}}{\frac{1}{2}\lambda}$$

$$K_t = 1.291 \pm 0.0030 \ \frac{\text{chart div}}{\text{rev}}$$

The calibration scale factor is

$$K = \left(\frac{1}{0.5219} \ \frac{\frac{1}{2}\lambda}{\text{chart div}}\right)\left(1.291 \ \frac{\text{chart div}}{\text{rev}}\right)\left(\frac{2508\text{Å}}{\frac{1}{2}\lambda}\right)\left(10^{-8} \ \frac{\text{cm}}{\text{Å}}\right)\left(10^{4} \ \frac{\mu}{\text{cm}}\right)$$

$$K = 0.620 \ \frac{\mu}{\text{rev}}$$

Table VIII

THE CALCULATION OF THE TRANSDUCER SCALE FACTOR AND ITS UNCERTAINTY - THE STATISTICAL AVERAGE

Line	k	σ_k	σ_k^2	$\frac{1}{\sigma_k^2}$	$\frac{k}{\sigma_k^2}$
A	1.272	.0066	43.56×10^{-6}	2.296×10^{4}	2.921×10^{4}
B	1.275	.0066	43.56×10^{-6}	2.296×10^{4}	2.927×10^{4}
C	1.270	.0093	86.49×10^{-6}	1.156×10^{4}	1.468×10^{4}
D	1.272	.0093	86.49×10^{-6}	1.156×10^{4}	1.470×10^{4}
E	1.277	.0093	86.49×10^{-6}	1.156×10^{4}	1.476×10^{4}
				$S_1=8.060\times10^{4}$	$10.262\times10^{4}=S_2$

$$k_t = \frac{S_2}{S_1} = 1.273 \ \frac{\text{chart div}}{\text{rev}} \qquad \sigma_t = \left(\frac{1}{S_1}\right)^{\frac{1}{2}} = 0.0035 \ \frac{\text{chart div}}{\text{rev}}$$

Table IX

CALCULATION OF THE DRIFT CORRECTED TRANSDUCER SCALE FACTOR AND ITS UNCERTAINTY - THE STATISTICAL AVERAGE

k_{av}	σ_k	σ_k^2	$\frac{1}{\sigma_k^2}$	$\frac{k_{av}}{\sigma_k^2}$
1.296	0.0041	16.81×10^{-6}	5.943×10^{4}	7.702×10^{4}
1.285	0.0044	19.36×10^{-6}	5.165×10^{4}	6.637×10^{4}
			$S_1=11.108\times10^{4}$	$S_2=14.339\times10^{4}$

$$k_t = \frac{S_2}{S_1} = 1.291 \ \frac{\text{chart div}}{\text{rev}} \qquad \sigma_t = \frac{1}{(S_1)^{\frac{1}{2}}} = 0.0030 \ \frac{\text{chart div}}{\text{rev}}$$

Table X

COMPARISON BETWEEN THE GRAPHICAL AND LEAST-SQUARE TRANSDUCER SCALE FACTORS

	k_t	$k_{t'}$	K_t
Least Square	1.285	1.296	1.291
Relative Uncertainty	0.38%	0.31%	0.26%
Graphical	1.279	1.293	1.286
Percent Difference	0.47%	0.23%	0.39%

or $K = 24.4 \frac{\mu \text{ in.}}{\text{rev}}$

The relative uncertainty for K is calculated by the method of propagating errors, where for the quotient

$$K = \frac{K_t}{K_I},$$

one has

$$(12) \qquad \frac{\sigma_K}{K} = \pm\{(\frac{\sigma_t}{K_t})^2 + (\frac{\sigma_I}{K_I})^2\}^{\frac{1}{2}}$$

where

$$\frac{\sigma_t}{K_t} = 0.00232 \qquad (\frac{\sigma_t}{K_t})^2 = 5.40 \times 10^{-6}$$

and

$$\frac{\sigma_I}{K_I} = 0.00575 \qquad (\frac{\sigma_I}{K_I})^2 = 32.49 \times 10^{-6}$$

Finally

$$\frac{\sigma_K}{K} = \pm\ 0.006$$

Since the graphical and least-square results are identical to three significant figures, the relative uncertainty in using the graphical procedure is 0.6 percent for this particular calibration.

Then the calibration factor calculated for transducer X using a 1-percent uncertainty is

$$K = 0.620 \pm 0.006 \frac{\mu}{\text{rev}}$$

or

$$K = 24.4 \pm 0.24 \ \frac{\mu \text{ in.}}{\text{rev}}$$

The accuracy obtained in calculating the calibration scale factor graphically has been shown to be better than 1 percent. However this result is derived from one calibration, and it will surely require a check from several other calibrations before this conclusion is definitely confirmed. As of now, the requirements that the calibration be exactly 1 percent is not rigorous, so that an accuracy of perhaps 2 to 3 percent by graphical means may be acceptable. The graphical procedure is simple and rapid enough so that many people may be willing to accept its inherent lack of accuracy. However a word of caution: it was demonstrated in appendix B that the uncertainty σ_K will increase with the drift of the transducer that occurs during the interferometer run. In fact, if the difference between the scale factors k'-k goes beyond 8 percent of K_I, the conservative estimate in the accuracy of 2 to 3 percent may be wrong, and it is even recommended that the results of the calibration be rejected without further calculation.

B. Systematic Errors

In ch. II an analysis of the Fabry-Perot interferometer showed the possible existence of certain disturbing effects which would decrease the accuracy of the wavelength scale

recorded by the interferometer. Indeed, these disturbances seemed to account for a large part of the recorded peak width calculated in sec. a-1. Although this analysis served to demonstrate the capabilities of the instrument, it was incomplete since a number of conditions encountered in the actual operation of the instrument were ignored. These conditions are now considered because they might impose a large systematic error upon the calibration factor and thus degrade the 1-percent accuracy. These conditions are:

(1) The index of refraction is neither unity nor constant.

(2) The filter transmits wavelengths from other parts of the helium spectrum, e.g. 5875 $\overset{\circ}{A}$.

(3) The upper plate of the parallelogram does not move parallel with respect to the bottom plate.

(4) Motion normal to the central capacitor plate mounted on the upper plate of the parallelogram is not the same as motion of the optical flat along the optical axis.

b-1. The Index of Refraction is Not One

In the derivation of eq. 11 in ch. II, the index of refraction, n, was assumed to be exactly one. Equation 11 states that the distance represented by a scan of one order is exactly one half wavelength where

(14) $(\Delta m)\lambda = 2\Delta h$ at $\phi = 0$

If the index of refraction n is not one, the change of order number is

(15) $(\Delta m_t)\lambda = 2n\Delta h \quad \text{at } \phi = 0$

where Δm_t is the actual order change when n is not one. The error incurred in using n = 1 is then

(16) $$\frac{\Delta m_t - \Delta m}{\Delta m_t} = \frac{n-1}{n} \approx n-1$$

(n-1) is called the refractivity, and if this quantity can be shown to be less than 0.01 order, the 1-percent accuracy will be maintained.

The refractivity of air is a function of temperature, pressure, CO_2 content, and H_2O vapor content. Because the measurements of wavelengths in air has reached accuracies of one part in 10^8, then in order to determine the equivalent wavelengths in vacuo, it has become necessary to determine the index of refraction of air to the same accuracy. Several investigators have measured the refractivity of air for radiations in the infrared, visible, and ultraviolet regions. Edlén (1953, 1966) has compiled the results of these investigations, and he has developed empirical equations to calculate the refractivity of air for different wavelengths at various pressures and temperatures to one part in 10^8. Edlén shows

(17) $$(n-1)_{t,p} = \frac{p(n-1)_s}{720.775}\left\{\frac{1+p(0.817-0.0133t)\times 10^{-6}}{1+0.003661t}\right\}$$

for the temperature range from 5°C to 30°C (Edlén, 1966).

p is the air pressure in torr for the range 100 to 800 torr,

$(n-1)_s$ is the refractivity of air at standard conditions. Standard conditions are defined to include dry air with 0.03% CO_2 content at 15°C and 760 torr.

Edlén tabulates measurements of (n-1) in dry CO_2 free air at 760 torr and 15°C in the visible spectrum (1966). At about 5000 Å, (n-1) is approximately 3×10^{-4}. Referring to eq. 16 one sees that the deviation in the order measurement is approximately 3×10^{-4}. For standard air which includes 0.03% CO_2 content, Edlén (1966) states that the refractivity over that of CO_2 free air will be about $\frac{1}{2} \times 10^{-8}$, a variation that is negligible here. Therefore it will be sufficiently accurate to calculate $(n-1)_{t,p}$ under the average atmospheric conditions used to calibrate the strainmeter transducer. The average conditions under which the calibrations were performed were p = 630 torr and t = 20°C. Substitution of these values and the quantity $(n-1)_s = 3 \times 10^{-4}$ in eq. 17 yields the result in which the change of the refractivity from standard conditions to the working conditions occur in the seventh decimal place. This is also negligible.

In the above calculations $(n-1)_{t,p}$ was determined for dry air. At 20°C the vapor pressure of the water at the dew point is 17.5 torr (Sears and Zemansky, 1960, Tbl. 19-5, p. 371). Since the relative humidity in the Denver area is low (10 to 15 percent inside most buildings according to

the Denver Weather Bureau), an overestimation of the relative humidity at 30% would yield a vapor pressure for water at 5.3 torr. When compared to the total atmospheric pressure of 630 torr, the water-vapor content would constitute less than 1% of the atmosphere by volume. Edlen (1966) states that under usual lab conditions air will contain water vapor at 1 to 2 percent by volume, which will decrease $(n-1)_{t,p}$ by about 80×10^{-8} a value which is still negligible. On the days which the calibrations described here were performed, the temperature was below freezing so that the vapor pressure of water was somewhat less than the figure quoted above. Hence no significant error in the calibration will result due to the humidity.

b-2. The Index of Refraction is Not Constant

The average time elapsed in a typical calibration run is about 30 minutes. During such a run fluctuations in temperature and pressure may cause n to fluctuate. Thus an additional calculation should be made to account for changes in temperature and pressure.

From eq. 10 in ch. II, one has for the distance h between the Fabry-Perot plates

(18) $\quad m = 2hn/\lambda \qquad$ at $\phi = 0$

During an incremental displacement Δh, suppose that n changes by the amount $\Delta n_{t,p}$. The corresponding order change

Δm_n, is then

$$(19) \quad \Delta m_n = \frac{2h\Delta n_{t,p}}{\lambda_o}$$

Where $\Delta n_{t,p}$ is the change in refractive index due to fluctuations in temperature Δt and pressure Δp.

The change in refractive index due to a pressure change is obtained by calculating the refractivity for two pressures and taking the difference between the resultant refractivities. The change in refractive index for a temperature change is calculated in a similar manner.

Rewriting eq. 17 in the form

$$(20) \quad (n-1)_{t,p} = \frac{(n-1)_s}{A} p \times \frac{1+p(B-Ct)\times 10^{-6}}{1+Dt}$$

where $A = 720.775$ torr $\qquad (n-1)_s = 0.0003$

$B = 0.817 \frac{^oC}{torr} \qquad t = 20^oC$

$C = 0.0133\ torr^{-1} \qquad p = 630$ torr

$D = 0.0036610$

one may then show

$$(a) \quad \Delta(n-1)_p < \frac{(1.001)(n-1)_s}{A(1+Dt)} \Delta p$$

(21)

$$(b) \quad \Delta(n-1)_t < p\frac{(1.001)(n-1)_s}{A} \Delta t \times \frac{\frac{D\Delta t}{(1+Dt)^2}}{1+\frac{D\Delta t}{1+Dt}}$$

where $\Delta(n-1)_p$ is the variation in refractivity due to the pressure change, Δp.

$\Delta(n-1)_t$ is the variation in refractivity due to the temperature change, Δt.

By putting the quantities $(1+Dt)$ and $(1+Dt)^2$ equal to 1.001 and the quantities $1+\frac{D\Delta t}{1+Dt}$ and $\frac{p}{A}$ equal to 1, eq. 21a may be simplified. One thus has

$$(a) \quad \Delta(n-1)_p < (n-1)_s \frac{\Delta p}{A} < 5\times10^{-7}\ \Delta p\ ,$$

(22)

$$(b) \quad \Delta(n-1)_t < (n-1)_s\ D\Delta t < 12 \times 10^{-7}\ \Delta t\ .$$

Examination of several barometric records shows that the average change in pressure occurring in an hour is about 1 torr. From eq. 22a the corresponding change in refractivity, $\Delta(n-1)_p$ is 5×10^{-7}.

A variation in temperature has a large effect on the order shift, Δm_n. For example with a $5^{\circ}C$ change, the variation in refractivity, $\Delta(n-1)_t$ will be 60×10^{-7} which shifts the fringe peak by about 0.04 order (as computed from eq. 19). Adding this order shift to a peak width of 0.05 order calculated in sec. a-1, the total uncertainty would then be about 0.09 order. In a ten-order scan with the interferometer, the relative uncertainty would then be about 1 percent. However the temperature change was measured under essentially the same conditions occurring during a calibration run, and it was found to be about $0.1^{\circ}C$. With the effect of the pressure change included (eq. 22a), the resultant total-refractivity

change is about 6×10^{-7} which produces an order shift, Δm_n, of about 0.004 order. Thus the order change due to fluctuations in temperature and pressure is small enough so that the 1-percent calibration will not be considerably affected.

b-3. Transmission of Other Wavelengths of the Helium Spectrum

Figure 43, the recording of the interferometer output, shows a variation in the peak height which results from the leakage of the 4470 Å and 5875 Å wavelengths through the Bausch and Lomb filter. Superposition of their fringes with those of the 5016 Å line indicated the possibility that the peak of the resultant fringe would be deformed so that the uncertainty in locating the peak might be greater than 0.01 order. However the analysis in appendix C shows that the peak is shifted by maximum amount of 0.002 order.

The 4470 Å and 5875 Å lines are transmitted at about $\frac{1}{10}$ the intensity of the 5016 Å line. In this section the 5016 Å line will be known as the "measuring fringe," and the fringes resulting from wavelengths transmitted from other parts of the helium spectrum will be called "contaminating fringes" or "contaminants." When the "measuring fringes" and the "contaminating fringes" overlap, the resulting

fringe contour will in general be asymmetrical, and its amplitude will be increased. If the peaks superimpose so that they coincide, symmetry will be maintained, and there will be no error. However when an asymmetrical contour occurs, the recorded fringe will be displaced from its theoretical position, and the peak will be broadened. Consequently the linearity and the accuracy of the wavelength scale will be degraded.

The peak offset and peak broadening may be determined by superimposing the "measuring fringe" with a fringe at $\frac{1}{10}$ the peak value. This has been done (see appendix C), and the results are plotted in fig. 46. The resultant fringes are plotted for four different positions of the "contaminating peak" measured along the abscissa from the peak position of the "measuring fringe" (see also fig. 53). In particular the "contaminating peak" has been placed at points on the abscissa where the corresponding y-coordinates on the "measuring fringe" contour are $0.95I_o$, $0.90I_o$, $0.80I_o$, and $0.70I_o$. Examination of each of the resultant peaks in fig. 46 shows that the maximum displacement of the peak is about 0.002 order, and the peak broadening is about 0.001 order.

b-4. Rotation of the Moving Flat

Although it was demonstrated in sec. b-3 that the use of the Bausch and Lomb filter would not introduce any

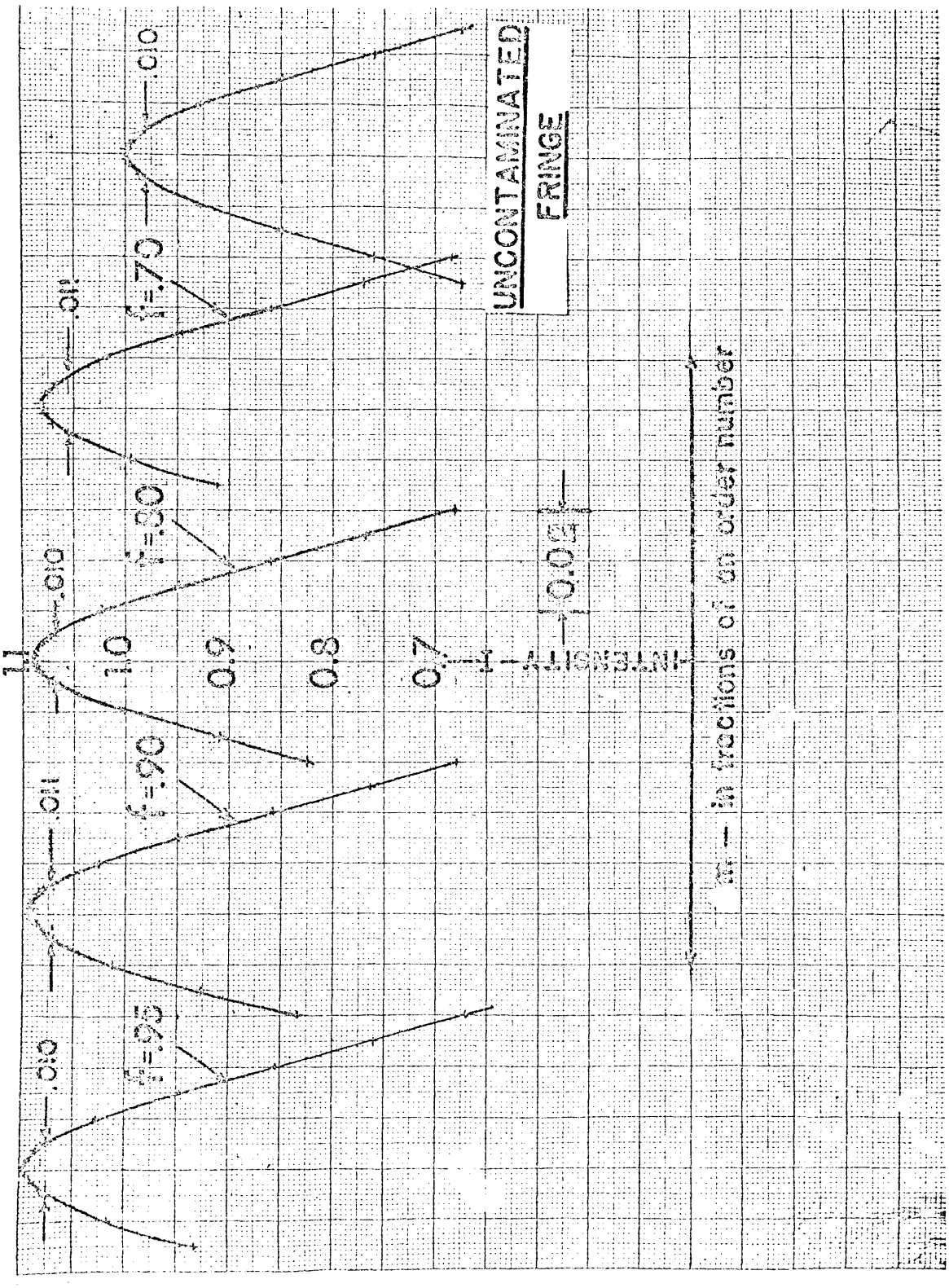

Figure 46. Asymmetry of the Resultant Fringes due to the Superposition of the "Measuring" and "Contaminating" Fringes.

significant systematic error in the recorded accuracy of the calibration, yet one finds a serious drawback inherent in its use. The variation in peak intensity may mask any loss of parallelism as the upper plate of the parallelogram is moved. For example fig. 47 shows a 6-percent loss in peak intensity for a scan through nine peaks when the spectrum systems filter is used (see ch. III, sec. b-1). Reduction in peak height to 10 percent has been recorded in a typical calibration run. A direct check of the parallelism between the flats (see chapter IV, sec. a-4) immediately following the calibration run clearly indicated that the flats were no longer parallel.

The reduction in peak height as the interferometer scans is an index of the angle which the movable flat rotates through as it is moved. To determine the peak width resulting from this loss of parallelism, it is necessary to convolve the Parallelism Function $D_p(m,b)$ (eq. 25 in ch. II) with the Airy Function for several half widths, b, in order to associate the reduction in peak height with fringe broadening. For this convolution the coefficient $\frac{S}{\pi C}$ is now computed whereas in sec. d-2 of ch. II the same convolution was performed, except that the peak height was normalized to one.

A computer program designed by Mr. Russell Gray was used to compute points on the fringe contours of each

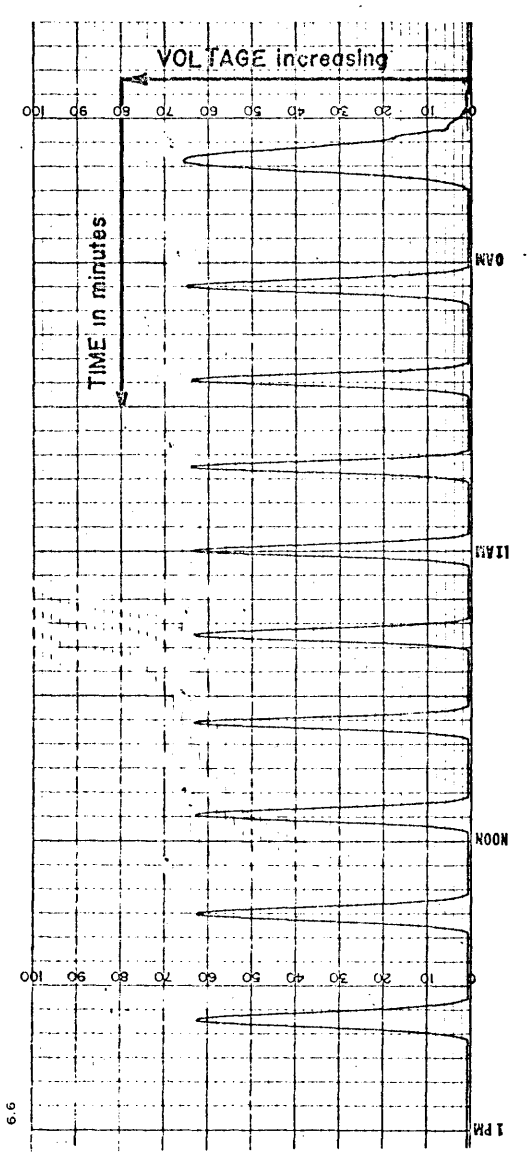

Figure 47. Output Recording of the Interferometer Scan With the Spectrum Systems Filter.

Parallelism Function, $D_p(m,b)$, corresponding to the range of half widths from b =0.044 to 0.070 order. The results of this operation are displayed in fig. 48. The peak magnitude of $D_p(m,0.044)$ has been normalized to one. The other fringes have peak heights equal to the ratio of their actual peak magnitude $(\frac{4S}{\pi C})$ to the peak magnitude of $D_p(m,0.044)$.

When the flats are not parallel, one may suppose they form a triangle with the fixed flat perpendicular to the optical axis. Deviation of the flats from parallelism is then measured as the horizontal component, c (the component parallel to the optical axis), of the side of the triangle opposite the wedge angle α (see fig. 10a). For example at b = 0.070 order, the "horizontal" deviation c is $\frac{4}{100}\lambda$ and the wedge angle between the 1-in.-diam flats is about 0.18 arc sec. If the flats were originally adjusted within the flatness tolerance, the wedge angle α would have been 0.09 arc sec. A 12-percent loss of intensity (see fig. 48) corresponds to a broadening of the half width from 0.04 order to 0.070 order. This is equivalent to the optical flat rotating through an angle of 0.09 arc sec as it is being moved.

The Instrumental Function was next produced from the convolution of the Parallelism Function, $D_p(m,0.070)$, with the other Disturbance Functions. The Instrumental Function

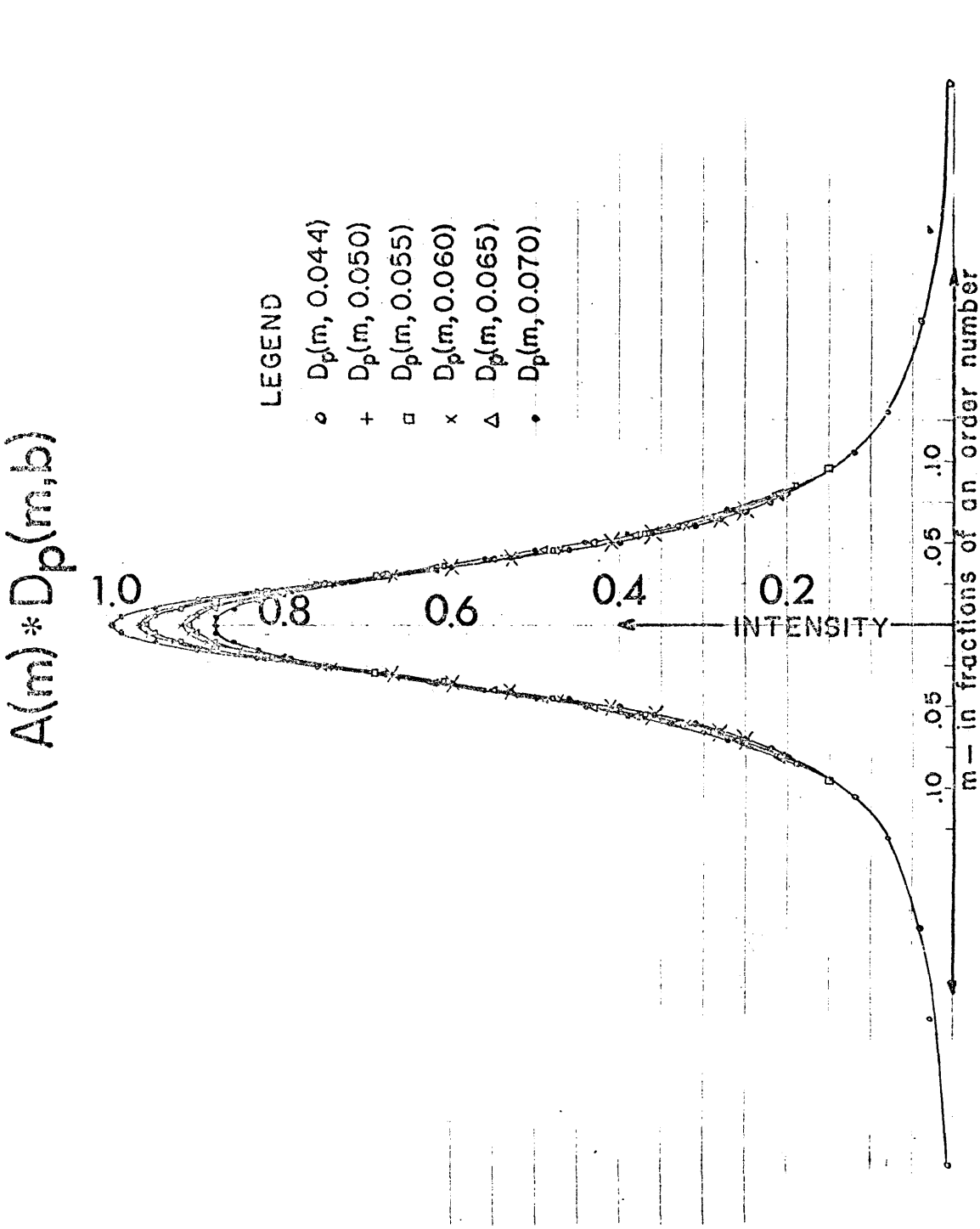

Figure 48. Decrease in Peak Height of the Parallelism Function Due to a Rotation of the Optical Flat.

is plotted in fig. 49, and the peak and half widths are determined to be respectively 0.03 order and 0.164 order. Consequently the loss of accuracy to be anticipated when a 12-percent drop in intensity occurs will be small. Furthermore in all calibration runs performed with the Bausch and Lomb filter, only those runs were accepted in which a visual check of the central zone showed that the parallelism of the plates was close to the flatness tolerance of the plates. Hence one may assume that in all calibration runs that were accepted, the deviation from parallelism was less than $\frac{4}{100}\lambda$. Thus this systematic error has a negligible effect on the 1-percent accuracy of the calibration computed in sec. A of this chapter.

b-5. Displacements of the Fabry-Perot Plates and the Central Capacitor Plates are not the Same

The movement of one of the optical flats along the optical axis as measured by the order scan of the interferometer may not be the same as the movement measured by the strainmeter transducer. The interferometer plate and the central capacitor plate are mounted and adjusted independently on the upper plate of the parallelogram. Thus the interferometer and capacitor plates may not be parallel, and therefore the component of the movement of the parallelogram normal to either element will not be identical

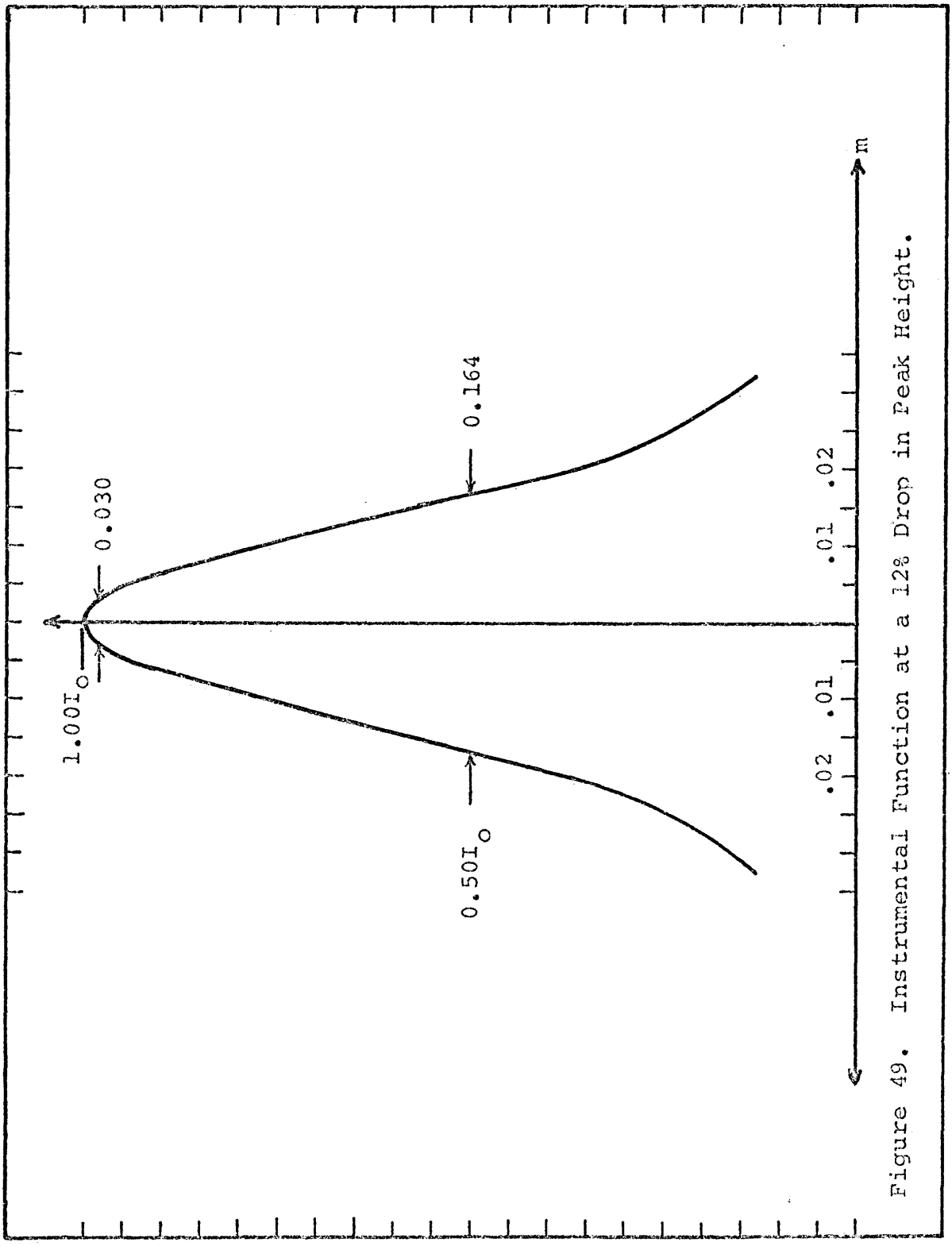

Figure 49. Instrumental Function at a 12% Drop in Peak Height.

(see fig. 50).

Suppose that the normals to the plates fail to coincide and differ in direction by the angle θ. Let Δh_o be the distance moved by the optical flat along the optical axis and let Δh be the corresponding movement normal to the capacitor plate.

From fig. 50 the actual motion of the capacitor plate will be

$$\Delta h = \Delta h_o \mathrm{Cos}\theta$$

The relative uncertainty in the movement of the capacitor plate is

$$\frac{\Delta h_o - \Delta h}{\Delta h_o} = \frac{\Delta h_o (1-\mathrm{Cos}\theta)}{\Delta h_o}$$

For a 1-percent uncertainty this requires

$$1-\mathrm{Cos}\theta < 0.01$$

$$\mathrm{Cos}\theta > 0.99$$

$$\theta < 8.1^{\circ}$$

Visual comparison of the interferometer and capacitor plates shows that the angle of deviation is less than 8°. Therefore the resulting uncertainty will be less than 1-percent.

b-6. Transducer Capacitor Plates are not Parallel

If the three capacitor plates of the transducer are not parallel, two undesirable effects might result:

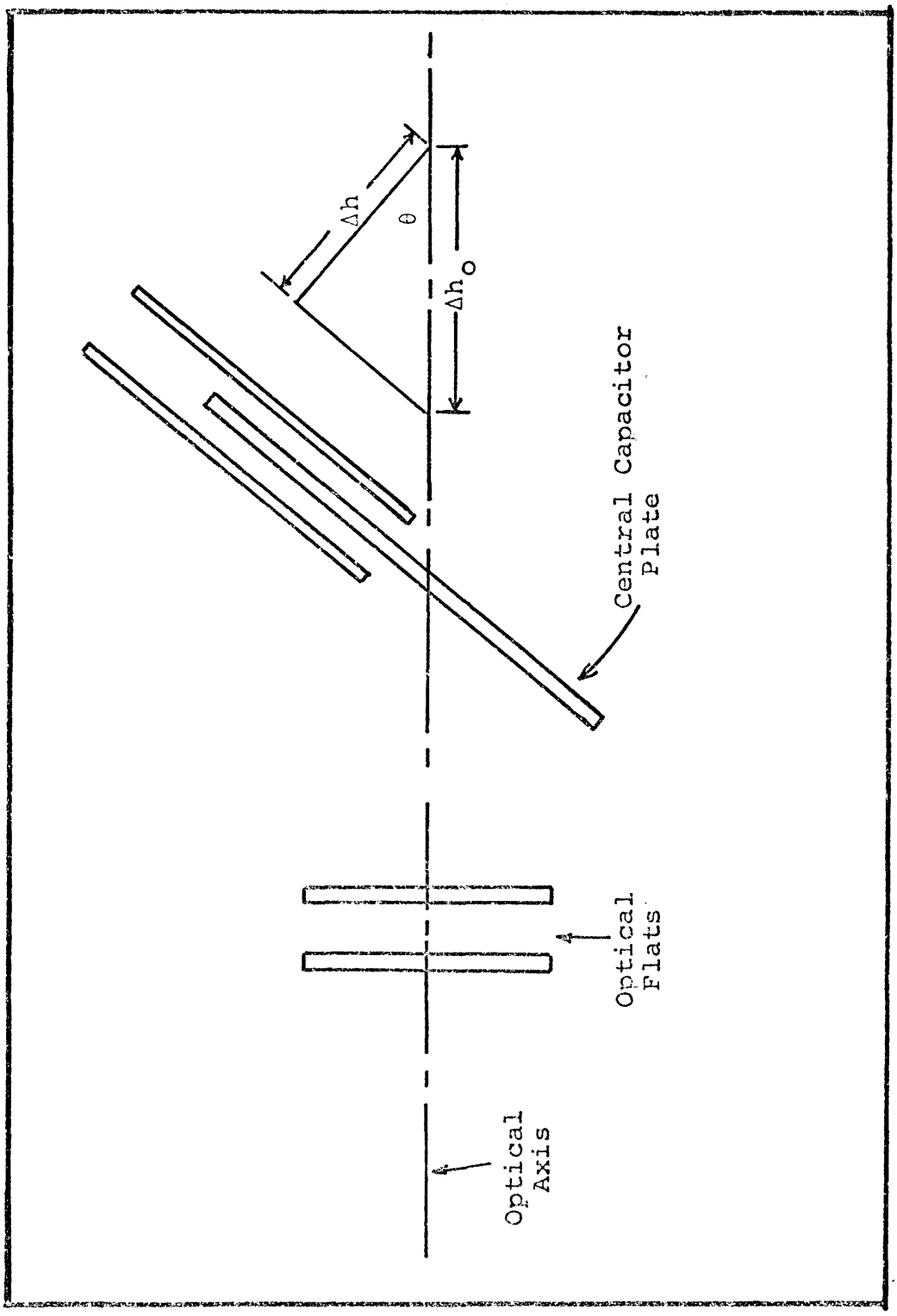

Figure 50. Details of the Central Capacitor Plate Movement With Respect to the Fabry-Perot Plate Movement.

1) The voltage change might not be a linear function of the displacement of the central capacitor plate. However according to Romig (private communication, 1967), proper adjustment of the detection circuit will make the relationship linear even when the plates are not exactly parallel. Figures 39 and 42 show that the voltage is indeed a linear function of the displacement of the central capacitor plate despite the fact that the alignment of the central capacitor plate was not extremely precise.

2) A change in the voltage sensitivity of the transducer would occur if the central plate were tilted with respect to the outer plates, thus nullifying the calibration. However since the electronic detection system is only an intermediate between the interferometer and the displacement transducer, a change in the voltage sensitivity will not affect the results because the sensitivity is stable during a calibration run.

C. Comparison Between the Recorded and Instrumental Fringes

In sec. b-4 the contour of the Instrumental Function at 12-percent intensity loss was calculated (see fig. 49) in an

attempt to predict the actual fringe to be recorded by the interferometer. This theoretical result is now compared with a recorded fringe obtained when the Spectrum Systems filter was used. The recorded fringe was enlarged by use of a Gerber scale and plotted with the theoretical fringe (see fig. 51).

With only the peaks of the fringes made to coincide, the fringes are seen to merge above the magnitude at one half the peak amplitude. Otherwise the recorded fringe is narrower than that predicted by theory. Because of the similarity in shape between the recorded and predicted peaks, one may reasonably conclude that the theoretical approach presented in chs. II and V, may be used successfully to predict the recorded uncertainty of the wavelength scale.

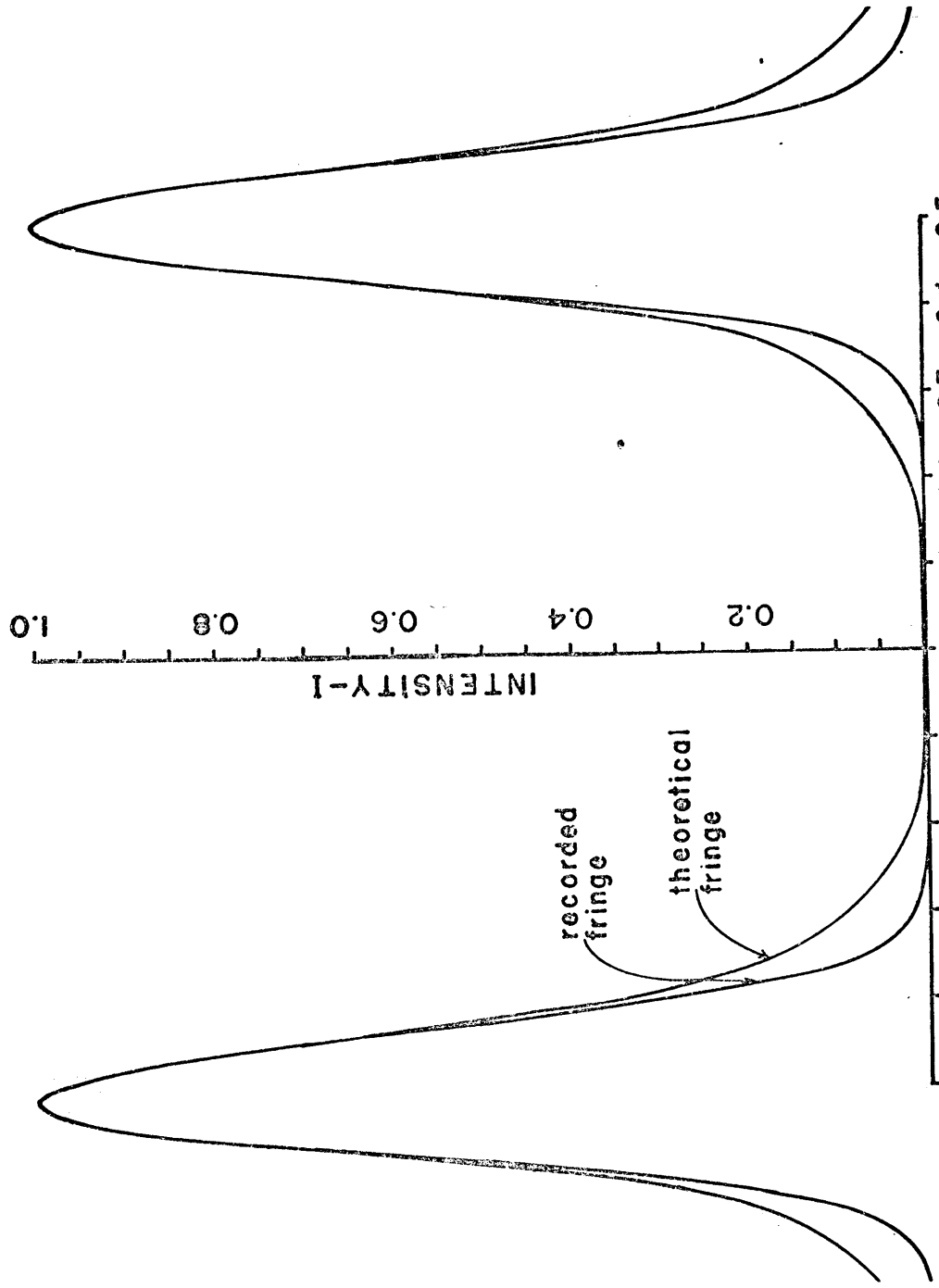

Figure 51. Comparison Between the Recorded and Theoretical Fringes.

VI. RECOMMENDATIONS AND CONCLUSIONS

Experience with the interferometer has suggested some recommendations for its improvement. For example the instrument described above is a laboratory calibration device. To be ideal for field use it would have to be more compact and stable.

The size of the interferometer is limited by the need to transmit sufficient intensity to the photodetection system. For example if smaller optical flats are used, the mounts holding the flats could be made smaller, reducing the size of the parallelogram. However the smaller plates would diminish the intensity passing through the interferometer. Certainly a more intense source would solve this problem, but unfortunately the Doppler width is usually larger for more intense sources. If the present source is kept, the spacing between the plates could be reduced so that a larger pinhole could be used. In the design of the mount for the optical flats, the brass

jacket (ch. III, sec. c-1) puts a limit on the minimum spacing that can be obtained between the plates. Thus this mount must be redesigned.

Another approach is to use a more stable moving mechanical element. If the present parallelogram device should be kept, an obvious way of improving its stability is to mill it out of one piece of metal. As remarked in ch. I, other devices have been developed to produce parallel motion. Slater (1964) in his introduction lists several mechanical scanning Fabry-Perot interferometers, which upon further investigation may prove to be preferable to the parallelogram device.

This interferometer has several features which make it attractive as the primary calibration device of the strainmeter transducer. For example with the photomultiplier tube, one may determine a $\lambda/2$ displacement of the plate directly from the chart when the interferometer scans through one peak. Thus one can avoid the inconvenience of the photographic technique, which involves long, tedious measurements and calculations. The calibration is independent of long-term changes in the variable transducer capacitance and its associated electronics. The expense of setting up many interferometric calibration systems is avoided by calibrating the displacement transducer (Romig,

1967) for each strainmeter with only one interferometer. Finally the accuracy of the wavelength scale can be improved considerably through certain modifications applied to the interferometer. These modifications were determined from the extensive error analysis developed in chs. II and V. It has been shown that most of the disturbances affecting the accuracy of the wavelength scale produces broadening of the transmitted fringes. Below is a list of these broadening effects and the modifications required to reduce these effects.

(1) Pinhole - Broadening is reduced by using a smaller pinhole and decreasing the interplate spacing.

(2) Reflection coefficient - Reflection coefficients approaching one will reduce peak broadening.

(3) Geometry of the optical flats - Optical flats plane to $\lambda/100$ or better will reduce peak broadening.

(4) Rotation of the moving flat - The mechanical scanning element should be more compact and stable as described in the earlier part of this chapter.

(5) Light source - A light source having a narrower line should be used, i.e., 5470 $\mathring{A}$ of Hg_{198}, or the light source should be cooled in order to reduce the Doppler width.

The pinhole, reflection coefficient, and the light source contribute more than 90 percent of the fringe broadening. Since 3 and 4 contribute very little to the broadening, they need not be considered further. The effect of the source which adds substantially to the fringe broadening will be costly to reduce because of the expense in purchasing a

Hg_{198} source or in cooling the present source. Reduction of the Airy width requires reflection films having higher reflection coefficients. If metal films are used, absorption of the incident intensity will be increased. If dielectric films are used, the drawback here will be the great expense in their purchase. Because reduction of broadening by minimizing the pinhole effect is by far the cheapest in both time and money, this route is recommended.

Another important result that comes out of the error analysis (ch. V, sec. b-2) is that, during the calibration run, a $5^{\circ}C$ change in temperature will shift the fringe peak by the maximum amount that can be tolerated if the interferometer is to calibrate the strainmeter transducer with an uncertainty of 1 percent. Although such a temperature change is extreme, it does underline the fact that the 1-percent calibration is near the limit in accuracy one can expect from the present instrument. However the interferometer can be made less sensitive to variations in refractive index due to pressure and temperature fluctuations by decreasing the spacing, h, between the Fabry-Perot plates (see eq. 19, ch. V), which would entail the slight redesign of the interferometer as noted in the beginning of this chapter.

The theoretical estimation of the peak broadening agrees well with that recorded by the interferometer, therefore one can predict the uncertainty in the wavelength scale. Finally it has been demonstrated that this variable spacing Fabry-Perot interferometer can calibrate a strainmeter transducer to about 1 percent in terms of the fundamental wavelength standard.

APPENDIX A

DRIFT CORRECTIONS

In this section a general formula is developed for drift corrections to be applied to the transducer output when disturbances, e.g. thermal, are superimposed on the measuring signal emanating from either a movement of the transducer capacitor plates or a movement of the interferometer capacitor plate. The justification for this derivation is based on the inability to sample drift readily during the interferometer run because of the uncontrollability of the driving mechanism, once it is activated. However runs have been made with all elements of the interferometer system in operation except that of the heating element. It was observed that the resulting drift tended to be small and linear. With the heating element in operation, any drift present during an interferometer run was therefore assumed to be linear. In the analysis below it will be demonstrated how empirical data can be used to calculate the average drift during an interferometer run. The formulas

developed below may also be applied to correcting the drift of the transducer output monitoring the voltage change per screw revolution. Figure 52 is a diagram of the transducer output obtained when the interferometer is allowed to scan.

In the following derivation the assumptions made are:

(1) The recorded output is linear.

(2) The drift is constant and linear throughout the calibration run.

(3) The interferometer scale factor, in half wavelengths per voltage change, is identical whether the parallelogram moves in one or the opposite direction.

(4) Because the heating and the cooling of the driving element occurs at different time rates, the slopes of the recorded outputs due to expansion and contraction of the driving element will not be equal.

(5) Nomenclature

M_d = Slope of the drift curve in voltage change per minute

k = Slope of the transducer output due to the expansion drive before correction for drift. The slope is expressed in units of voltage change per minute.

$$(\frac{dV}{dt})$$

k' = Slope of the transducer output due to the contraction before correction for drift

$$(\frac{dV'}{dt})$$

k_c = Drift corrected slope of the transducer output due to the expansion drive

$$(\frac{dV_c}{dt}).$$

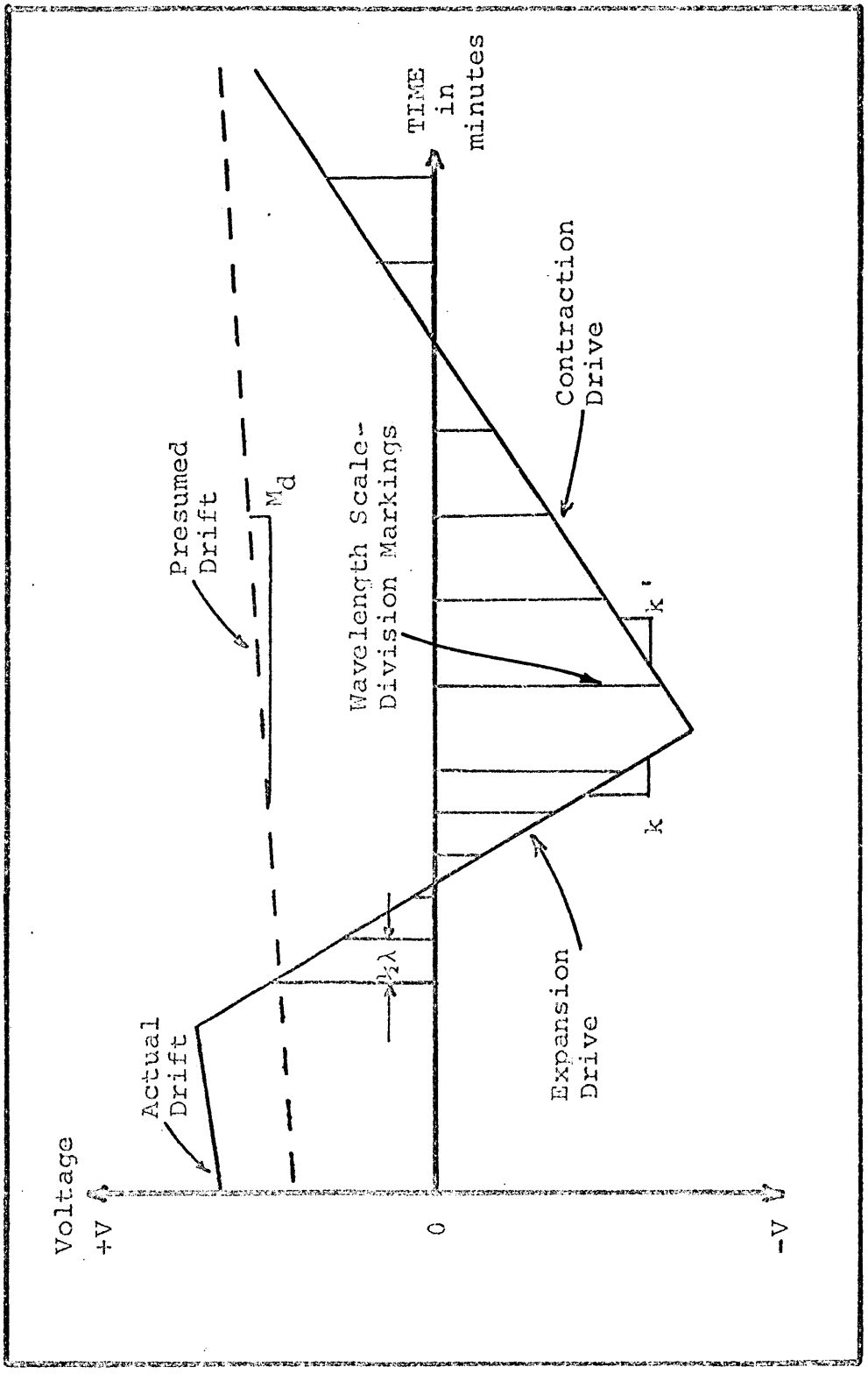

Figure 52. Drawing of the Transducer Output Produced by a Displacement of the Interferometer Capacitor Plate.

k_c' = Drift corrected slope of the transducer output due to the contraction drive $(\frac{dV_c'}{dt})$.

$u = \frac{dm}{dt}$, the velocity of the interferometer due to the expansion drive.

$u' = \frac{dm'}{dt}$, the velocity of the interferometer due to the contraction drive.

K = The desired interferometer scale factor $(\frac{dV_c}{dm})$

To obtain the outputs, k_c and k_c', one corrects the recorded signal output for drift

(a) $k_c = k + M_d$

(1)

(b) $k_c' = k' - M_d$

The calibration factor $K = \frac{dV_c}{dm} = \frac{dV_c'}{dm}$ is then obtained by noting that

(a) $k_c = \frac{dV_c}{dt} = \frac{dV_c}{dm}\frac{dm}{dt} = Ku$

(2)

(b) $k_{c'} = \frac{dV_c'}{dt} = \frac{dV_c'}{dm}\frac{dm'}{dt} = Ku'$

similarly

$$(a) \quad k = \frac{dV}{dm}\,\frac{dm}{dt} = -\frac{dV}{dm}u \tag{3}$$

$$(b) \quad k' = \frac{dV'}{dm}\,\frac{dm'}{dt} = \frac{(dV)}{dm}u'$$

Combining eqs. 2 and 3 with 1

$$(a) \quad K = \frac{dV}{dm} + \frac{M_d}{u} \tag{4}$$

$$(b) \quad K = \frac{dV'}{dm} - \frac{M_d}{u'}$$

To evaluate the linear drift, M_d, one equates 4a to 4b, whence

$$M_d = \left(\frac{dV'}{dm} - \frac{dV}{dm}\right)\frac{(uu')}{u + u'} \tag{5}$$

where u, u', $\frac{dV'}{dm}$ and $\frac{dV}{dm}$ are obtained empirically from the interferometer recordings in figs. 41a and 41b. Finally with M_d determined one can evaluate K from either eq. 4a or eq. 4b.

Equations 4a and 4b can be directly applied in correcting the drift of the screw driven transducer output. For this particular case the velocities u and u' (in $\frac{rev}{min}$) provided by the screw are equal. Then the addition of eqs. 4a and 4b cancels out the effect of the average drift and one obtains

$$K = \tfrac{1}{2}\left(\frac{dV}{dm} + \frac{dV'}{dm}\right) \tag{6}$$

APPENDIX B

THE UNCERTAINTY IN THE DRIFT CORRECTED SCALE FACTOR K

In ch. V the operation of the calibration system was described. The interferometer was allowed to scan forward with a velocity, u, and return with a velocity, u'. The interferometer scale factors k and k' and their corresponding uncertainties σ_k and $\sigma_{k'}$ were computed by the method of least squares. Application of the drift correction M_d to k and k' yields the final scale factor K as shown in appendix A. The uncertainty in K, σ_K, depends on the uncertainties σ_k, $\sigma_{k'}$, and σ_d. The quantity σ_d is the uncertainty in calculating the drift correction, and it contributes a significant amount to the final uncertainty σ_K.

From appendix A eqs. 4 and 5, the corrected scale factors due to the drift corrections are

$$(a) \quad K = k + \frac{M_d}{u} \tag{1}$$

$$(b) \quad K = k' - \frac{M_d}{u'}$$

The drift slope is

$$(2) \quad M_d = (k' - k) \frac{uu'}{u+u'}$$

The uncertainties of a function made up of several variables with known uncertainties may be determined by the method of propagating errors through the function. In computing σ_K, two types of functions will be handled.

(a) $z = x + y$

(3) whose uncertainty is

(b) $\sigma_z^2 = \sigma_x^2 + \sigma_y^2$

and

(a) $z = xy$

(4) whose uncertainty is

(b) $\frac{\sigma_z^2}{z^2} = \frac{\sigma_x^2}{x^2} + \frac{\sigma_y^2}{y^2}$

From the functions listed below, the uncertainty, σ_K, as a function of σ_k, σ_d, σ_u, and $\sigma_{u'}$, will be determined.

Let

(a) $z_1 = uu'$

(b) $z_2 = u+u'$

(6) (c) $z_3 = \frac{z_1}{z_2}$

(d) $z_4 = k'-k$

(e) $z_5 = \frac{M_d}{u}$

From eq. 2 the drift slope is

$$(a) \quad M_d = z_4 z_3$$

(7) and from eq. 1a the scale factor is

$$(b) \quad K = k + z_5$$

The corresponding uncertainties are

$$(a) \quad \sigma_d^2 = (z_3\sigma_4)^2 + (z_4\sigma_3)^2$$

(8)

$$(b) \quad \sigma_K^2 = \sigma_k^2 + \sigma_5^2$$

where

$$(8) \quad (c) \quad \sigma_5^2 = \frac{\sigma_d^2}{u^2} + \frac{\sigma_u^2}{u^4} M_d^2$$

σ_d is determined. The expressions for the uncertainties σ_3 and σ_4 are first derived. From eqs. 6c and 6d one has

$$\sigma_3^2 = \{(\frac{\sigma_1}{z_1})^2 + (\frac{\sigma_2}{z_2})^2\} z_3^2$$

where

$$\sigma_1^2 = \{(\frac{\sigma_u}{u})^2 + (\frac{\sigma_{u'}}{u'})^2\} z_1^2$$

$$\sigma_2^2 = \sigma_u^2 + \sigma_{u'}^2$$

whence

$$\sigma_3^2 = \{(\frac{\sigma_u}{u})^2 + (\frac{\sigma_{u'}}{u'})^2 + \frac{\sigma_u^2+\sigma_{u'}^2}{z_2^2}\} (\frac{z_1}{z_2})^2$$

$$\sigma_3^2 = (u')^2 \{\frac{(u+u')^2+u^2}{(u+u')^4}\} \sigma_u^2 + u^2 \{\frac{(u+u')^2+u'^2}{(u+u')^4}\} \sigma_{u'}^2$$

In the first approximation, σ is chosen such that $\sigma \geq \sigma_u$ or $\sigma_{u'}$, so that one obtains

$$\sigma_3^2 \leq \frac{(u^2+u'^2)(u+u')^2+2(uu')^2}{(u+u')^4}\sigma^2$$

Expanding the numerator

$$\sigma_3^2 \leq \frac{u^4+2u^3u'+4(uu')^2+2uu'^3+u'^4}{(u+u')^4}$$

whence

$$\sigma_3^2 \leq \{1 - \frac{2uu'}{(u+u')^2} + \frac{2(uu')^2}{(u+u')^4}\}\ \sigma^2$$

since the second term is larger than the third term.

$$(9) \quad \sigma_3^2 \leq \sigma^2$$

Now σ_4 is determined where

$$\sigma_4^2 = \sigma_K^2 + \sigma_{K'}^2$$

and finally σ_d, where one has from eq. 8a

$$(10) \quad \sigma_d^2 \leq (\frac{uu'}{u+u'})^2\ (\sigma_K^2 + \sigma_{K'}^2) + (K' - K)^2\ \sigma^2$$

Turning to eq. 8c, σ_5 is calculated

$$\sigma_5^2 \leq (\frac{u'}{u+u'})^2\ (\sigma_K^2+\sigma_{K'}^2)+\frac{(K'-K)}{u^2}\ \sigma^2\{1+\frac{u'^2}{(u+u')^2}\}$$

Hence the total uncertainty σ_K is by eq. 8b

$$(11)\quad \sigma_K^2 \leq \{1+(\frac{u'}{u+u'})^2\}\sigma_K^2+(\frac{u'}{u+u'})^2\ \sigma_{K'}^2 +$$

$$(K'-K)^2\ (\frac{u'}{u})^2\ (\frac{\sigma}{u'})^2\ \{1+\frac{u'^2}{(u+u')^2}\}$$

The quantity $\frac{\sigma}{u'}$ appears in the third term of eq. 11 because the greater nonlinearity in the velocity u' makes the measurement of u' more uncertain than that of u. A check of exp X-B_2' (fig. 41) and exp X-B_1' (records not shown) shows that the velocities u and u' for both experiments are about the same. In keeping with the policy of overestimating σ_K, the values $u = 1.15\frac{\frac{1}{2}\lambda}{min}$ and $u' = 0.70\frac{\frac{1}{2}\lambda}{min}$ are chosen. Furthermore a measurement of the maximum error in the velocity determination indicates that $\frac{\sigma}{u'} < 0.15$. Hence applying these numerical values, one may show

$$(\frac{u'}{u+u'})^2 < 0.2\ ,\qquad (\frac{u'}{u})^2 < 0.4$$

so that eq. 11 now becomes

$$(12)\quad \sigma_K^2 < 1.2\ \sigma_K^2 + 0.2\ \sigma_{K'}^2 + 0.011\ (K'-K)^2$$

Since the drift causes less than a 5% difference in the two scale factors, k and k', of the two experiments, one may choose the quantity k'-k =0.05 x0.5 =0.025. Also typical values for the least-squares uncertainties are $\sigma_k < 0.0020$ and $\sigma_{k'} < 0.0040$ (see p. 130, 133). Then using these approximations, one may then compute the total uncertainty σ_K

$$\sigma_K^2 \leq 14.5 \times 10^{-6}$$

$$\sigma_K < 0.0040$$

A similar derivation using eq. 1b rather than 1a will yield the result

$$(13) \quad \sigma_K^2 \leq \{1+(\frac{u}{u'+u})^2\}\sigma_K^2 + (\frac{u}{u+u'})^2 \sigma_{K'}^2 + (K'-K)^2 (\frac{\sigma}{u'})^2 \{1+ \frac{u'^2}{(u+u')^2}\}$$

This time using $u = 1.25 \frac{\frac{1}{2}\lambda}{\text{min}}$ and $u' = 0.60 \frac{\frac{1}{2}\lambda}{\text{min}}$, the uncertainty, σ_K, is calculated to be

$$\sigma_K^2 < 51 \times 10^{-6}$$

$$\sigma_K < 0.007$$

It is obvious from the above calculations that a smaller uncertainty, σ_K, is associated with eq. 1a rather than 1b. This results mainly from the presence of k in eq. 1a. Its value is known with more confidence than that of k' whose uncertainty is responsible for the larger σ_K computed from eq. 1b. Hence $\sigma_K = 0.004$ will be used in the text to obtain the final uncertainty in the calibration scale factor.

Equation 12 shows that σ_K will increase with k'-k. This is an important observation because as much as 10-percent

differences between the scale factors k and k' have been observed with other records. Then one may ask the question: how large must k'-k be, for $\frac{\sigma_K}{K}$ to equal 0.01? For under this condition the results of the calibration must be rejected if a 1-percent calibration is desired. Then dividing eq. 11 by K^2, one obtains

$$(14) \quad \left(\frac{\sigma_K}{K}\right)^2 \leq 1.2 \left(\frac{\sigma_K}{K}\right)^2 + 0.2 \left(\frac{\sigma_{K'}}{K}\right)^2 + 0.011 \left(\frac{K'-K}{K}\right)^2$$

With $\frac{\sigma_K}{K} = .01$ and $K = 0.520$ one obtains

$$\left(\frac{k'-k}{K}\right)^2 = 71 \times 10^{-4}$$

$$\frac{k'-k}{K} = .084$$

Hence for the particular conditions of this calibration: e.g. the wavelength scale has 14 divisions for the expansion drive and 8 divisions for the contraction drive, $u \approx 1.2 \frac{\frac{1}{2}\lambda}{\text{min}}$ and $u' \approx 0.65 \frac{\frac{1}{2}\lambda}{\text{min}}$; the results must be rejected when the drift causes k and k' to differ from each other by an amount greater than 8% of K.

APPENDIX C

TRANSMISSION OF WAVELENGTHS FROM OTHER PARTS OF THE HELIUM SPECTRUM

In ch. V, sec. D, it was stated that the transmission of wavelengths from other parts of the helium spectrum through the Bausch and Lomb filter would shift the transmitted fringe of the 5016 Å line from the theoretical position it would otherwise occupy if there was no leakage. In this appendix it is demonstrated that any loss of accuracy and linearity in the wavelength scale due to this leakage will not be appreciable and may therefore be ignored.

In calculating the peak offset Δm and the peak width, p, one would superimpose the "contaminating fringe" with the "measuring fringe." Superposition may be done graphically. Let λ = the wavelength of the "measuring fringe"

λ' = the wavelength of the "contaminant"

The fringe contours corresponding to these wavelengths are assumed to be due only to the Airy distribution of the transmitted intensity. One thus has

$$(a) \quad I = \frac{I_o}{1+F \sin^2 \pi m} \qquad m = \frac{2h}{\lambda}$$

(1) where

$$(b) \quad I' = \frac{I_o'}{1+F \sin^2 \pi m'} \qquad m' = \frac{2h}{\lambda'}$$

The primed letters refer to the "contaminating fringe" and $I_o' = I_o/10$.

To perform the superposition operation, the "contaminating" and "measuring fringes" are plotted as functions of the order position, m (see eq. 1), and the peak of the "contaminant" is placed at several order positions along the "measuring fringe" contour where $I = 0.95I_o$, $0.90I_o$, $0.80I_o$, and $0.70I_o$. From eq. 1 the order position of the "contaminant", m' is determined in terms of the order position, m.

$$(2) \qquad m' = \frac{\lambda}{\lambda'} m$$

If m_p and $m_{p'}$ are the positions of the "measuring-" and "contaminating-fringe" peaks respectively, and if Δm and $\Delta m'$ represent any offset from m_p and $m_{p'}$ respectively, one may calculate the corresponding points on I and I' from eq. 1. First noting that

$$\text{Sin } \pi m = \text{Sin } \pi(m_p \pm \Delta m) = \pm \text{Sin } \pi \Delta m$$

$$\text{Sin } \pi m' = \pm \text{Sin } \pi \Delta m',$$

one then has

$$(3) \qquad (a) \quad I = \frac{I_o}{1 + F \text{ Sin}^2 \pi \Delta m}$$

$$(b) \quad I' = \frac{I_o}{1 + F \text{ Sin}^2 \pi \Delta m'}$$

Let μ be the distance in order number between the "contaminating-" and "measuring-fringe" peaks (see fig. 53). From fig. 53, the offset from the "contaminating-fringe" peak $\Delta m'$ which defines the order position where I and I' are to be added is by eq. 2

$$(4) \qquad \Delta m' = \frac{\lambda}{\lambda'} (\mu \pm \Delta m)$$

Then the fringes superimpose according to the law

$$(5) \qquad I_t = I_o \left\{ \frac{1}{1+F \sin^2 \pi \Delta m} + \frac{0.1}{1+F \sin^2 \pi \frac{\lambda}{\lambda'} (\mu \pm \Delta m)} \right\}$$

The first term in eq. 5 is the contribution of the "measuring fringe," and the second term is the contribution of the "contaminating fringe."

Suppose μ is chosen so that the λ' peak lies at a position coincident with a point on the λ contour where $I = fI_o$ ($|f|<1$). The quantity μ is calculated from eq. 3a where $\Delta m = \mu$. One thus has

$$f = \frac{1}{1+F \sin^2 \pi \mu}$$

$$\pi \mu = \sin^{-1} \left(\frac{1-f}{fF} \right)^{\frac{1}{2}}$$

With $F = 80$ and the quantity $\left(\frac{1-f}{fF}\right)^{\frac{1}{2}} < 0.1$, one obtains the approximate expression

$$(6) \qquad \mu = \frac{1}{4\pi (5)^{\frac{1}{2}}} \left(\frac{1-f}{f} \right)^{\frac{1}{2}}$$

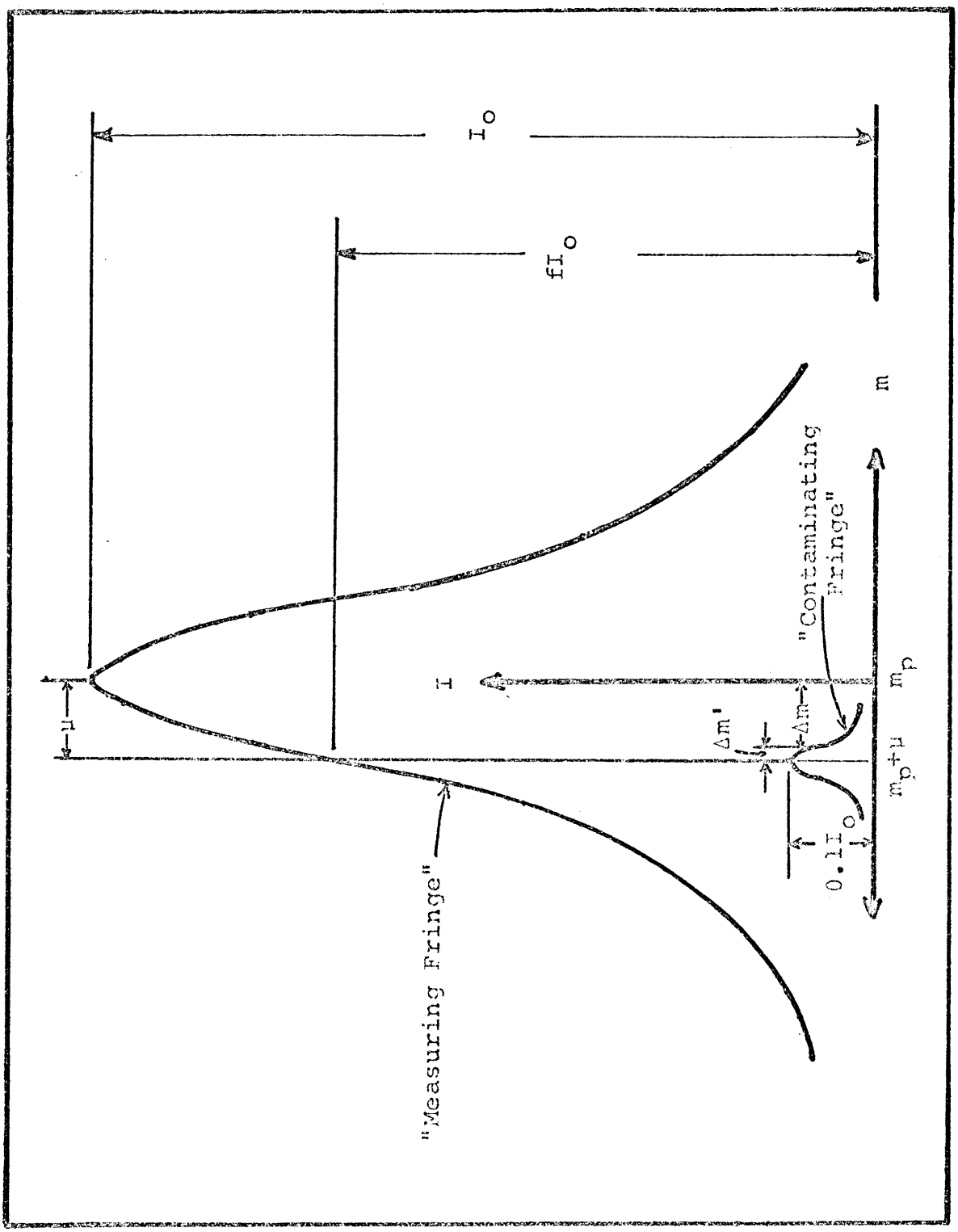

Figure 53. The Geometric Relations Between the "Measuring Fringe" and the "Contaminating Fringe".

Choosing f = 0.95, 0.90, 0.80, and 0.70, eqs. 3, 5, and 6 are calculated, and the resultant fringes are plotted in fig. 46 with an uncontaminated peak for comparison. In Table XI a set of sample calculations have been performed for the case f = 0.95, and λ = 5000 Å, λ' = 6000 Å. In fig. 46 the peak is displaced by a maximum amount of 0.002 order and broadened by a maximum amount of 0.001 order. Hence the position of the peak will not be significantly altered so as to affect the 1-percent accuracy of the calibration.

Table XI

COMPUTATION OF POINTS ON THE RESULTANT FRINGES WHEN THE INTERFEROMETER TRANSMITS WAVELENGTHS FROM OTHER PARTS OF THE HELIUM SPECTRUM

for $f = 0.95$

$\lambda = 5000\ \mathring{A}$

$\lambda' = 6000\ \mathring{A}$

$$\left(\frac{1-f}{f}\right)^{\frac{1}{2}} = 0.230$$

$$\mu = \frac{1}{4\pi(5)^{\frac{1}{2}}}\left(\frac{1-f}{f}\right)^{\frac{1}{2}} = 0.0082$$

$$\theta = \pm\ \Delta m\pi$$

$$\theta' = (\mu \pm \Delta m)\pi\,\frac{\lambda}{\lambda'} = 2.617\ (\mu \pm \Delta m)$$

$$I + I' = I_t = \frac{1}{1+80\ \theta^2} + \frac{0.1}{1+80\ \theta'^2}$$

Calculation of I

Δm	θ	$\theta^2 \times 10^{-5}$	$1+80\ \theta^2$	I
-.0150	.0471	222	1.178	0.8489
-.0100	.0314	98.6	1.0789	0.9269
-.0050	.0157	24.6	1.0197	0.9807
-.0040	.0127	16.1	1.01288	0.9873
-.0020	.0063	3.9	1.00312	0.9969
-.0010	.0031	0.99	1.00079	0.9992
.0000	.0000	0.00	1.00000	1.0000
.0010	.0031	0.99	1.00079	0.9992
.0020	.0063	3.9	1.00312	0.9969
.0040	.0127	16.1	1.01288	0.9873
.0050	.0157	24.6	1.0197	0.9807
.0100	.0314	98.6	1.0789	0.9269
.0150	.0471	222	1.178	0.8489
.0200	.0628	394	1.315	0.7604
.0250	.0785	616	1.493	0.6694
.0030	.0942	887	1.710	0.5848

Table XI - continued

Calculation of I' and I_t

$-\Delta m$	$\mu \pm \Delta m$	θ'	$\theta'^2 \times 10^{-5}$	$1+80\theta'^2$	I'	I	I_t
.0150	.0232	.0607	397	1.295	.0772	.8489	0.926
.0100	.0182	.0476	227	1.181	.0846	.9269	1.012
.0050	.0132	.0345	119	1.095	.0913	.9807	1.072
.0040	.0122	.0319	102	1.081	.0925	.9873	1.080
.0020	.0102	.0267	71.2	1.057	.0946	.9969	1.092
.0010	.0092	.0259	67.1	1.054	.0949	.9992	1.094
.0000	.0082	.0215	46.1	1.037	.0964	1.0000	1.096
-.0010	.0072	.0188	35.5	1.028	.0972	.9992	1.096
-.0020	.0062	.0162	26.3	1.021	.0979	.9969	1.095
-.0040	.0042	.0110	12.1	1.010	.0990	.9873	1.086
-.0050	.0032	.0084	7.01	1.006	.0994	.9807	1.080
-.0100	-.0018	-.0047	2.22	1.002	.0998	.9269	1.027
-.0150	-.0068	-.0178	31.7	1.025	.0975	.8489	0.946
-.0200	-.0118	-.0309	95.4	1.076	.0929	.7604	0.853
-.0250	-.0168	-.0440	193	1.155	.0866	.6694	0.757
-.0300	-.0218	-.0571	325	1.260	.0793	.5848	0.664

BIBLIOGRAPHY

Benioff, Hugo, 1959, Fused quartz extensometer for secular tidal and seismic strains: Geol. Soc. America Bull., v. 70, p. 1019-1031.

Blayne, J. L. and Gilman, R., 1965, A portable strainmeter with continuous interferometric calibration: Seismol. Soc. America Bull., v. 55, p. 955-970.

Bottom, V. E., 1964, Fabry-Perot Dilatometer: Rev. Sci. Instruments, v. 35, p. 374-376.

Born, M. and Wolf, E., 1965, Principles of optics: New York, Pergamon Press, 777 p.

British Scientific Instrument Research Association, 1963, A guide to instrument design: London, Taylor and Francis Ltd., 435 p.

Bruce, C. F., 1966, On automatic parallelism control in a scanning Fabry-Perot Interferometer: Applied Optics, v. 5, p. 1447-1452.

Candler, C., 1951, Modern interferometers: Glasgow, Hilger and Watts, Ltd., 494 p.

Chabbal, R., 1958, Finesse Limite D'un Fabry-Perot Forme de Lames Imparfaites: Jour. Phys. Radium, 19, p. 295-300.

Edlén, B., 1966, The refractive index of air: Metrologia, v. 2, p. 71-80.

Edlén, B., 1953, The dispersion of standard air: J.O.S.A., v. 43, p. 339-344.

Englehard, E., 1957, Precise interferometric measurement of gage blocks: Metrology of gage blocks: U. S. Natl. Bur. Stand., Circ. 581, p. 1-20.

Francon, M., 1966, Optical interferometry: New York, Academic Press, 307 p.

Jaquinot, Pierre, 1954, The luminosity of spectrometers with prisms, gratings, or Fabry-Perot etalons: J.O.S.A., v. 44, p. 761-764.

Kane, Julius, 1966, Fiber optics and strain interferometry: I.E.E.E. Geoscience Electronics Trans., GE-4, p. 1-11.

Kline, J. V., 1952, A variable spacing Fabry-Perot interferometer: Purdue Univ., Ph.D. Thesis, 104 p.

Lansing Research Corp., 1965, Product Catalogue: p. 17-20.

Major, M. W., Sutton, G. H., and Oliver, Jack, 1964, On elastic strain of the earth in the period range of 5 seconds to 100 hours: Seismol. Soc. America Bull., v. 54, p. 295-346.

Meissner, M. W., 1941, Interference spectroscopy. Part I: J.O.S.A., v. 31, p. 405-427.

Romig, P. R., Jr., 1967, Millimicron displacement transducer with mechanical calibration: Colo. School Mines, M.Sc. Thesis, T-1123, 59 p.

Rossi, Bruno, 1957, Optics: Reading, Mass., Addison-Wesley Publ. Co., Inc., 510 p.

Sears, F. W., and Zemansky, M. W., 1960, University physics: Reading, Mass., Addison-Wesley Publ. Co., Inc., 3rd ed., 1011 p.

Slater, P. N., Betz, H. P., and Henderson, G., 1965, A new design of a scanning Fabry-Perot Interferometer: Applied Phys. Jap. Jour., v. 4, Supplement I, p. 440-444.

Sluis, K. L. V., and McNally, J. R., Jr., 1956, Fabry-Perot Interferometer with finite apertures: J.O.S.A., v. 46, p. 39-46.

Terrien, J., 1960, The Wavelength of the helium line, 5016 Å: London, Interferometry, Her Majesty's Stationery Office, 471 p.

Vali, V., Krogsted, R. S., and Moss, R. W., 1965, Laser interferometer for earth strain measurements: Rev. Sci. Instruments, p. 1352-1355.

Wiese, W. L., Smith, M. W., and Glennon, B. M., eds., 1966, Atomic transition probabilities: U. S. Natl Bur. Stand., NSRDS-NBS4, v. 1, 153 p.

Wildhack, W. A., Powell, R. C., and Masin, H. L., eds., 1965, Accuracy in measurement and calibration: NBS Tech. Note-262, 145 p.